NANO ELECTROCERAMICS FOR INTERMEDIATE TEMPERATURE SOLID OXIDE FUEL CELL

By

Raja Kishora Lenka

Enrolment No: CHEM01200604025

Bhabha Atomic Research Center, Mumbai

A thesis submitted to the

Board of Studies in Chemical Sciences

In partial fulfillment of requirements

For the Degree of

DOCTOR OF PHILOSOPHY

of

HOMI BHABHA NATIONAL INSTITUTE

July, 2012

Homi Bhabha National Institute

Recommendations of the Viva Voce Board

As the members of the Viva Voce board, we certify that we have read the dissertation prepared by Mr. Raja Kishora Lenka entitled "Nano Electroceramics for Intermediate Temperature Solid Oxide Fuel Cell" and recommended that it may be accepted as fulfilling the dissertation requirement for the degree of Doctor of Philosophy.
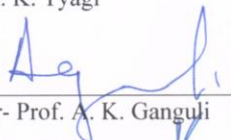
Chairman- Prof. G. K. Dey   Date: 1-04-2013

Convenor- Prof. A. K. Tyagi   Date: 1-04-2013

External Examiner- Prof. A. K. Ganguli   Date: 1-04-2013

Member- Prof. S. K. Mukerjee   Date: 1-04-2013

Member- Prof. S. M. Yusuf   Date: 1-04-2013

Final approval and acceptance of this dissertation is continment upon the candidate's submission of the final copies of the dissertation to HBNI.

I hereby certify that I read this dissertation prepared under my direction and recommended that it may be accepted as fulfilling the dissertation requirements.

Date: 1-04-2013

Place: BARC

(Prof. A. K. Tyagi)

STATEMENT BY AUTHOR

This dissertation has been submitted in partial fulfillment of requirements for an advanced degree at Homi Bhabha National Institute (HBNI) and is deposited in the Library to be made available to borrowers under rules of the HBNI.

Brief quotations from this dissertation are allowable without special permission, provided that accurate acknowledgement of source is made. Requests for permission for extended quotation from or reproduction of this manuscript in whole or in part may be granted by the Competent Authority of HBNI when in his or her judgment the proposed use of the material is in the interests of scholarship. In all other instances, however, permission must be obtained from the author.

Raja Kishora Lenka

DECLARATION

I, hereby declare that the investigation presented in the thesis has been carried out by me. The work is original and has not been submitted earlier as a whole or in part for a degree / diploma at this or any other Institution / University.

Raja Kishora Lenka

Dedicated to my parents

ACKNOWLEDGEMENTS

RAJA KISHORA LENKA

Contents

Chapter 5

Chapter 6

Synthesis and Characterization of GdCoO$_3$ based Cathode Materials

Chapter 7

Evaluation of Electrode Performance by Electrochemical Impedance Spectroscopy (EIS)

Chapter 8

Fabrication and characterization of single cells

Chapter 9

Conclusions

Synopsis

Solid Oxide Fuel Cell (SOFC) is an all oxide electrochemical device which directly converts chemical energy into electrical energy in an efficient and environmental friendly manner [1]. SOFCs are required to be operated at high temperatures for getting high power density. The operating temperature has been reported to be as high as 1000 ^{o}C. However, operation at high temperatures leads to various practical problems, such as, corrosion, thermal instability of the materials, loss of mechanical integrity [2]. Interdiffusion of cations at the interfaces at high temperatures may lead to formation of electrically insulating barrier at the interface and thereby decreasing the cell performance over a period of time. Therefore, selection of SOFC functional materials as well as materials required for assembling the cells become a constraint for SOFCs operating at higher temperatures. These problems can be largely circumvented by bringing down the operating temperature of a SOFC cell. Lower temperature operation will lead to long term stability and reduced cost. Hence, there has been continuous effort to reduce the operating temperature of SOFC without sacrificing the overall performance.

For improved performance the internal resistance of a cell should be as low as possible at the operation temperatures. In a fuel cell the internal resistance is primarily comprised of the ohmic resistance contribution from the materials and interfacial polarization resistance from the electrode-electrolyte interfaces. The ohmic resistance of the electrolyte is much higher compared to the electrode materials. Therefore, the electrolyte should be an excellent oxygen ion conducting material and the thickness of the electrolyte layer should be minimum in the SOFC stack. There has also been continuous effort to reduce the interfacial polarization resistance by way of searching new electrode materials having superior electro-catalytic activity in the intermediate temperature range. Optimization of cell fabrication methodology and electrode microstructure plays an important role in reducing the area specific resistance of a cell

and thus enhancing the performance. Further, the electrode materials must be compatible with the electrolyte material.

Yttria stabilized zirconia (YSZ) is the most widely used electrolyte material till now. The operating temperature for SOFC is between 800-1000 ^{o}C when YSZ is used as an electrolyte. The high temperature operation can be minimized by the use of alternative electrolyte materials having appreciable ionic conductivity at lower temperature. Doped ceria, bismuth oxides and lanthanum gallate are few electrolytes reported in the literature which have appreciably ionic conductivity at lower temperature [3]. However, in addition to high ionic conductivity an electrolyte must be stable in both oxidizing and reducing environments. Bismuth oxide based systems fall short in terms of their stability in reducing environment. In lanthanum gallate based electrolyte systems gallium evaporation at elevated temperature is a major concern for use as SOFC electrolyte. In doped ceria system change in valency state of cerium cations takes place at high temperature and reduced environment leading to introduction of electronic conductivity in the material [4]. However, it has been reported that at intermediated temperature (600-800 ^{o}C) the electronic contribution is negligible and ionic conductivity is appreciable in doped ceria system thus making it as a potential electrolyte material for intermediate temperature solid oxide fuel cell (IT-SOFC)[5].

At the anode-electrolyte interface electrochemical combination of oxide ion and hydrogen takes place. Nickel is the most suitable low cost material for the hydrogenation reaction [6]. A composite of nickel and electrolyte material is commonly used as an anode material. The composite anode structure helps in matching the thermal expansion coefficient with the electrolyte material and extends the triple phase reaction sites. NiO is generally used as the precursor material for anode. NiO gets reduced to Ni under the cell operating conditions. The anode microstructure in terms of particle size and distribution of composite phases play an important role in determining the catalytic activity towards hydrogenation reaction [7,8].

The oxygen reduction reaction of the cathode requires a mixed ionic and electronic conductor (MIEC) for decreasing cathode resistance and thereby increasing the performance [9,10]. In the intermediate temperature range doped $LnCoO_3$ (Ln=

lanthanides) system shows highest conductivity and lowest cathodic over potential. However, mismatch in thermal expansion coefficient is a common problem in many doped $LnCoO_3$ system. For GDC electrolyte based SOFC, $GdCoO_3$ based cathode could be a candidate material. Limited literature is available on the use of $GdCoO_3$ as cathode material. The functional properties are influenced by addition of dopants. Therefore, defining suitable composition with improved microstructure is of particular importance for practical application.

As discussed above, the roles of polarization resistance and electrolyte thickness are crucial for the overall performance. The ceramic fabrication technique plays an important role in order to minimize the area specific cell resistance. The fabrication parameters need to be optimized for a particular starting powder. Electrode and interface microstructure can be tailored when starting with nano-ceramic powder. Solution synthesis routes are known for producing high purity nano-sized powders of mixed oxides at lower temperature.

In view of the above, the present thesis is aimed towards development of nano-electroceramics for IT-SOFC application. Gadolinia doped ceria has been chosen as the electrolyte material. Ni-GDC and Ba-doped $GdCoO_3$ have been considered as the anode and cathode materials, respectively. The following objectives were set to be realized in the present study.

- o Preparation and characterization of nano-powders of the above mentioned IT-SOFC materials through solution synthesis route and optimization of processing parameters.
- o Study of sintering behavior of the nano-electroceramic powders.
- o Evaluation of functional properties of individual IT-SOFC materials.
- o Integration of cell materials to form symmetric cells and single cells and electrochemical evaluation.

To meet the above objectives, 12 mol% gadolinia doped ceria (12GDC) powder was synthesized by combustion route using different fuels. The characteristics of the processes have been studied by thermal analysis of gel precursor. The processes have been analyzed through thermodynamic calculation. Physical properties of powders prepared through different route were characterized. Based on the characteristics of

the synthesized GDC powder metal nitrate - citric acid gel combustion route was chosen for the preparation of powder. In order to study the effect of dopant concentration on the sintering and electrical behavior, GDC powders of different composition (3, 6, 8, 10, 12, 15 and 18 mol% GDC) were synthesized by citrate-nitrate gel combustion route. Shrinkage behavior of GDC powders was monitored by a dilatometer. The powders were sintered to get pellets with density above 97% of theoretical density. The dense sintered pellets of different compositions were used for conductivity measurements using a frequency response analyzer. The contributions of bulk and grain boundaries towards the total resistance have been delineated and the conductivity has been explained on the basis of hopping frequency from the complex impedance plot. The activation energies for oxygen ion conduction in the bulk and grain boundary have been determined from the Arrhenius type relationship of conductivity. It was confirmed that maximum ionic conductivity was obtained with 12 mol% GDC. 12GDC pellet sintered at 1200 ^{o}C are further heated for grain growth in order to study the effect of grain size on ionic conductivity.

Ultrafine NiO powder for use in anode material was synthesized by solution combustion route. NiO-GDC composition in 50:50 weight ratios was prepared by mixing in a pot mill. Shrinkage behavior of the anode composition was studied using a dilatometer. Electrical conductivity was measured after reduction in hydrogen atmosphere. The effect of sintering temperature on the microstructure and electrical conductivity of Ni-GDC cermet was studied. For estimating the ASR at the interfaces, NiO-GDC electrode and GDC electrolyte have been integrated in symmetric cell form to evaluate the interfacial polarization resistance by ac impedance spectroscopy technique.

Gadolinium cobaltate doped with different percentage of barium was synthesized by solution combustion route as well as solution polymerization method. Based on the process and powder characteristics the later process was chosen for further study. The effect of barium doping on sintering behavior, thermal expansion coefficient and electrical conductivity was studied. Symmetrical cells were prepared and area specific resistance for interfacial polarization was evaluated. The composition and processing parameters were optimized for its application as cathode.

Based on the results of the above studies, anode supported single cells were fabricated by tape casting method. In this electrolyte, anode was integrated by co-casting in tape form and co-firing. Cathode slurry in terpinoel medium was painted over the electrolyte followed by sintering. I-V characterization of the single button cell was carried out.

The total work carried out in this thesis has been organized in eight chapters with further sub-chapters as and when required.

Chapter 1: Introduction

The need of SOFC as an energy efficient and environment friendly new technology has been addressed. This chapter contains a brief review on the functioning of a SOFC, its advantages and disadvantages. Different designing aspects of a SOFC and associated advantages are presented. It outlines technological importance of the materials, and issues associated with high temperature operation of the fuel cell. Review on the literature pertaining to the present work is narrated here. The necessity of an intermediate temperature solid oxide fuel cell has been addressed. Present IT-SOFC materials and their status are reviewed in this chapter. More detailed literature review is also incorporated in the individual chapters. Finally, based on the literature review a set of IT-SOFC materials have been selected and statement of the objectives and scope of the work have been described.

Chapter 2: Experimental

The synthesis techniques adopted in preparation of different nano-ceramics and the experimental techniques used for characterization of the ceramics have been presented in the Chapter 2. The solution combustion route used for preparation of GDC and NiO powder has been described. Solution polymerization route adopted for preparation of gadolinium cobaltate has been elaborated. Thermal analysis (TG/DSC) of the gel precursors / precursor powders has been carried out in order to study the nature of thermal decomposition and determination of calcination temperatures. Phase evolution of synthesized powders was characterized by X–ray diffraction after calcination. Particle size of powder was characterized by laser scattering particle size analyzer. Surface area was measured using BET principle. Particle morphologies were observed in scanning electron microscope (SEM) and transmission electron

microscope (TEM). The shrinkage behavior of the powder compact on heating was observed by a dilatometer.

The microstructures of the sintered samples were observed in SEM. The measurements of thermal expansion co-efficient of the sintered materials were carried out using a dilatometer. Electrical conductivity was estimated from the four probe measurements. Ionic conductivity of the electrolyte material was determined by ac impedance spectroscopic technique. The principle of all of these characterization techniques have been described in detail in this chapter.

The electrodes have been integrated with electrolyte to form symmetric cells for evaluation of area specific interfacial polarization resistance. The methodology adopted for integrating the cell has been described. The technique used for determining ASR has been elaborated. Anode supported cell has been fabricated and performance tested. The single cell fabrication methodology and the testing procedure have been elaborated in this chapter.

Chapter-3: Synthesis and characterization of GDC electrolyte material

Preparation of gadolinia doped ceria powder through gel combustion route and its characterization has been discussed in this chapter. Ceria powder doped with 12 mol% gadolinia was prepared by combustion route using different fuels (citric acid, glycine and urea) to study the effect of fuel on the combustion process and powder characteristics. The exothermic heat energies and adiabatic flame temperatures of the possible combustion reactions have been calculated theoretically for different fuels. TG-DTA results of the dried gels indicate that calcination step is not necessary for powders synthesized using citric acid and glycine as fuel. However, the powder produced using urea needs to be calcined at 700° C. The crystallite size of the combustion synthesized powder depends on the type of fuel and is in relation with the exothermic heat and the flame temperature of the reaction. The degree of agglomeration was found to vary with the fuel type. Citric acid was found to give optimum results in terms of producing carbon free nano-crystalline powder through a controlled combustion reaction and with minimal agglomeration. As-synthesized powder prepared using citric acid could be sintered to near theoretical density at 1250

^{o}C. It is observed that sintered density remains low when using powder cacined at higher temperature. Based on the above observations, for the subsequent studies gadolinia doped ceria powders have been prepared by combustion route using citric acid as fuel.

In order to study the effect of gadolinia content on powder characteristics, its sintering behaviour and ionic conductivity Gadolinia doped ceria with different compositions were prepared by combustion route. X-ray diffraction patterns indicated that phase pure powder is obtained in combustion synthesis for all the compositions. The powders were nanocrystalline in nature as revealed from the X-ray line broadening. The particle size (agglomerate size) measured by laser scattring particle size shows monomodal distribution of particles for all the compositions. Analysis of crystallite size, surface area and particle size indicates that the powders are agglomerates of nanosize primary particles. The degree of agglomeration increases with increase in gadolinia content. The shrinkage behavior on firing of the powders was studied using a dilatometer. Although the shrinkage starts at a lower temperature the densification completes at higher temperature as the gadolinia content increases. Shrinkage pattern with different composition shows initial shrinkage at lower temperature below 600 ^{o}C and shrinkage insertion temperature decreases with gadolinia doping which is attributed to the increased reactivity with gadolinia doping. However for complete densification the final temperature increases as hard agglomerates are formed with increase in doping concentration.

Chapter-4: Ionic conductivity of GDC electrolyte
The results on the electrical conductivity of gadolinia doped ceria have been presented and discussed in this chapter. The conductivity data have been presented in complex impedance plot (Z" vs. Z'). After analyzing the impedance plot the conductivity is presented in terms of Arrhenius plots, from which activation energy is calculated. The hopping frequency related to oxygen jump has been evaluated from the imaginary impedance spectra (plot of Z" vs. log frequency). The frequency corresponding to max value of Z" could be related to the hopping frequency.

It has been observed that the conductivity of GDC system increases with increase in gadolinia content. Maximum conductivity is obtained for 12 mol% gadolinia doped

ceria. Thereafter, on further doping conductivity has been found to decrease. As the gadolinia concentration increases the oxygen vacancy concentration increases leading to increase in oxygen ion conductivity. However, at higher dopant concentration vacancy association takes place leading to decrease in conductivity. The activation energies for ion conduction /ion hopping have been found to increase with gadolinia content.   For the GDC compositions studied, the activation energy for bulk conduction varies from 0.66 to 1.13 eV and the activation energy for grain boundary conduction varies from 0.97 to 2.24 eV. The variation in activation energy has been attributed to higher degree of association as the gadolinia content increases. For grain boundary process the activation energies are higher than that of bulk. The difference decreases with increase in gadolinia content.

In order to study the effect of grain size on ionic conductivity samples of 12 mol% Gd_2O_3 doped ceria having different grain sizes were produced. In the low temperature measurements, a significant decrease in the total resistivity was observed in the fine grained sample. As the grain size decreases the bulk conductivity is found to decrease and grain boundary conductivity is found to increase. Analysis of the impedance spectra indicates that the relaxation frequencies in the bulk and the grain boundary are influenced by grain size. This behavior explains well the significantly higher ionic conductivity in nanocrystalline doped ceria and zirconia structures reported earlier by many authors. However, improved ionic conductivity in fine grained material is observed only in the lower temperature range where grain boundary effect is dominant. In the higher temperature range, where the bulk effect is dominant, the total conductivity increases with increase in grain size.

Chapter-5: Synthesis and characterization of Ni-GDC composite for SOFC anode

NiO powder was synthesized by combustion method using glycine and citric acid as fuels. Results of thermal analysis and X-ray diffraction data show that as-synthesized powder contains some carbonaceous material and a mixture of NiO and Ni. Therefore, the powder was calcined at 700 ^{o}C for total conversion to NiO. SEM micrographs of the phase pure powder shows submicron size particles. Based on the recovery of powder, citric acid was chosen as fuel. Phase pure NiO and GDC powder are properly

mixed in a ball mill for better homogenization. Conductivity of a sintered bar pellet after reduction shows a value more than 1100 Scm^{-1} in the operating temperature region. Thermal expansion co-efficient of Ni-GDC is close to that of GDC electrolyte material. Symmetric cells have been fabricated using dense electrolyte and this NiO-GDC anode. ASR value of a NiO-GDC/GDC symmetric cell measured as low as 0.06 Ω.cm at 600 ^{o}C.

Chapter-6: Synthesis and characterization of GdCoO$_3$ based cathode materials

This chapter deals with the development of GdCoO$_3$ based new cathode material. Synthesis of the material was carried out by combustion method as well as solution polymerization method. Based on the thermogravimetric and X-ray diffraction results the as synthesized powder in combustion was calcined at 700 ^{o}C and the other powder at 1000 ^{o}C. Nano-crystalline powder was produced by a solution polymerization route and submicron size powder in combustion route as seen in the TEM micrographs. Shrinkage behavior of GdCoO$_3$ was observed with Ba doping. It has been observed with barium substitution that shrinkage starts at a lower temperature attributed to the more defect formation with doping. Electrical conductivity of GdCoO$_3$ at low temperature increases with increases with barium doping and remains almost unaffected at higher temperature. The conductivity of GdCoO$_3$ system is sufficient for better current collection. Thermal expansion of the material decreases with barium substitution and with 10% Ba substitution the TEC has decreased from 16 to 12 x 10^{-6} K^{-1}.

Chapter-7: Evaluation of electrode performance by electrochemical impedance spsctroscopy

Measurement of area specific resistance of electrode material determines the interfacial polarization resistance of the electrode electrolyte interface. Fabrication methodologies has great role in determining the interface i.e. the triple phase boundary. Hence this ASR value in the symmetric cell qualifies both the material and the fabrication procedure. Slurries of electrode material in terpinol medium were applied over dense electrolyte pellet. Symmetric measurements were taken in respective environment as seen in the fuel cell working condition. The interfacial polarization resistance of a dense NiO-GDC anode was 0.06 ohm.cm^2 at 600 ^{0}C in hydrogen environment. This value is comparable to the lowest ever ASR value

reported in case of NiO-GDC anode. SEM micrograph and EDS analysis showed well distributed Ni particles in GDC matrix helpful in decreasing the resistance.

From the symmetric cell measurement, the area specific resistance (ASR) of the pure $GdCoO_3$ was calculated to be 5 ohm.cm^2 at 900 ^{0}C. An attempt to increase the triple phase boundary was initiated with an addition of porous electrolyte layer, the measured ASR value was further decreased to 2 ohm.cm^2 at 900 ^{0}C. It has been observed that a composite layer of cathode and electrolyte layer has helped in decreasing the ASR value to 0.48 ohm.cm^2 at 900 ^{0}C. With Barium doping the ASR value is decreased because of mixed conductivity behavior [MIEC]. However the ASR values for sample with 10 mol% and 15 mol% Ba are not quite different. When graphite pore former was added the ASR value of a pure $GdCoO_3$ cathode decreases from 0.48 to 0.265 ohm.cm^2 and 0.40 to 0.12 5 ohm.cm^2 for 10 mol% Ba doped sample. This change in ASR value is due to increase in the triple phase boundary area.

Chapter-8: Fabrication and characterization of single cells

This chapter describes the methodology of Ni-GDC anode supported single cell fabrication by tape casting and its characterization. The materials used for electrolyte, anode and cathode were of optimized composition and prepared using optimized process parameters. The compositions of the tape casting slurries were suitably formulated based on powder characteristics. For the preparation of single cells, tapes of GDC electrolyte and NiO-GDC anode precursor were co-cast on a glass plate. The bi-layer was fired at 1350 ^{o}C to achieve near theoretical densification of GDC electrolyte. The cathode layer was formed by screen printing using a terpineol based slurry of cathode material followed by firing at 1050 ^{o}C. Microstructural characterization of the cell by SEM showed good adherence between the three layers before and after testing of cell. A maximum power density of 80 mW.cm^{-2} was obtained for these types of cells at 800 ^{o}C. The power density is expected to increase by improving the current collection.

Future scope:

Ba-doped GdCoO$_3$ being a novel cathode material there is need to study its long term stability under the cell operating conditions. The cells prepared using the nanoceramics as studied here need to be performance tested extensively. There is a further scope in optimization of cathode and anode microstructure for enhanced performance.

References:

1. N Q Minh, *J Am Ceramic Soc 76 (1993)563.*

2. J.A.M van Roosmalen and E.H.P. Cordfunke, *Solid State Ionics* 52(1992) 303.

3. Keegan C, Wincewicz, Joyce S. Cooper, *Journal of power Sources* 140(2005)280.

4. Y. Zhou, M.N. Rahman, *Acta. Mater.,* 45 (1997) 3635.

5. B.C.H. Steele, *Solid State Ionics,* 129 (2000) 95.

6. Jan Rossmeisl, Wolfgang G. Bessler, *Solis State Ionics* 178(2008) 1694.

7. Lee, J. H., Heo, J. W., Lee, D.S., Kim, J., Kim, G.H., Lee, H.W.et al,. *Solid State Ionics,* 158 (2003) 225.

8. Hideto Koide, Yoshiyuki Someya, Toshihiko Yoshida, Toshio Maruyama, *Solid State Ionics* 132(2000) 253.

9. S.P. Jiang, W. Wang, *Solid State Ionics* 176(2005) 1351.

10. Chunwen Sun, Rob Hui, Justin Roller, *Journal of Solid State Electrochemistry 14*(2009) 1125.

List of figures

List of tables

CHAPTER 1

Introduction

Fossil fuel is widely used as source of energy at present and more than 80% of the energy comes from coal, natural gas, and petroleum products [1]. However, considering a limit in these natural resources and increasing demand of power in modern life, the society has been compelled to think of new renewable energy sources before confronting any severity in future. The consumption of natural fuels leads to green house effect and this has further accelerated the quest for renewable energy sources. Renewable energy sources, such as, solar energy and wind energy are not continuous sources of energy. In the quest for continuous and reliable energy sources hydrogen is being considered worldwide as a future energy carrier. However, it is not naturally available and needs to be produced using renewable energy sources and nuclear energy. Fuel cell is considered to be a promising technology towards direct conversion of chemical energy of fuel to electrical energy without any intermediate step [2-3]. Being a direct energy conversion device the efficiency of energy production in fuel cell is high. The operation of a fuel cell is similar to a battery; the difference is that fuel cell is a continuous source of energy as long as the reactants are supplied to it. Like battery, it can be used in remote locations.

Fuel cell technology is being investigated in many countries for transport and power generation applications.

1.1 Different types of Fuel Cells

Fuel cell was first demonstrated by Sir William Grove in 1839 using a liquid electrolyte [4]. Later on in 1899, Nernst discovered the solid oxide electrolyte and the famous Nernst equation was established. Based on the electrolyte used fuel cells can be classified into five different types; namely, Polymer electrolyte membrane fuel cell (PEMFC), Alkaline fuel cell (AFC), Phosphoric acid fuel cell (PAFC), Molten carbonate fuel cell (MCFC) and Solid oxide fuel cell (SOFC). The moving ions and the interfacial catalytic reactions are different for different fuel cells. PEMFC, PAFC and AFC operate at a lower temperature region and pure hydrogen is used. However, the other two fuel cells (MCFC and SOFC) are operated at a higher temperature region. High temperature operation enables internal reforming of hydrocarbon in these fuel cells. Fuel and oxidant are supplied continuously at the anode side and cathode side, respectively. Based on the electrolyte and working temperature different types of catalyst are used for these cells. A comparison of different types of fuel cells is shown in Table 1.1.

Among the fuel cells, the low operating temperature fuel cells (PEMFC, AFC and PAFC) have been demonstrated in commercial application but not with a cost competitive basis. The cost of other two types of fuel cells, namely, MCFC and SOFC, are also high and

lack in competition with the contemporary power generating systems. MCFC uses molten

carbonate at high temperature and hence, corrosion problems need to be addressed with

long time operation. The modular design with all-solid construction, operating at high

efficiency has made SOFC attractive compared to other types of fuel cells. Westinghouse

laboratories have worked extensively towards the commercialization of fuel cell [5].

Table 1.1 Different types of fuel cells: A comparison

	Fuel cell type	Operating temperature (°C)	Fuel	Mobile ion	Electrolyte	Power efficiency (%)
Low temperature	PEMFC	60-90	Hydrogen	H^+	Sulphonated polymers	50-55
	AFC	50-200	Hydrogen	OH^-	Aqueous KOH	45-50
Medium temperature	PAFC	180-210	Hydrogen	H^+	H_3PO_4	35-45
High temperature	MCFC	650	Reformed hydrocarbons	CO_3^{2-}	$(Na/K)_2CO_3$	45-53
	SOFC	650-950	Hydrogen, Reformed hydrocarbons	O^{2-}	YSZ	45-57

1.2 Solid Oxide Fuel Cells (SOFC): Operating principle

In a solid oxide fuel cell (SOFC) the solid oxide electrolyte is sandwiched between two porous electrodes. Oxidant is passed through the cathode and oxygen ions are generated through electrochemical reactions at the cathode-electrolyte interface. Under chemical potential gradient these oxygen ions are transported through the oxygen conducting electrolyte to the anode side. Hydrogen is passed through the anode and at the anode-electrolyte interface the oxygen ions combine with the hydrogen to form water. The electrochemical reactions lead to the flow of current in the external load thus producing electricity. The schematic of a solid oxide fuel cell is shown in Fig. 1.1.
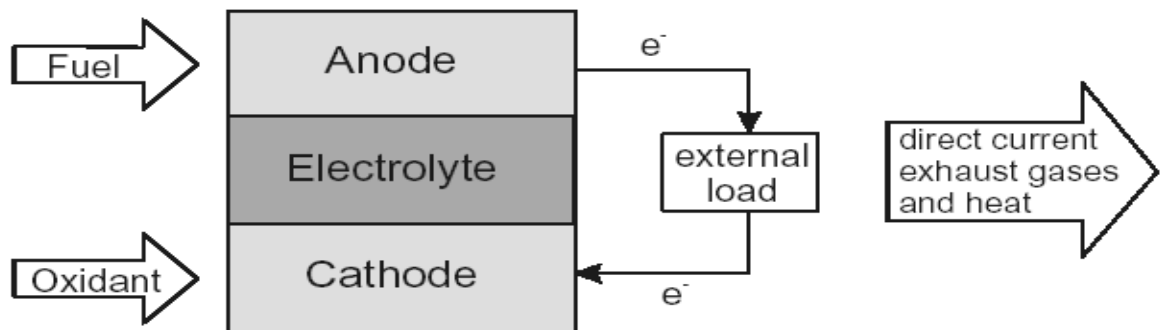
Fig.1.1 Schematics of a fuel cell

The electrochemical reactions of the fuel cell can be written as:

$$Cathode: \quad \tfrac{1}{2}O_2 + 2e^- \rightarrow O^{2-}$$
$$Anode: \quad H_2 + O^{2-} \rightarrow H_2O + 2e^-$$
$$\overline{Overall: \quad \tfrac{1}{2}O_2 + H_2 \rightarrow H_2O}$$
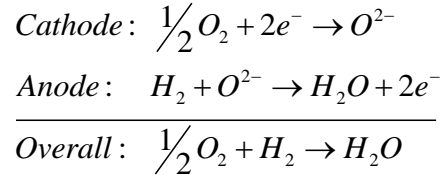
During a fuel cell operation oxygen is reduced at the interface of cathode and electrolyte, whereas hydrogen is oxidized at the anode side. The difference in the oxygen chemical potential is the driving force for the migration of oxygen ions from cathode to anode side. At the anode and electrolyte interface hydrogen combines with oxygen to form water along with release of two electrons which flows through the external circuit. All the electrochemical reactions at the electrode-electrolyte interface occur within a distance of less than 20 µm from the electrolyte surface, referred as the functional layer [6-7]. Beyond the functional layer rest part of the electrode is used for current collection and facilitates the flow of oxidants and fuels to the reaction sites. Dense electrolyte maintains the partial pressure difference between the cathode and anode. The difference of the chemical potential between oxidant gas and fuel is converted to the electrostatic potential difference of the anode and the cathode. From the partial pressures of different gases, the open circuit voltage (OCV) of the cell is determined using Nernst equation.

$$E = \frac{RT}{4F} \ln \left(\frac{P_{O_2}(\text{cathode})}{P_{O_2}(\text{anode})} \right)$$

..............(1.1)

where, R is the gas constant (8.314 J.mol^{-1}.K^{-1}) and F is the Faradays constant (96500 C.mol^{-1}).

For a hydrogen-oxygen fuel cell taking p_{O2} at the cathode side as 0.21 atm.(in case of air) and p_{O2} at the anode side as 10^{-18} atm. the open circuit potential is calculated to be 1.229 V. The potential developed in a fuel cell obeys Nernst equation at zero current. While drawing current from a cell, the cell voltage decreases due to internal resistance. Current to voltage characteristics of a typical SOFC is shown in Fig. 1.2.
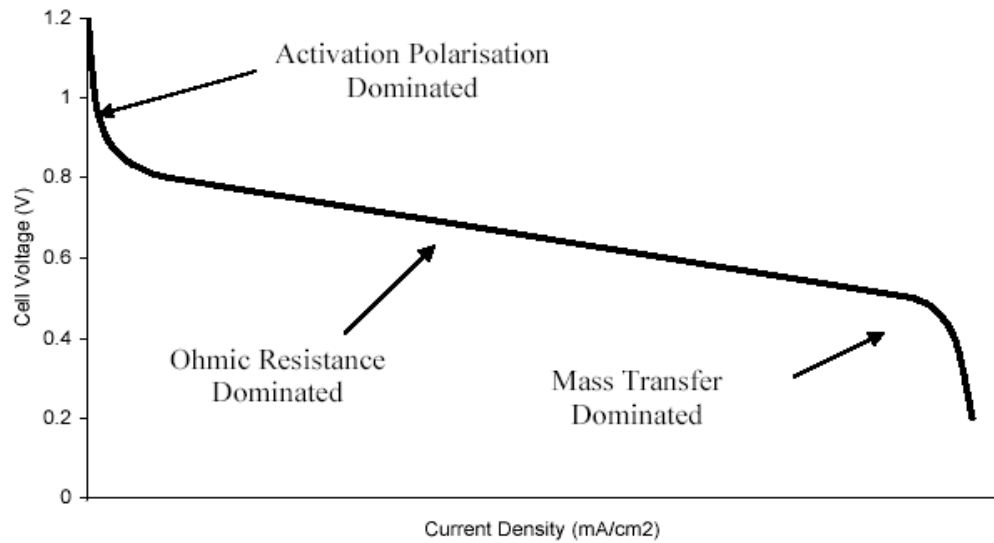
Fig. 1.2 Current - voltage (I - V) characteristics of a fuel cell [5]

There are three distinct regions in the I-V curve representing three different reaction mechanisms. The low current density region is called the activation polarization domain where the charged species have to move through an activation barrier. Approximately 200 mV of potential is lost to overcome the activation barrier. Hence, there is a need of high performance material to reduce this activation barrier.

At high current density region, there will be large concentration of products at the interface site. The products may accumulate at the interface, leading to concentration polarization at the interface. This concentration polarization arises due to inadequate mass transfer of reactants and products. Between the activation and concentration polarization region the current to voltage follows the ohm's law. This region is called ohmic region where most of the fuel cells are operated. All the three polarizations are available at any point of time, however their contribution to the total resistance are different.

The performance of a fuel cell is represented by the power density at a particular temperature. Powder density is the multiplication of voltage to current density of the fuel cell. While drawing current, the cell voltage decreases. Voltage drop is associated with different polarization and ohmic losses in the circuit as well as in the cell. The voltage output is given by:

$$E = E_{eq} - E_L - \eta_{act} - \eta_{iR} - \eta_{diff} \quad \text{......................(1.2)}$$

where, E_{eq} is the equilibrium voltage as calculated from Nernst equation, E_L is the voltage loss due to leaks through the electrolyte, η_{act} is the activation over potential due to slow electrode reactions, η_{iR} is the over potential due to ohmic resistances in the cell and η_{diff} is the over potential due to concentration polarization. E_L is attributed to the gas mixing that may occur through the porous electrolyte layer and improper sealing. Electronic conductivity in electrolyte also leads to loss in voltage and is accounted in E_L.

1.3 Advantages of SOFC

Solid oxide fuel cell is an environmental friendly, pollution free energy conversion system which directly converts chemical energy to electrical energy with high efficiency. Advantages of SOFC are numerous and few are highlighted below.

1. *High efficiency*: SOFC operates at high temperature, hence rate of reaction increases. The byproduct is also a source of heat and can be combined with other energy conversion system to increase the efficiency. The high grade waste heat coming through the byproduct can be coupled with other new energy technologies eg. Micro turbines to increase the overall efficiency. Efficiency of such systems reaches to ~90% with CHP applications with natural fuels [8-10].

2. *Modular design*: All components are solid oxides, so SOFC can be constructed in different shapes and sizes to fulfill the need. There are no moving parts and no corrosive liquids are used. It is a high performance electrochemical device with great reliability and durability.

3. *Fuel flexibility*: SOFC can be operated on all type of hydrocarbon fuels, whereas all other type of fuel cells requires clean hydrogen, free of impurities. Operating the SOFC at high temperature favors internal reforming of the fuel. The fuel can be passed directly at the anode or with reforming. Hydrocarbon fuels like LPG, diesel, petrol methanol, and butane can be used directly in SOFC.

4. *No green house gas and noise*: No noise is produced during the operation of the fuel cell. In the electrochemical reaction water is produced as byproduct along with very little amount of NOx and SO_2 gases in ppm level.

1.4 Candidate SOFC materials

There are three basic components namely, electrolyte, cathode and anode, which constitute the fuel cell. Interconnect and high temperature sealants are the other important materials required for assembling multiple SOFC cells and testing of SOFC cells. Suitable high temperature sealant is used to separate the oxidizing chamber from the fuel chamber. The interconnect helps in collecting current from the electrodes of multi-cell SOFC assembly. All the components should satisfy some basic properties for use in SOFC. These are: chemical, mechanical and thermal stability in the operating conditions, sufficient conductivity, chemical compatibility with other cell components and matching coefficient of thermal expansion (CTE) with other cell components. Fabrication criteria are also important factors governing the performance of the cell. The stability of individual components and the chemical compatibility among the cell materials should be maintained during the fabrication of cells. Finally, the fabrication and processing cost should be kept at a minimum. The requirements of different cell components are described below.

1.4.1 Electrolyte material

In a solid oxide fuel cell, electrolyte is the most important component around which the material selection starts. Therefore, the property of the electrolyte material defines the whole structure of the fuel cell. The following criteria should be met by a material for application as an electrolyte of SOFC.

i. The material should have appreciable oxygen ionic conductivity in the operating temperature regime.

ii. The transport number for oxygen ion conduction should be close to unity, i.e. it should have negligible electronic conductivity.

iii. The material should be stable over a wide range of oxygen partial pressure.

iv. Electrolyte should have good mechanical strength and good thermal shock resistance.

v. Electrolyte should be impervious and free of porosity after fabrication and sintering.

vi. Compatibility with electrodes and interconnect material.

vii. Chemically inert to the fuel cell gases.

Oxides with fluorite structure have been investigated for use as electrolyte. Doped ZrO_2 ceramics having fluorite structure are first investigated as electrolyte material for high temperature operation of the fuel cell between 800-1000 $^\circ$C. Aliovalent metal oxides, such as, CaO, Y_2O_3, Sc_2O_3 and other rare earth oxides form solid solutions with zirconia and stabilize the cubic phase. In addition, these aliovalent oxides introduce vacancies in the oxygen sub-lattice as charge compensating defects. The defect reaction can be presented in Kröger-Vink notation as given below for yttria addition in zirconia.

$$Y_2O_3 \xrightarrow{\ 2ZrO_2\ } 2Y'_{Zr} + 3O^x_O + V^{\bullet\bullet}_O$$
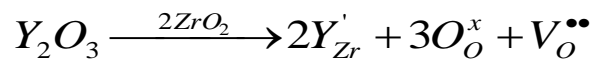
The diffusion of oxygen ions through the vacancies is responsible for the high ionic conduction in yttria stabilized zirconia (YSZ). Oxygen ions hop through the vacancies

and under a potential gradient a net flux of ions takes place resulting in ionic conductivity. The conductivity value depends on the dopant concentration [11]. As the dopant concentration increases concentration of oxygen vacancy increases. It may be apparent that the conductivity will increase with dopant concentration. However, for various zirconia systems it is known that conductivity increases with dopant concentration, exhibits a maximum and subsequently decreases with increasing dopant concentration. Increasing trend in conductivity can be explained by increase in the number of vacancies; whereas decrease in conductivity is associated with decrease of vacancy mobility due to trapping of oxygen vacancies through vacancy clustering or electrostatic interaction [12]. In ZrO_2-Y_2O_3 system the maximum conductivity has been found at 8 mol% Y_2O_3 concentration. Yttria stabilized zirconia (YSZ) is chemically stable and remains a purely oxygen ion conductor over a wide range of oxygen partial pressure [13-14]. Therefore, YSZ is widely used as an electrolyte material for high temperature SOFC.

The oxygen ion conductivity also depends on the microstructure and impurity content. Presence of silica is detrimental to the ionic conductivity in solid oxide electrolytes. Silica segregates at the grain boundary and increases the grain boundary resistivity substantially. Effect of Al_2O_3 impurity on the microstructure, electrical resistivity, mechanical strength and SOFC performance in YSZ electrolyte system was studied by Ishizaki et al.[15]. Alumina addition decreases the total resistance and increases the mechanical strength. The added alumina acts as scavenger of silica and precipitates at the grain boundary.

Doped ceria based electrolyte are studied extensively after YSZ electrolyte material. Compared to zirconia system, higher conductivity of doped ceria system at lower temperature region with lower activation energy makes the material a candidate electrolyte material [16]. Ceria based electrolyte materials have some inherent electronic conductivity at higher temperature and reducing environment. Hence these types of materials are used for intermediate temperature fuel cell applications.

Among the fluorite based electrolyte system, Bi_2O_3-based oxides have also been investigated [17-18]. These materials have conductivity values several orders of magnitude higher than that of YSZ [19-21], at similar condition of temperature and oxygen partial pressure. β-cubic phase in Bi_2O_3-PbO_2 system has conductivity value as high as 1.0 S.cm^{-1} at 600 ^{o}C with a relatively low activation energy (0.4 - 0.5 eV). The disadvantage of a Bi_2O_3 based systems is their stability over a narrow range of oxygen partial pressure and at high temperature [22]. Hence, this system is not pursued largely by researchers.

Solid electrolytes with ABO_3 perovskite structure is another class of materials used for SOFC applications [23-31]. In this system oxygen vacancy is generated by substitution of aliovalent cations at A and B-site. The total conductivity depends on the activation energy for oxygen ion conduction and free volume available for oxygen migration [31]. Some of the well studied perovskite systems are $CaTi_{1-x}Al_xO_{3-\delta}$, $CaTi_{1-x}Mg_xO_{3-\delta}$, $La_{1-x}Ca_xAlO_3$, $BaCe_{1-x}Gd_xO_{3--\delta}$, $SrZr_{1-x}Sc_xO_{3-\delta}$, and doped $LaGaO_3$. Among these materials lanthanum gallate based materials have been proven as alternate promising electrolyte

material for use in intermediate temperature solid oxide fuel cell (IT-SOFC) [32]. Both A site and B-site are substituted by divalent ions for increasing the conductivity value. Among this family, $La_{1-x}Sr_xGa_{1-y}Mg_yO_3$ (LSGM) has been reported to have better conductivity properties [32]. LSGM has significantly higher oxygen ion conductivity than YSZ in the intermediate temperature region and is considered to be a candidate electrolyte material for IT-SOFC. The disadvantage of this system is the instability of the compound and difficulty in preparing single phase LSGM. Insulting phases of $La_4Ga_2O_9$ and $SrLaGa_3O_7$ evolve at the grain boundary during the phase formation and degrades the performance of the fuel cell in the long term operation [32].

1.4.2 Anode materials

In a fuel cell, anode is called the fuel electrode through which fuel is fed to the system. Anode faces the reducing environment at high temperature, 700-1000 ^{o}C. At the anode side hydrogen combines with the oxygen ion at the electrolyte interface. The following criteria should be met by a material for application as an anode for SOFC.

  i.   Good electronic conductivity in reducing environment.

  ii.   Porous enough for the passage of inlet fuel and exit of byproduct (H_2O).

  iii. Good catalytic activity towards hydrogen oxidation reaction.

  iv.   Stability (chemical, mechanical, morphological and phase) in the operating condition.

  v.   Thermal expansion coefficient matching with other cell components.

  vi.   Chemical compatibility with electrolyte and the interconnect material.

Ni, Co, Cu, Ru and Pt are some metals which have better catalytic activity for hydrogen oxygen recombination reaction. Though metals have good catalytic properties towards oxidation of fuels, they cannot be used in the fuel cell operating condition alone. TEC of metals is too high in comparison with the electrolyte material. In order to bring down the TEC of anode structure a composite electrode approach is adopted in which a mixture of metal catalyst and ceramic is used. The ceramic helps in matching the TEC with other cell components. Conventionally, the electrolyte material is chosen to make the ceramic phase of the cermet structure. Ru, Pt and Co if used increases the cost of anode. Hence Ni is widely used as anode material in SOFC. NiO is generally used as precursor of Ni and undergoes reduction in the operating condition of SOFC. The minimum amount of Ni for percolation in YSZ matrix is 30%. In long term operation of the fuel cell coarsening of Ni takes place.

Ni-YSZ, Ni-GDC, Cu-GDC are most extensively used anode materials for SOFC applications. The metallic phase is used for catalytic reaction and electronic conduction in the anode phase. The electrolyte is used to bring down the TEC value close to the electrolyte material. As the reaction is heterogeneous in nature more the reaction sites faster will be the reaction kinetics. The active reaction sites are located at the triple phase boundary (TPB) where ceramic electrolyte, metal catalyst and pores meet together. The TPB length at the anode-electrolyte interface should be maximized for good electrode performance [33]. There should be good percolation path for the electron transfer, oxygen migration and gas diffusion in the anode layer which is controlled by the microstructure. For this purpose fine nickel particles and high electrolyte to nickel ratio is used. Graded

14

microstructure was adopted by many researchers where both fine and coarse electrolyte and Ni particle are used to optimize the microstructure. Mathematical calculation shows 30 vol% metallic phase as the percolation threshold of metallic conduction. Use of fine Ni particles from combustion method alters the electrical properties near the percolation limit [34]. At high temperature, anodes with high nickel content degrade fast due to coarsening of nickel particles. When natural gases are used as fuel carbon deposition on nickel catalyst reduces the catalytic activity. Copper based anode materials have been tried along with ceria based material because of lower C-C bond formation to get rid of the carbon deposition at anode. However, these materials show very low electro-catalytic activity.

Ceria based nickel cermet anode was considered during 1960 [35-37] because of some added advantages of doped ceria compared to YSZ. Ceria has good catalytic activity for carbon oxidation. Hence, fuels cells operating on hydrocarbon fuels or biogas have considerable decrease in the carbon deposition at the anode side. Ceria has some electronic conductivity contribution along with ionic conductivity which helps in increasing the electrocatalytic reaction [36,37]. Nanocrystalline ceria can be infiltrated in the anode to enhance the reaction sites. Presence of nano crystalline ceria is reported to increase the tolerance towards carbon deposition and sulfur poisoning [35,38].

A new class of redox stable $La_{1-x}Sr_xCr_xMn_{1-x}O_3$ (LSCM) anode material has been developed [39-42]. The advantage of this material is that it has good electrochemical activity at both cathode and anode environment and compatibility with many solid

electrolytes. This material has very low electrical conductivity and low ionic transport. However, this can be improved by YSZ or ceria addition in the anode. Another advantage of this material is that it can be used as cathode and or anode in single chamber SOFC.

1.4.3 Cathode materials

Cathode is a porous oxide material through which air/oxygen is passed to the electrolyte. At the cathode-electrolyte interface, reduction of oxygen takes place. The reaction is heterogeneous in nature where the cathode material plays an important role. Cathode alternatively is knows as air electrode in SOFC has to meet the following requirements:

1. High electrical conductivity.

2. Porous enough for transport of oxidant to the reaction site.

3. Stability (chemical, mechanical dimensional and phase) in the operating condition.

4. TEC matching with other cell components.

5. No interaction with electrolyte and the interconnect material (no diffusion of materials).

Doped lanthanum manganites, and doped lanthanum cobaltites are widely used as cathode materials. The dual valency of Mn and Co governs the conduction mechanism in these types of cathodes. The reaction at the cathode-electrolyte interface is very slow and dominates the overall reaction rate of SOFC. Cathode offers major resistance component to the total resistance of SOFC. Suitable material selection and fabrication is must for better realization of a fuel cell.

Manganites

Manganite based perovskite ($Ln_{1-x}A_xMnO_3$) (Ln- lanthanides, A= Ca, Sr, Ba, Pb) materials is a state of art cathode material for its high electronic conductivity, matching thermal expansion co-efficient with many electrolyte materials (e.g. YSZ), and appreciable catalytic activity for oxygen reduction reaction at the cathode-electrolyte interface [43-49]. Lanthanum strontium manganite (LSM) is widely used as a cathode material for fuel cells operating between 800 to 1000 ^{o}C [44-47,50-55]. Nickel and cobalt based cathode materials have higher electronic conductivity and good catalytic activity compared to manganite based cathode material. However, these materials have high thermal expansion coefficient and poor stability. The solubility of the aliovalent dopant like Ca, Sr, Ba and Pb varies from 40-70% in the lanthanum manganate cathode material [48,56-59]. This solubility limit depends on the size of the lanthanide ion.

Manganite systems show some oxygen non-stoichiometry and this amount varies with temperature and doping level. The catalytic properties and transport properties depends on this non-stoichiometry, which is responsible for electronic conductivity and oxygen ion diffusion. The concentration of oxygen vacancy at the cathode surface influences the cathodic polarization and hence the catalytic property [55,60-62]. In air at a temperature below 1000 ^{o}C LSM (Sr =20 mol%) are oxygen-hyperstoichiometric. Beyond this doping concentration, loss of oxygen takes place from the lattice [56,63]. The electrical conductivity of doped lanthanum manganite system increases with increase in dopant concentration as per the following equation.

$$Mn^x_{Mn} + \text{SrO} \xleftrightarrow{\ \ LaMnO3\ \ } Sr'_{La} + Mn^{\cdot}_{Mn} + O^x_O$$
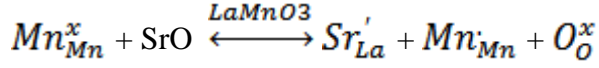
Mn^{4+} concentration increases with Sr^{2+} doping level and is responsible for the increase in conductivity value. At the lower temperature range conductivity maximum is obtained at a substitution level of 20 to 50%. However, this maximum value is obtained at a lower dopant concentration in the higher temperature region. Sakaki et al. have studied the $Ln_{0.7}Sr_{0.3}MnO_3$ (Ln=La-Gd) system where maximum conductivity is obtained for $Nd_{0.7}Sr_{0.3}MnO_3$ at higher temperature region and $Pr_{0.7}Sr_{0.3}MnO_3$ at lower temperature region [65]. Praseodymium based cathode materials ($Pr_{0.6}Sr_{0.4}MnO_3$ and $Pr_{0.7}Ca_{0.3}MnO_3$) have superior properties owing to the Pr^{3+}/Pr^{4+} redox couple and lower interaction with zirconia based electrolyte material [65,66]. $Ln_{1-x}A_xMnO_3$ based cathode materials react with zirconia based electrolyte material resulting in the formation of $AZrO_3$ based perovskite and $Ln_2Zr_2O_7$ type pyrochlore resistive phase [43,55,56,57,59,64-71]. These resistive phases are responsible for the higher interfacial polarization at the cathode electrolyte interface. As the radius of Ln ion decrease, the possibility of formation of zirconia pyrochlore phase decreases [64,65,68,72]. This is attributed to the lower thermodynamic stability of the pyrochlore phase with smaller r_A/r_B ratio.

In the lanthanum manganite based cathode materials partial substitution of manganese with other transition metal ions with stable oxidation state helps in improved thermal expansion, interfacial stability and improves the electrode performance [48,56,57,73-76].

Ferrites

The advantage of ferrite system is that they have TEC close to YSZ and GDC electrolyte systems. However, $LnFeO_3$ system has very low conductivity in the fuel cell operating temperature region. Substitution of acceptor type cations increases the oxygen vacancy concentration and p-type electronic charge carriers in $(Ln_{1-x}A_x)FeO_3$ system. When Sr is substituted at the A sites the charge of $Sr_{Ln}^{\cdot}$ is balanced by either formation of oxygen vacancy or Fe^{4+}. Hence the maximum conductivity is expected when the substitution level is 50% i.e. the ratio of Fe^{3+} to Fe^{4+} is 1:1. [77]. Increasing the dopant concentration above 50% has negative impact on the conductivity due to vacancy ordering and hole localization process. At low oxygen partial pressure oxygen vacancy formation is more favorable because of the formation of $A_{Ln}^{\cdot}$, but at high oxygen partial pressure holes are the predominate charge carriers. At high temperature nonstiochiometry in the ferrite system leads to formation of oxygen vacancy as per the following equation.

$$2Fe_{Fe}^{\cdot} + O_O^x \rightarrow 1/2O_2 + 2Fe_{Fe}^x + \ddot{V}o$$
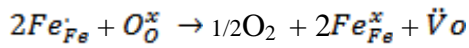
Since the mobility of the electrons or holes is very high compared to the oxygen vacancy/oxygen ions, the conductivity in ferrite system is dominated by holes [77].

Compared to manganite cathodes, perovskite based ferrite cathode materials lose oxygen at elevated temperature unfavorably affecting the TEC and hence are thermochemically incompatible with few solid electrolytes [78-82]. This oxygen loss can be avoided by substitution of iron by cations with stable oxidation state. But substitution of other ions for Fe leads to decrease in the transport number of ions. Ferrite systems are more stable

compared to the cobaltite system as they have stable $3d^5$ electronic configuration. $La_{0.8}Sr_{0.2}FeO_3$ cathode with little lanthanum deficiency showed an ASR value of $0.1 ohm.cm^2$ at 800 °C and has matching TEC with YSZ and GDC electrolyte material [83]. A power density of 900 $mW.cm^{-2}$ was obtained at 700 °C for a cell using this cathode and YSZ as electrolyte [84]. Cu doped LSF shows better kinetics for the oxygen reduction reaction compared to LSF cathode [85]. During sintering of the cathode there was no Zr^{4+} diffusion into the perovskite cathode.

Cobaltite cathodes

Cobaltite based cathode materials have superior cathodic and transport properties compared to the ferrites. However, cobaltites have higher chemical reactivity and higher thermal expansion coefficient [55,56,57,86-101]. $Ln_{1-x}A_xCoO_3$ perovskite shows greater hole delocalization and mobility compared to the manganite or ferrite based cathode materials. $La_{1-x}Sr_xCoO_3$ series is the most studied system in cobaltite cathodes. Substitution of Sr at lanthanum site forms electron holes. The charge neutrality is maintained by formation of $Co_{Co}^{\cdot}$ and oxygen vacancy as per the following equation,

$$Sr_{Sr}^{x} + Co_{Co}^{\cdot} + 2\ddot{V}o = Sr_{La}' + Co_{Co}^{x}$$

$$2Co_{Co}^{\cdot} + O_O^{x} \rightarrow 2Co_{Co}^{x} + \ddot{V}o + 1/2O_2(g)$$
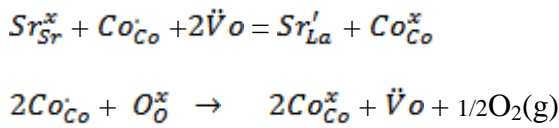
And

$$[\ddot{V}o]\,[Co_{Co}^{x}]^2 = K\ddot{v}o\,[Co_{Co}^{x}]^2\,[O_O^{x}]\,P_{o2}^{-1/2}$$

20

Where $Co^{\cdot}_{Co}$ and Co^{x}_{Co} represents Co^{3+} and Co^{4+} at cobalt site respectively and $K\ddot{v}o$ is the equilibrium constant.

The charge compensation mechanism for the cation deficiency at the Ln side depends on the ratio of Ln/A, temperature and oxygen partial pressure. Cobaltite system is thermodynamically less stable and less tolerant to cation non-stoichometry. Hence synthesis condition influences the structural and electrical data along with microstructure [56,101-103]. Ba^{2+} doping has some positive effect on the oxygen reduction reaction as revealed by many researchers [104-107]. Lanthanum site can be substituted by Gd or Pr for a decreased TEC and ASR values. Cobaltite based cathode materials have higher TEC than the manganite based cathode materials due to the formation of oxygen vacancy and spin state transitions associated with Co^{3+} [108] and weak Co-O bond compared to Mn-O bond [109].

Substitution of Cu at the cobalt site enhances the catalytic property as well as ionic conductivity of $LaSrCoO_3$ cathode material [110]. The dual oxidation state of Pr^{3+}/Pr^{4+} may be utilized by substituting at the A site of $LaSrCoO_3$ to improve the over potential [111]. Zhu et. al [112] substituted Pr and Sr at A side, Cu at the B-site in lanthanum cobaltite cathode and observed improved performance. Few researchers have also substituted Mn at cobalt site, however they have higher TEC [113].

The disadvantages of a cobalt based system are its high TEC value and interaction with YSZ electrolyte material. This inter diffusion mechanism is more pronounced due to lower thermodynamic stability of cobaltite phase [56,114].

Ferro-Cobaltite cathodes

$La_{1-x}Sr_xFe_{1-y}Co_yO_3$ (LSCF) is a state of art cathode material for IT-SOFC because of its good electrical conductivity, excellent oxygen surface exchange co-efficient and oxygen self diffusion co-efficient compared to lanthanum manganite based cathode materials [115-116]. LSCF has a thermal expansion co-efficient close to 13×10^{-6} K^{-1} and do not react with ceria based electrolyte material [117,118]. Electrical conductivity of LSCF based cathode material depends on the Fe content at the Co side and ionic conductivity is controlled by the Sr concentration at the lanthanum site. Cation deficiency at the A site has less effect to the TEC value of the cathode material. LSCF based cathode materials are incompatible to YSZ based electrolyte materials and for this type of cells, an interlayer of GDC is applied between the cathode and electrolyte layer. It has been observed that substitution of multivalent Pr (in PSCF) improves the cathode performance of IT-SOFC [119]. PSCF with composition $Pr_{0.6}Sr_{0.4}Co_{0.8}Fe_{0.2}O_3$ shows a conductivity value of 1040 S cm^{-1} at 300 ^{o}C. The ASR value of a composite of PSCF-GDC (50:50) is 0.046 ohm.cm^2 at 800 ^{o}C. From these results it can be inferred that PSCF is a promising cathode material for IT-SOFC.

For the first time rare earth element free cathode material $Ba_{0.5}Sr_{0.5}Co_{0.8}Fe_{0.2}O_3$ (BSCF) is developed by Haile and Sao [120]. This material showed an ASR value as low as 0.05 ohm.cm^2 at 600 ^{o}C. However this cathode material has very high TEC value for practical use. Another disadvantage of BSCF is that it is susceptible to CO_2 between 450-750 ^{o}C [121].

Nickelate cathodes

$LaNi_{0.6}Fe_{0.4}O_3$ (LNF) is a candidate cathode material having an electronic conductivity of 580 S.cm^{-1} at 800 ^{o}C and TEC of 11.4 x 10^{-6} K^{-1} [122]. This has better TEC value compared to LSM cathode. The biggest disadvantage of this type of cathode is the reaction of LNF with zirconia based electrolyte material and rapid formation of resistive $La_2Zr_2O_7$ pyrochlore phase [123]. However the reaction problem can be avoided by applying a GDC interlayer between the cathode and electrolyte layer.

K_2NiF_4 type La_2NiO_4 is another class of compound having stability at both oxidizing and moderately reducing atmospheres [48,56]. P-type electronic conductivity mechanism dominates over all range of oxygen partial pressure for this type of cathode material with less contribution from hole conduction. These compounds have lower conductivity compared to cobaltite cathode materials. A^{2+} substitution leads to decrease in the oxygen content and increase in the conductivity value detrimental for the performance of cathode material.

1.5 SOFC technology: Critical issues

The performance of a fuel cell is governed by different parameters, such as, cell component materials, fabrication methodology and operating temperature. Processing method has a great role in determining the microstructure of the electrodes, electrolytes and electrode-electrolyte interfaces. Again use of fine powder helps in decreasing the processing temperature during cell fabrication. Starting with fine powders the microstructure can be tailored.

Operating temperature is also important while developing a fuel cell. High temperature operation leads to higher kinetics and higher performance. However, chemical compatibility of cell components, inter-diffusion of chemical species, chemical stability of construction materials and usefulness of sealing are the issues associated with the high temperature operation. Hence, over the last decades thrust has been given to develop SOFC than can be operated in the intermediate temperature range without sacrificing the performance. This challenge has been mitigated by various research groups worldwide through the development of new materials and improvement in fabrication methodologies. In many cases extraordinary performance has been reported in IT-SOFC.

Microstructure has immense effect on the polarization resistance of electrode-electrolyte interface. A numerous literature is available on oxygen reduction reaction at the cathode [124-128] and electrochemical oxidation of hydrogen/fuel at the anode [129-131]. The

reaction sites i.e. the length of the triple phase boundary can be correlated to the polarization resistance. The reaction sites should be increased in order to increase the electrode performance. This can be achieved by adopting suitable ceramic processing techniques.

Cathode materials having mixed ionic-electronic conduction (MIEC) can extend the reaction region and thereby increases the triple phase boundary area. Distribution of MIEC cathode material and pores in finer scale will have more number of reaction sites. Nano-materials can be used as a starting material for tailoring the final microstructure. Excellent electrochemical properties have been reported for nano-structured cathode materials with higher surface area [132]. Nano-structured and functionally graded cathode with graded porosity in the microstructure has been fabricated by CVD method and the cathode is reported to have a reduced interfacial polarization resistance [126]. A maximum power density of 375 mW.cm^{-2} was obtained for the Ni-SDC (samarium doped ceria) anode supported cell with GDC electrolyte and SSC(samarium strontium cobaltite)-SDC cathode fabricated by the above approach.

Nano-structured electrodes with improved performance have been fabricated by wet impregnation technique. In the wet impregnation method the fine nano particles forms a well connected network in the porous electrode and are responsible for this property enhancement [133]. It has been observed that LSCo infiltration to LSM-YSZ composite cathode improved the electrochemical property significantly [134]. The nano-particles

coat the pore wall and oxygen reduction reaction (ORR) within the cathode is enhanced as reflected in the low ASR values obtained in the impedance analysis. However, long term operation of SOFC at high temperature leads to agglomeration of nano-particles and decrease in the catalytic property. Therefore, retaining the nano-structured cathode remains a challenge to researchers.

Synthesis of nanomaterials and their previous history determines the properties as well as the microstructure. Powders prepared by solution route are smaller in size with narrow size distribution and have high surface area. However the cost of material synthesis for large scale production should be considered before a technology development.

Apart from microstructural optimization and development of high performance cathode material, composite cathode approach has been adopted by many researchers [135-148]. In the composite cathode one part is the electronically conducting cathode whereas other part is the electrolyte in definite proportion. The electrolyte component helps in extending the triple phase boundary away from the electrolyte-electrode interface, helps in matching the TEC of cathode with the electrolyte, adheres the electrode layer to the electrolyte, and enhances the microstructural stability of the cathode. For ferrite and cobaltite based materials with high thermal expansion coefficient, composite electrode approach has been adopted to get matching TEC.

1.6 Motivation of work

Long term operation of SOFC with improved performance compelled the material scientists for the development of materials for intermediate temperature fuel cell operation. In general catalytic activity decreases with decrease in temperature. Therefore, to retain the performance at a reasonably high value the materials need to have high catalytic activity. The different materials used for the intermediate operation were briefly described above along with the issues and concerns. Though there is a range of materials for intermediate temperature operation, a particular set of electrolyte and electrode materials have been chosen for the above issues.

The present study is aimed at exploring the beneficial effect of using nano-sized powders in developing IT-SOFC. Gadolinia doped ceria was selected as the electrolyte material. Ni-GDC cermet was studied as the anode material. Based on the literature doped gadolinium cobaltite seems to be a promising material for use as cathode in GDC electrolyte based system and development of this novel cathode material has been explored in the present study. Cell fabrication parameters have been optimized for a better performance.

CHAPTER 2

Experimental Work

The work carried out in this thesis primarily consists of (a) synthesis of fine ceramic powders by wet chemical route for use as SOFC electrolyte and electrodes, (b) characterisation of as-synthesized powders and precursors, (c) study of sintering behaviour of the powders, (d) evaluation of functional properties of each SOFC component materials, (e) integration of electrodes with electrolyte to form symmetric cells and characterization of symmetric cells, and (f) fabrication of single cell and performance evaluation. Microstructural evaluation has been carried out at different stages of the work to correlate with the properties. The experimental procedures adopted in the present work are described below.

2.1 Synthesis of fine powders for SOFC application

Two different wet chemical routes, namely, gel combustion and solution polymerisation route have been adopted to prepare the SOFC materials in this work. Powders of gadolinia doped ceria electrolyte material and nickel oxide anode material have been prepared by gel combustion route. Based on preliminary studies, it has been observed that material containing multiple transition elements can be synthesised in phase pure nano-crystalline form at lower calcinations temperature using solution polymerisation route in comparison with gel combustion route. Therefore, gadolinium cobaltite based cathode materials have been prepared by solution polymerisation route. The details of these two synthesis processes are described as follows.

2.1.1 Gel combustion route

In gel combustion an exothermic reaction between an oxidiser and fuel takes place. Usually metal nitrates are used as the starting materials. These metal nitrates act as oxidizer. Aqueous metal nitrate solution forms gel in combination with complexing agents such as, citric acid, glycine, urea, EDTA etc. These complexing agents act as fuel in the combustion synthesis process. In combustion synthesis the ratio of oxidizer and fuel is fixed in such a way that the net oxidizing valency of the oxidizer becomes equal to the net reducing valency of the fuel. In the present work, citric acid, glycine and urea are used as fuels. Metal nitrates are first dissolved in the deionised water for preparation of stock solution. The metal nitrate solutions in definite ratio are mixed with constant stirring on a hot plate at 80 ^{o}C. Required amount of fuel is added to the mixed nitrate solution and dehydrated on a hot plate with stirring. The metal nitrates form complexes with the chelating agent (fuel). The gel formation takes place with dehydration and further heating of gel leads to combustion. Combustion reaction is a highly exothermic reaction with evolution of large amount of gaseous products in a small time scale. The powder characteristics depend on the exothermicity and evolved gaseous products. Fuel to oxidant ratio has a great role in determining the exothermicity of the reaction. The advantage of a combustion reaction is that final product is often formed in a single step and no calcination is required. However, precursor of the desired product may be formed in some cases. Combustion is a less cumbersome method for the synthesis of oxides, starting with low cost materials. As the metal ions form complexes with the fuels, homogenous distribution of cations takes place. Again the decomposition of the metal fuel complex is exothermic in nature. The released heat during the decomposition of metal-fuel complex is utilised for the phase formation.

2.1.2 Solution polymerisation route

Solution polymerization is a wet chemical process like combustion method. In the wet chemical process the final product may be achieved directly or through an intermediate step. The self sustaining combustion process is very fast and leads to the final product from the molecular mixture instead of any intermediate crystalline phase which on further inter-crystalline mass transfer leads to the final product. However solution polymerization is a method where an amorphous intermediate is formed from the liquid mixture homogenous at the molecular level. This amorphous solid decomposes on heating and thermal reaction at high temperature gives the final product.

Like other wet chemical processes the metal solutions are homogenously mixed to get a complex with a polymerizing agent. In the solution polymerization method sucrose and poly vinyl alcohol (PVA) are taken as polymerizing agent. In this method, stoichiometric amounts of metal nitrates are taken in deionized water. Sucrose and PVA are added to the nitrate solution with constant stirring on a Hot-plate at 80 ^{o}C. The solution pH is adjusted to 1.0 with citric acid. Further heating of the gel after total dehydration leads to fluffy charred mass. This amorphous solid is calcined at desired temperature for phase formation. As the molecules are closely spaced, lower temperature is required for phase formation with better homogeneity compared to the conventional solid state route.

Excess sucrose is added during the synthesis to the metal nitrate solution which is converted to saccaric acid in the acidic medium. Saccaric acid, a good chelating agent, forms complexes with the metal ions in the solution. On a hotplate at a temperature

30

around 200 ^{0}C, PVA (10-20mol %) and saccaric acid undergoes polycondensation (polyesterification) reaction. At the same time dehydration of the gel takes place and lot of water molecules are removed. A viscous gel is formed which on further heating leads to charring of the gel. This amorphous fluffy mass is calcined to form the final product. The advantage of the process is that atomistic distribution of metal ions in the polymer requires lower calcinations temperature for phase formation. A schematic representation of the reaction is shown in Figure 2.1.
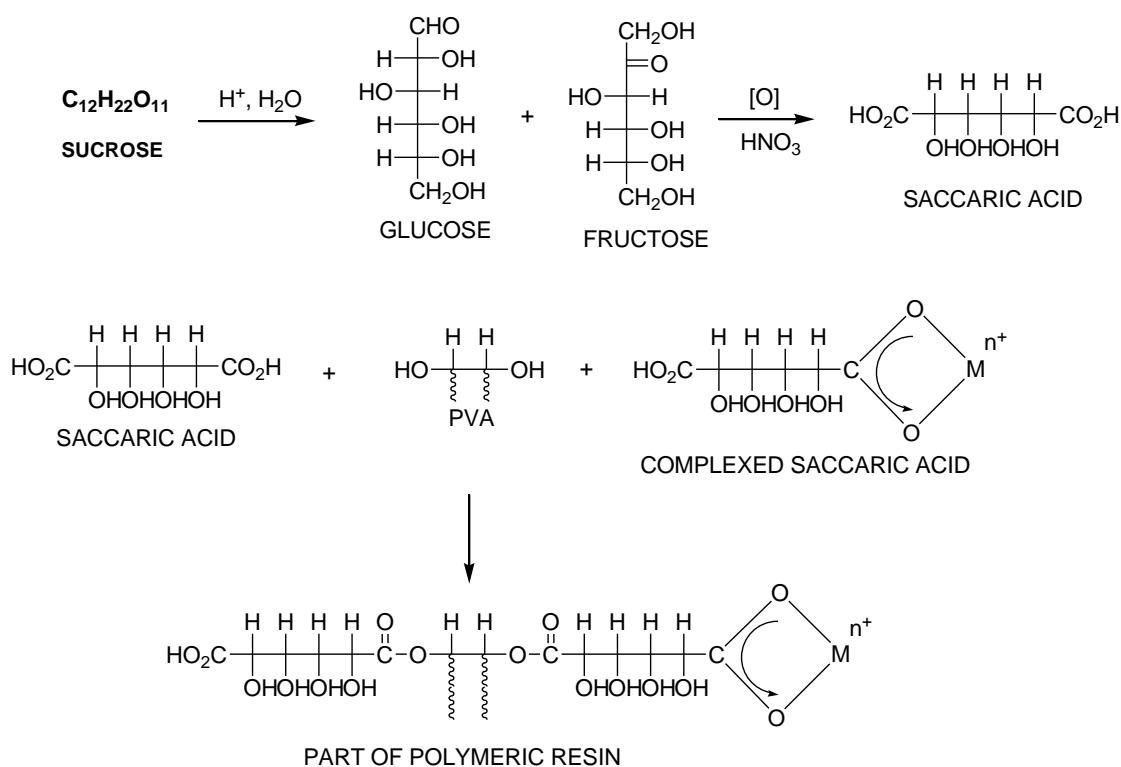
Fig. 2.1: Schematic presentation of solution polymerization reaction.

2.2 characterization of precursor and phase pure powder

2.2.1 Thermal analysis of precursor gel and as-synthesized powders

During the combustion synthesis little amount of gel was taken out and dried separately to remove the water. Thermo-gravimetric analysis of the dried gel precursor was carried out on a TG-DSC instrument (SETARAM make: SETSYS EVOLUTION) to study its thermal decomposition behaviour. Similarly the synthesized powder from combustion and the charred mass from the solution polymerization route were taken for thermal analysis to know the residual carbonaceous materials. All experiments were carried out in flowing air atmosphere in a platinum crucible at a heating rate of $10\ ^o$ C/min. The mass loss with temperature was recorded up to $1000\ ^o$ C. DSC curve was recorded along with the TG curve to ensure any phase change, to observe the nature of decomposition, to calculate the heat capacity and heat of reaction. Always an experiment without the sample was carried out under the same experimental condition as the sample to compensate the instrumental contribution.

2.2.2 X-ray diffraction pattern of powders

Phase analysis of the powders obtained after synthesis and at various stages of synthesis were characterised by X-ray diffraction (Philips, PW 1830) method. Silicon single crystal supplied by the manufacturer was taken for calibration as internal standard. The powder sample was spread thin over a glass slide using a suitable binder. For sintered samples, the sintered masses were ground into fine powder by a

mortar and pestle and then the powder diffraction pattern was recorded. Diffraction patterns were taken between 20-80 degree at an interval of 0.2 degree and 1minute per interval. For better representation few diffraction patterns were taken at a slow scan rate.

2.2.3 Calcination of precursor powders

All the powder synthesis was carried out through a wet chemical process. Carbonaceous materials are used either as a fuel or a complexing (polymerizing) agent, during synthesis. Hence, unreacted reactants or carbon based material may form part of the as-synthesized product. Based on the results of thermal analysis and X-ray diffraction data, the as synthesized powders were calcined at desired temperature for phase formation as well as for removal of carbonaceous materials. All calcinations were carried out in CARBOLITE furnace in static air environment.

2.2.4 Particle size analysis of powders

The Particle size and distribution of powders were measured by a laser diffraction particle size analyser (Model: LA–500, Horiba, Japan). The method of analysis is based on the combination of Fraunhoffer diffraction and Mie's scattering theories. He-Ne laser source is used for light scattering. When laser beam falls on the particles, it is scattered through different angles and the intensity of light at different angles are recorded. The angle of light scattering is inversely proportional to the particle size and the intensity is proportional to the distribution of the particles. Scanning of the angular distribution of scattered light flux provides information on particle size and size distribution. Photomultiplier detectors are arranged at different angles for measuring the light intensity over a wide range of angle.

2.2.5 Specific surface area measurement

Surface force is one among the driving forces for sintering of powder compacts. Hence measurement of surface area gives an idea of reactivity of the combustion-synthesized powder. The specific surface area of the phase pure powders was measured using a surface area analyser (Sorptomatic 1990, Thermoquest, Italy). The principle behind the measurement is the adsorption of mono layer of gas molecules (Nitrogen) on the powder surface and the analysis was based on BET principle. When nitrogen is passed over the sample with pressure, gas molecules are adsorbed on the powder surface and the volume of gas absorbed at different pressure is recorded. From the diameter of the adsorbed molecules, the amount of gas molecules required for monolayer absorption is calculated. Adsorption and desorption both cycles were taken after degassing the sample at 120 ^{o} C. Specific surface area and the particle size are calculated from the surface area data.

2.2.6 Powder morphology by SEM and TEM

Fine particles are produced in the solution synthesis route. Though particle size and distribution is measured by laser diffraction, and surface area by BET principle, the finer details of the powder like morphology and agglomeration nature is not clear. Hence the powder Morphology was studied by scanning electron microscopy (SERON technology, Korea) and Transmission electron microscopy (Philips CM#)/super TWIN). For SEM analysis, powder sample was dispersed in acetone using ultrasonic bath. A drop of this powder suspension was placed on a carbon tape pasted on an aluminium stub. Acetone is evaporated from the stub surface leaving behind the dispersed powder on the stub. For TEM sample preparation, one drop of

the dispersed powder in acetone was put on a copper grid in the similar fashion. Before analysis, the dispersed powder on the carbon tape and cupper grid was coated with gold using a D.C. sputtering unit.

2.2.7 Powder compaction and sintering behaviour by TMA

Compaction of the powder was carried out by a motor driven uniaxial hydraulic press. Steel die with tungsten carbide lining was used for pressing. Pellets of different diameter were prepared followed by sintering for different applications. Pre-compaction was carried out prior to final compaction. Pre-compaction was carried out at 80MPa pressure and final compaction at 150MPa pressure in the hydraulic press. The die-wall was lubricated with stearic acid for smooth operation. For the dilatometric study, green pellets of 8mm diameter were prepared by uniaxial die pressing. For ionic conductivity measurement and symmetric cell measurement pellets were prepared in a die of 15mm diameter. Few electrolyte button cells were prepared in a die of 25mm diameter for cell characterization.

Green pellets in cylindrical shape, of approximately 8 mm diameter x 6 mm height were used for studying the shrinkage behaviour. Linear shrinkage of the sample was recorded at a heating rate of 4 ^{o}C /min in air on a dilatometer (Theta make having two push rods and SETARAM make with single push rod). Data were taken at an interval of 0.4 ^{o}C up to 1400 ^{o}C for ceria samples and up to 1300 ^{o}C for other samples.

Bar pellets were prepared using a rectangular die. The rectangular die was made up of steel with an inner lining of tungsten carbide. These rectangular pellets are used for 4-probe DC conductivity measurement.

2.3 Sintering

From the analysis of the sintering curve, sintering temperature was decided. The temperature at which two third of the sintering takes place is chosen as the sintering temperature. Most of the sintering was carried out in air using a resistance heated muffle furnace (Model: HTF-18, Carbolite, UK). The furnace is programmable and is controlled by auto-tuning Eurotherm PID controller. The furnace has Super Kanthal heating element and LJ – type (Pt 20% Rh – Pt 40% Rh) thermocouple. The heating schedules were decided based on some preliminary experiments and literature reports.

2.4 Fabrication of symmetric cells

For our experiments both electrolyte and electrode supported symmetric cells were fabricated. For the electrolyte supported cells dense electrolyte pellets of 12mm diameter were prepared by uniaxial pressing followed by sintering. Both surfaces were polished near to flatness and cleaned in an ultrasonic bath. Organic slurries of electrolyte-electrode composites (1:1) and electrodes were prepared in terpinol medium. Slurry of the composite was first applied at the two faces and dried in air. Again the cathode slurry was applied on both the sides followed by drying and sintering at the desired temperature. Samples of different kind were sintered at different temperatures based on the shrinkage behaviour. Anode supported symmetric cells are prepared by co-pressing method. First anode material was pressed in a die and electrolyte slurry was applied over the anode compact inside the die. After drying of the slurry again anode material is poured over the electrolyte layer and pressed in the uniaxial die. The co-pressed sample was then co-sintered at desired temperature.

2.5 Characterization of sintered materials

After characterization of the synthesized powders, sintered mass were characterized in terms of microstructure, electrical properties and functional properties. Details of the characterization procedure are mentioned as follows.

2.5.1 Microstructure and composition

One face of the sintered GDC pellet was polished using diamond suspension prior to taking for microstructural study. For polishing diamond particles in the suspensions were 9, 6, 3, 1, ¼ μm for sequential use. The samples were ultrasonically cleaned after polishing followed by thermal etching at 1200 ^{o}C to reveal the grain boundaries. The samples were coated with gold employing a d.c. sputtering unit before taking micrographs in a SEM.

The micrographs were analysed by image analysis software (BIOVIS) for determining the grain size. Average grain size of the sintered samples were measured by line-intercept method where, a line of known length (L) is drawn on the micrograph of the sample and the number of grains intercepted (N) is counted. The ratio of L by N gives the value of average grain size. For better result lines at different places of the micrographs were taken and the average grain size was calculated statistically.

Micrographs of the sintered pellets of cathode and anode materials were taken on the fracture surfaces. Fracture surface was also taken in symmetric cells as well as in a complete cell. Micrographs of the anode materials were taken before and after reduction. The sintered and fracture mass were mounted on an alumina stub. A carbon

tape was put between the alumina stub and the sintered mass. The sample was coated with gold using a d.c. sputtering unit. For EDS analysis, the sample was mounted in a bakelite mould and sample surface was polished using diamond paste. Oxford make EDX was used for this purpose. Gold coating was applied on the sample surface for better conduction.

2.5.2 Measurement of ionic conductivity

2.5.2.1 Coating with platinum paste

The sintered pellets were polished near to flatness at both the faces and cleaned in an ultrasonic bath. Both the faces of the polished pellets were coated with Platinum conductive paste (frit free) procured from M/s ELTECKS Corporation, Bangalore. The coating was allowed to dry at room temperature or under an IR lamp if required. The coating was baked at 1000° C for one hour to remove the organic binders mixed in the platinum paste and to makes a continuous conducting layer. After baking the surface platinum layer conductivity was checked by a multimeter.

2.5.2.2 AC impedance spectroscopy

Impedance spectroscopy was used for characterizing the conductivity behaviour of the electrolyte material. Impedance was measured by a frequency response analyser (SOLARTRON 1260) in the frequency range 0.01 Hz to 10 MHz with PROBOSTAT sample holder (Norweigian Ceramic Society, Norway). The platinum coated sample was fixed in the PROBOSTAT test set-up with two platinum electrodes at both faces of the pellet. Measurements were carried out from 125 ^{o}C to 1000 ^{o}C in air environment. The advantages of AC measurement is to separate the contribution of

grains, grain boundaries and electrodes from a single measurement. Z-plot and Z-view software were used for data presentation and analysis, respectively.

2.5.3 Measurement of electronic conductivity

Electronic conductivity of the material was measured by DC 4-probe method using a sintered bar sample. Two grooves were made in the middle part of the bar at 1cm apart. Platinum paste was applied at the two ends as well as in the grooves followed by baking of the platinum past to reduce the contact resistance. Current was passed though the end terminals of the bar and the voltage was measured through two probes wound over the grooves. The voltage to current response of the material was measures by an in-house set up using a source meter (Kethley-238) in combination with a nano voltmeter (Aligent). For the cathode materials, the electrical conductivity was measured in air; however conductivity of anode materials were measured in the reducing atmosphere.

2.5.4 Evaluation of TEC

Thermal expansion coefficients of the materials were calculated from the dilatometry data. Sintered cylindrical samples of nearly 6mm dia x 3mm height were used for dilatometric study. Thermal expansion was assumed to be isotropic and the linear thermal expansion of the samples were recorded at a heating rate of 10 ^{o}C /min in flowing helium atmosphere using a thermo mechanical analyzer (SETARAM , setsys evolution) with a single push rod. Thermal expansion of a standard Safire sample was taken in the same condition as the sample and the thermal expansion coefficient (TEC) of the samples were corrected by the TEC of Safire.

2.6 Symmetric cell measurement

The symmetric cells prepared by the methods mentioned above are fixed in a PROBOSTAT unit using a spring load. Both the sides of the pellets are attached to two platinum electrodes with platinum mesh. The four electrodes are connected to the four terminal of a frequency response analyzer (Solartron 1260 with the electrochemical interface 1287). Impedance of the symmetric cells was measured at different temperature in the corresponding electrode environment. All cathode symmetric cells were measured in air environment and anode symmetric cells were measured in hydrogen environment. The impedance plots were represented by imaginary plots. Resistance was calculated from the impedance plot fitting into semicircles and area specific resistance of the electrode material in a desired condition was calculated from the symmetric cell data considering the area of the electrode surface. Z-view software was used for analyzing the complex impedance data.

2.7 Fabrication of anode supported cells

Two methods are used for the fabrication of anode supported cells, namely uniaxial die pressing and tape casting method. Anode supported cells of 22mm diameter were fabricated for characterizing the cells. Green pellet of NiO-GDC was prepared by uniaxial die pressing. Slurry of the electrolyte in terpinoel medium was brush painted over the anode layer. After room temperature drying, the half cell was co-sintered at 1300 $^{\circ}$C. Slurry of the cathode material in terpinoel midium was brush painted over the electrolyte layer and calcined at 1100 $^{\circ}$C. Platinum paste was applied over the two sides of the pellet and baked at desired temperature.

   For cell fabrication by tape casting, slurries of anode and electrolyte were prepared in organic medium. The organic slurry was casted on a mylar film fixed on a glass

plate using a doctors' blade tape casting machine. The doctor's blade is forced to move by an electric motor with definite control over speed. First electrolyte layer was casted followed by anode layer. The two layers were then co-sintered at 1300 ^oC. Slurry of the cathode was applied over the sintered electrolyte layer and sintered at 1100 ^oC. Platinum paste was applied over the two sides of the pellet and baked.

2.8 characterization of single cell

The cell tests were carried out using probostat cell test setup. This full cell was mounted over an alumina tube by ceramic sealant (CERABOND 885). The sealant was baked at different temperatures as recommended by the supplier. Platinum mesh connected with platinum wire was used as current collector and fixed at opposite faces of the cell. The single cells in disc shape attached to the test set up is heated in a controlled rate with oxygen gas flowing through the cathode side and moist hydrogen at the anode side. For passing humidified hydrogen in the anode side, hydrogen was bubbling through water for absorbing water. The sealing between the sample and the alumina holder was checked by a hydrogen leak detector. At different temperatures the current to voltage response was checked using a Nano-voltmeter (Aligent) and a source meter (kethley model-238). After the experiment, the SEM micrograph of the facture surfaces was taken by a scanning electron microscope.

CHAPTER 3

Synthesis and characterization of GDC electrolyte material

3.1 Introduction

Ceria based oxide materials are used as electrolytes for intermediate temperature solid oxide fuel cell (IT-SOFC) applications. Gadolinia doped ceria (GDC) is a potential solid electrolyte for intermediate temperature solid oxide fuel cell system because of its high ionic conductivity in low temperature range (500 – 700°C) [149]. When gadolinia is substituted in ceria, it introduces vacancies in the oxygen sub-lattice as charge compensating defects responsible for oxide ion conductivity through these vacancies. The oxide ion conductivity increases with increase in temperature following Arrhenius equation. At a given temperature, conductivity increases with increase in substitution level, and decreases after attaining a peak in the conductivity value. Ceria doped with 12 mol% gadolinia is reported to have maximum conductivity in the ceria-gadolinia system [118]. The high oxygen ion conductivity has led to its use as a solid oxide electrolyte in various electrochemical applications [150]. However, at higher temperatures and reducing environments the valency state of cerium ions starts changing from Ce^{4+} to Ce^{3+} [151]. This phenomenon introduces

electronic conductivity in the GDC material and restricts its use. Nevertheless, the ionic conductivity and the ionic transport number is appreciable in 12 mol% gadolinia doped ceria for its use as electrolyte in the intermediate temperature (600 – 700 ^{o}C) solid oxide fuel cells (IT-SOFC).

A wide variety of processes are available for the synthesis of mixed oxide ceramic powders. Doped ceria powder has been reported to be synthesized by various wet chemical routes, such as, co-precipitation [152, 153], hydrothermal [154], sol-gel [150], salt assisted aerosol decomposition [155], and gel combustion [156] route. With appropriate processing parameters these wet chemical processes can produce nano-size powders in narrow particle size distribution. The synthesis of ultrafine ceria powder is of particular importance in order to get dense sintered product at a sintering temperature that is lower than the temperature at which valency state of cerium ($Ce^{4+} \rightarrow Ce^{3+}$) starts changing. Among the above mentioned processes, the gel combustion process is characterized by fast reaction rate and low cost. In the gel combustion route a self-sustaining exothermic redox reaction is allowed to take place in the gel that is formed on dehydrating an aqueous solution of a fuel (such as, polycarboxilic acid) and an oxidant (metal nitrate). The fuel also acts as a complexing agent in the aqueous solution of nitrate salts. The powder characteristics, such as, phase purity, crystallite size, particle size, nature (hard or soft) of agglomeration, are influenced by gel stability, exothermic heat, flame temperature, time of reaction and moles of gases evolved. Further, these parameters are dependent on chemistry of fuel and fuel-to-oxidant ratio.

In the present investigation fine and nano-crystalline 12 mol% gadolinia doped ceria powders have been prepared by gel combustion route using three different fuels, namely, citric acid, glycine and urea. The fuel-to-oxidant ratio has been taken as per stoichiometric reaction [157]. The characteristics of the processes have been studied by thermal analysis of gel precursor. The processes have been analyzed through thermodynamic calculation. Physical properties of powders prepared using different fuels were characterized and correlated with the process thermodynamics. Based on the characteristics of GDC powders synthesized using different fuels, metal nitrate - citric acid gel combustion route was chosen for the preparation of doped ceria powders of various compositions (3, 4, 6, 8, 10, 12, 15 and 18 mol% GDC) for further studies (sintering and electrical behavior).

On firing a green pellet shrinkage takes place leading to densification. The shrinkage behavior depends on the powder characteristics. The powder characteristics have been reported to be influenced by the dopant concentration [158]. Further, addition of dopant in ceria increases the defect concentration and may play an important role in the densification process. Comparative study of shrinkage behavior of ceria with different level of substitution is limited in the literature. In the present study, the shrinkage behavior of combustion synthesized pure ceria and doped ceria powders of two different compositions have been studied using a dilatometer.

3.2 *Experimental*

Cerium (III) nitrate hexahydrate (purity: 99.9%, Indian Rare Earths Limited, India) and gadolinium (III) nitrate hexahydrate (purity: 99.9%, Indian Rare Earths Limited, India) were dissolved in deionised water for preparation of stock solution. Required

volume of the stock solutions were taken and mixed. Different fuels (citric acid, glycine and urea) were added separately to the mixed nitrate solution. The molar ratios of fuel to metal nitrates were 5:6, 5:3 and 5:2 for citric acid, glycine and urea fuels, respectively. In each case the solution was dehydrated slowly on a hot plate forming viscous gel. On further heating, auto-ignition of the gel took place with evolution of large amount of gaseous molecules. The flow sheet for the synthesis of gadolinia doped ceria powder is shown in Fig. 3.1. Combined thermogravimetry and differential scanning calorimetry (TG-DSC) (Setaram, Model: 92-16.18) of the gel precursors were carried out in the temperature range from 25 to 900 ^{o}C in flowing oxygen environment with a heating rate of 10 ^{o}C/min. Based on the thermogravimetric results, the powder synthesized by urea route was calcined at 700 ^{o}C. This calcined powder was used for particle size analysis and sintering study. In case of citric acid and glycine route as-synthesized powders were used for particle size analysis and sintering study.

The powders were pre-compacted by cold pressing at 75 MPa pressure using a uniaxial hydraulic press. The final compaction was done with at a pressure of 150 MPa. The green pellets from all the three routes were sintered at 1250 ^{o}C. Densities of the sintered pellets were determined using Archimedes principle. The microstructures of the sintered pellets were studied using a scanning electron microscope (SEM) (SERON technology, Korea).
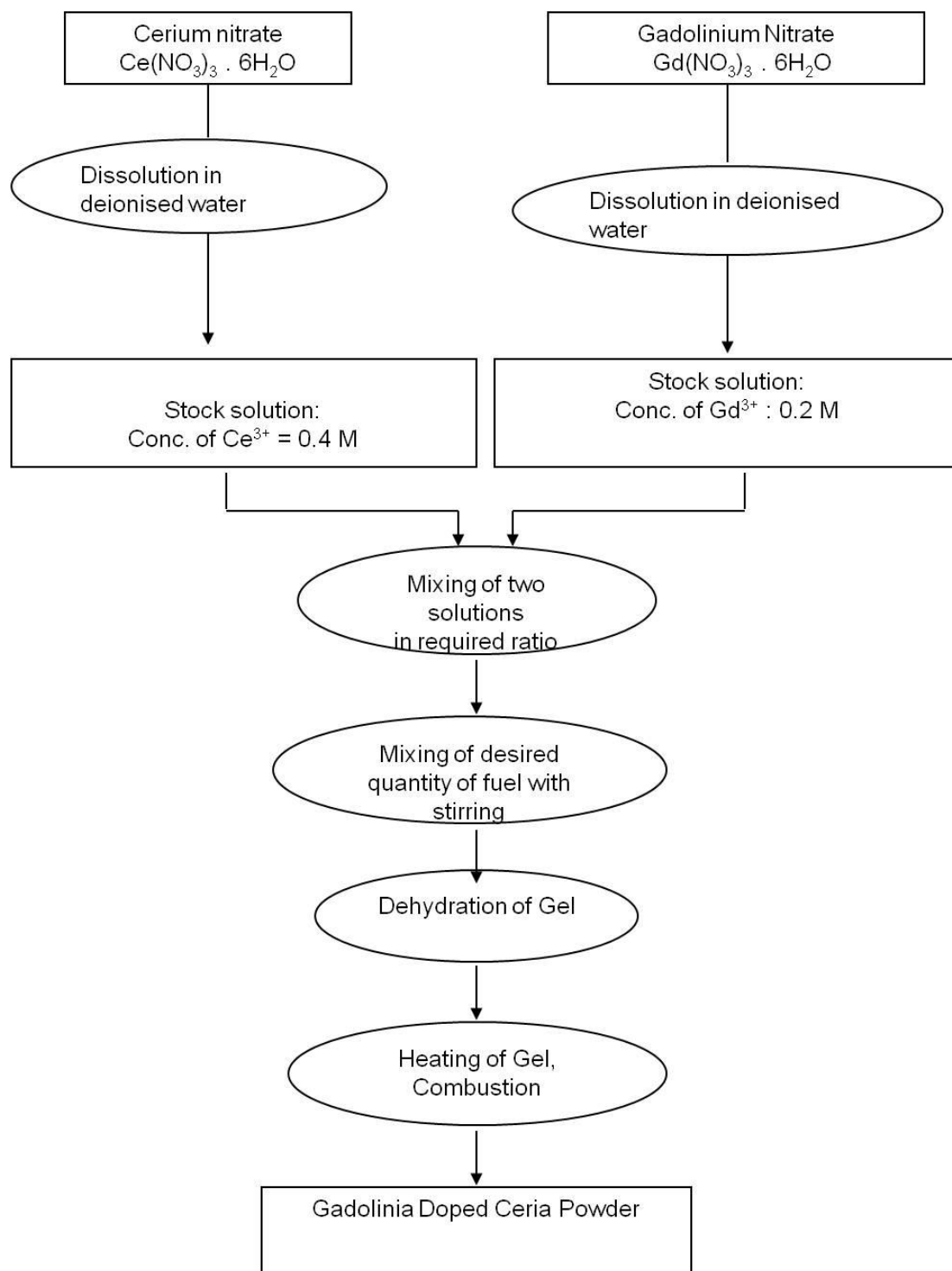
Fig. 3.1 Flow sheet for synthesis of GDC powder by combustion route

Based on the powder properties, citric acid fuel was found to give optimum results in terms of production of fine powder in narrow size distribution. Hence for further studies GDC powders with different gadoloinia substitution level (3, 4, 6, 8, 10, 12, 15 and 18 mol% GDC) were synthesized by citrate nitrate gel combustion route. The powders were characterized in terms of particle size, surface area and crystallite size by X-ray diffraction. The shrinkage behavior of GDC with different level of gadolinia substitution was studied using a dilatometer (Model: SETARAM evolution 1700) under constant rate of heating (4°C/min.).

3.3 Results and discussion

Gel combustion is an exothermic reaction between an oxidizer and a fuel. Metal nitrates are used as oxidizer and citric acid, glycine, urea, EDTA, etc are the probable fuels. These fuels form complexes with metal nitrates in the aqueous media and their decomposition reactions are exothermic in nature. This exothermic heat is used for phase formation during synthesis. In many cases desired phase is obtained during combustion. However in some cases, the precursor of the desired phase is formed which needs further calcination for phase formation. The residual carbonaceous materials are also removed during calcination. Either a single fuel or a mixture of two fuels in definite ratio can be used for combustion. In the present study citric acid, glycine and urea are used as fuels to study the effect of fuel on powder characteristics.

3.3.1 Combustion reactions: theoretical analysis

As per the propellant chemistry, the ratio of fuel to oxidant in a combustion reaction is fixed in such a way that the net reducing valency of the fuel equals to the net oxidizing valency of the oxidant. The oxidizing valencies of the oxidants and the reducing valences of different fuels are given in Table 3.1. The molar ratio of fuel to metal nitrate has been determined based on the above concept. It may be mentioned here that the reducing valencies of nitrogen and carbon have been taken as 0 and 4, respectively, considering N_2 and CO_2 as the gaseous combustion products. Presence of these gaseous states in the evolved combustion product has been reported in the literature [157]. For evaluating the relative exothermicity of combustion reactions involving different fuels, a simplified theoretical approach has been taken. This approach is similar to that reported by Purohit et al. [155]. The following combustion reactions that are balanced to give pure ceria have been considered.

Table 3.1 Oxidizing and reducing valencies of oxidants and fuels used in the study

Compound	Derivation	Valency oxidizing (-) reducing (+)
Oxidizers		
$M(NO_3)_3$ M = Ce, Gd	3+3.{0+3.(-2)}	-15
Fuels		
Citric acid ($C_6H_8O_7$)	6.(4)+8.(1)+7.(-2)	18
Glycine ($C_2H_5NO_2$)	2.(4)+5.(1)+0+2.(-2)	9
Urea (CH_4N_2O)	4+4.(1)+2.(0)+(-2)	6

Fuel: Citric acid

$$Ce(NO_3)_3 \cdot 6H_2O_{(C)} + \frac{5}{6}C_6H_8O_7 \cdot H_2O_{(C)} + \frac{1}{4}O_{2(g)} \rightarrow CeO_{2(C)} + \frac{3}{2}N_{2(g)} + 5CO_{2(g)} + \frac{61}{6}H_2O_{(g)}$$

…..(3.1a)

Fuel: Glycine

$$Ce(NO_3)_3 \cdot 6H_2O_{(c)} + \frac{15}{9}NH_2CH_2COOH_{(C)} + \frac{1}{4}O_{2(g)} \rightarrow CeO_{2\,(C)} + \frac{7}{3}N_{2(g)} + \frac{10}{3}CO_{2(g)} + \frac{61}{6}H_2O_{(g)}$$

…..(3.1b)

Fuel: Urea

$$Ce(NO_3)_3 \cdot 6H_2O_{(C)} + \frac{5}{2}NH_2CONH_{2(C)} + \frac{1}{4}O_{2(g)} \rightarrow CeO_{2(C)} + 4N_{2(g)} + \frac{5}{2}CO_{2(g)} + 11H_2O_{(g)}$$

…..(3.1c)
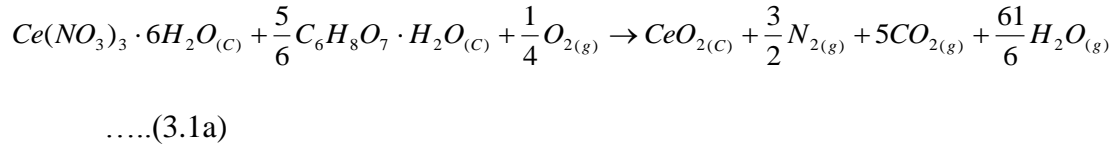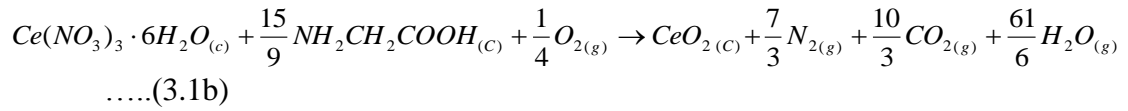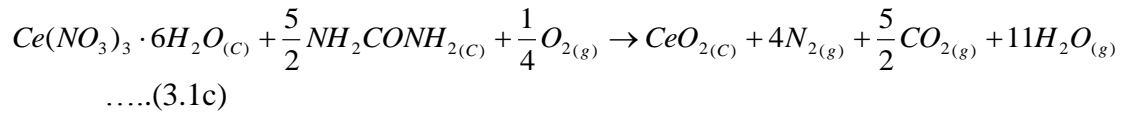
Heat of combustion reaction has been determined using the relation:

$$\Delta H_{combustion} = \left(\sum \Delta H_f\right)_{products} - \left(\sum \Delta H_f\right)_{reac\tan ts} \qquad …..(3.2)$$

The combustion reactions have been found to occur on dehydration of gel at a temperature above the ambient. However, for simplification in the calculation of exothermic heat, the reaction temperature has been assumed to be 298 K. The heat evolved in the combustion will raise the temperature of the products. In a complete combustion reaction total reactants are converted into product in a very small time scale. With this condition the system has been assumed to be adiabatic and the adiabatic flame temperature can be calculated by solving the equation:

$$\Delta H_{combustion} = \int_{298}^{T_{ad}} (\Sigma n C_P)_{products} dT \qquad .....(3.3)$$

where, n is the number of moles of a reaction product and T_{ad} is the adiabatic flame temperature. The calculated thermodynamic quantities of combustion reactions of cerium nitrate with different fuels are given in Table 3.2. The values indicate that the heat of combustion is significant for all the three fuels and the heat can raise the temperature of the products (referred as adiabatic flame temperature) above 1100 ^{o}C. It may be mentioned here that in the time scale longer than the combustion reaction time the experimental condition is far from adiabatic and hence, the temperature rise will be for a very short period. The differences in the total amount of evolved gases in the combustion reactions using the three different fuels are not significant. Thus the variation in the product characteristics will be predominantly dependent on the reaction kinetics.

Table 3.2 Calculated thermodynamic quantities of combustion reaction using different fuels

Fuel	$\Delta H^{298}_{combustion}$ (kcal/mol)	Adiabatic flame temperature T(^{o}C)	Total no. of moles of evolved gases (per mole of CeO_2)
Citric acid	-222.741	1170	16.66
Glycine	-221.789	1248	15.83
Urea	-202.668	1103	17.50

3.3.2 Thermal studies on precursor gels formed using different fuels

In citric acid and glycine route the combustion reaction was found to propagate through the reaction container and the powder was voluminous with uniform light yellow in color. When glycine was used as fuel, the reaction was more vigorous and the product yield was low. However, citric acid as a fuel, showed a controlled combustion reaction with better product yield. In case of urea route the reaction was found to be localized and the powder obtained was less voluminous. The colour of the powder was yellow with distributed intensity.

TG-DSC results of the gel precursors formed using different fuels are shown in Figures 3.2(a-c). Exothermic peak associated with sharp weight loss was observed in each case. This feature indicates the occurrence of a combustion reaction. The combustion reactions start at around 178, 192 and 235 ^{o}C in case of citric acid, glycine and urea fuels, respectively. It is observed that the reaction initiates at a higher temperature when the heat of combustion is less (ref. Table 3.2). No weight loss was observed after the combustion reaction when citric acid and glycine were used as fuel. This indicates complete combustion reaction giving a product free of residual reactants and carbonaceous matter. In case of urea fuel weight loss continues up to 700 ^{o}C. This indicates incomplete combustion of oxidant and fuel. Based on the TGA result the powder prepared by urea route has been calcined at 700 ^{o}C. The results indicate that the exothermic heat is adequate for combustion to take place when glycine and citric acid are used as fuel. The calculated values of exothermic heat of combustion and adiabatic flame temperature for urea fuel are lower than that of glycine and citric acid fuel. However, the values are significant to support a
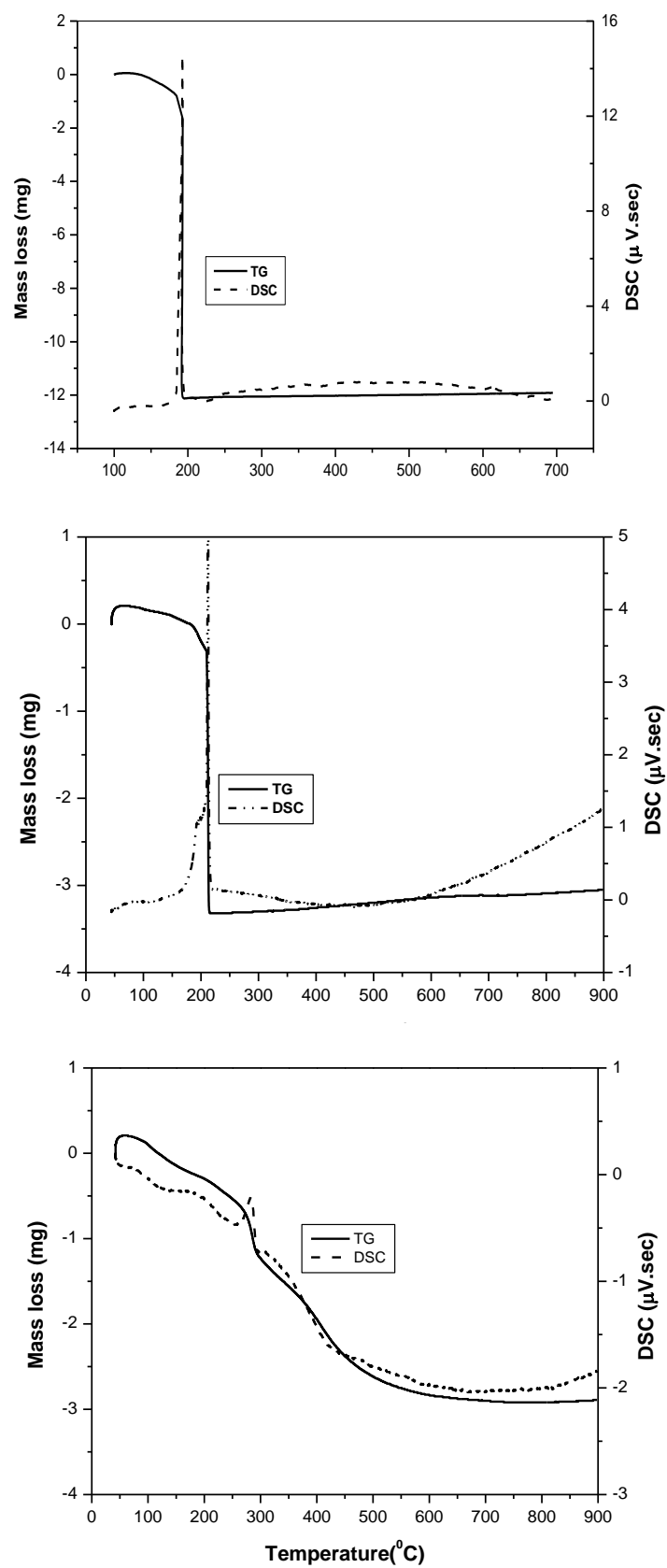
Fig.3.2 TG-DSC of gel precursors formed using different fuels; (a) citric acid (b)

glycine and (c) urea

combustion reaction. Inspite of this, the combustion reaction remains localized and incomplete in case of urea fuel. This may be attributed to inhomogeneous precursor formed out of an unstable gel. In such case the combustion heat can be dissipated to the surrounding colder region where fuel to oxidant ratio is not favorable for combustion and consequently the flame temperature would significantly decrease. In urea route the pH condition changes significantly on dehydration of the gel and might have lead to partial precipitation of weakly coordinated precursors. The continuous mass loss at later stage in the TG curve (Fig3.2c) is attributed to decomposition of weakly coordinated precursor. The results indicate that intimate mixing of the oxidant and fuel in the form of a stable gel is necessary for propagation of combustion reaction.

3.3.3   Thermal studies on precursor gels of different gadolinia content

In order to study the effect of gadolinia doping on combustion behavior of the gel precursor, three different compositions of gadolinia doped ceria (0, 4 and 18 mol% Gd) were synthesized using citrate-nitrate gel combustion route. The TG patterns of the precursor gels for the three compositions in flowing oxygen environment are shown in Fig. 3.3. It has been observed that major weight loss occurs in the temperature range of 178-192 ^{o}C for pure ceria, 187-206 ^{o}C for 4GDC and 210-230 ^{o}C for 18GDC. The weight loss in the narrow temperature range is due to combustion reaction of a precursor gel. As the gadolinia content increases, the combustion initiation temperature and final temperature both increase. Major weight loss took place in the combustion reaction. No detectable weight loss was observed after the combustion. It confirms that for all compositions the combustion synthesized powder is phase pure and free of carbonaceous material when stiochiometric ratio of fuel to

53

oxidant was used. The combustion reaction occurs with a large volume of evolved gases. This leads to physical loss of some amount of mass from the TG crucible. Therefore quantitative information could not be obtained from TG plot.
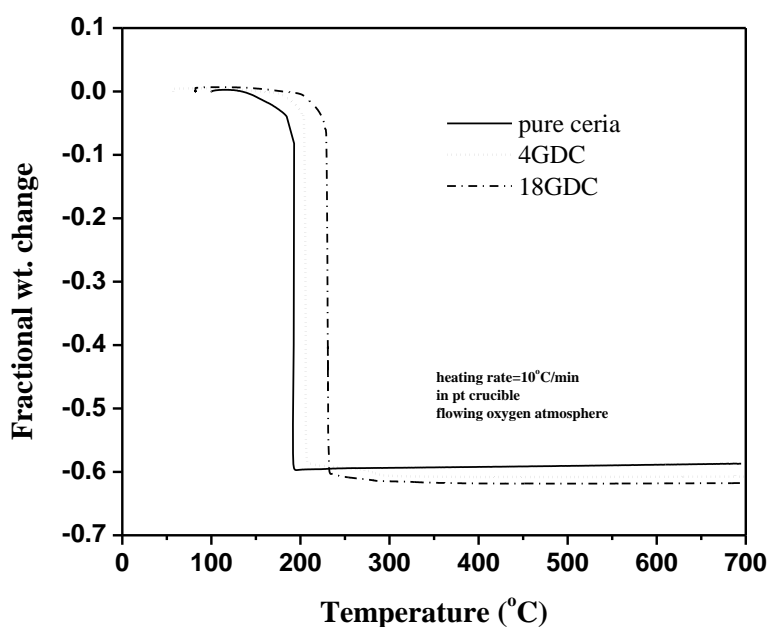
Fig.3.3. TG patterns of the gel precursors of pure ceria, 4GDC and 18GDC in flowing oxygen atmosphere

3.3.3 Effect of fuel on powder characteristics

X-ray diffraction (XRD) patterns of the powder samples obtained after combustion synthesis using three different fuels are shown in Fig. 3.4. In case of urea fuel calcined powder was used for recording XRD pattern. In all the three cases single phase fluorite structure was obtained. The presence of broad peaks in the diffraction pattern indicates the nano-crystalline nature of the powders. The broadening of the

peak is generally expressed in terms of FWHM (full width at half maximum). The crystallite size has been calculated from FWHM data using Scherrer formula;

$$D = \frac{0.9\lambda}{\beta.\cos\theta}$$ ….. (3.4)

where, D is the crystallite size in nm, λ is the radiation wavelength (0.154056 nm in present case, Cu K_α), 2θ is the diffraction angle, and β is the corrected line width at half peak intensity. β can be calculated using the formula:

$$\beta^2 = \beta^2_m - \beta^2_s$$ …..(3.5)

where β_m is the measured FWHM and β_s is the FWHM of a standard silicon sample.

The reflection from (111) plane was used for determination of average crystallite size. The crystallite sizes as determined using Scherrer formula are 7, 16 and 14 nm for citric acid, glycine and urea fuel, respectively. The largest crystallite size is obtained in case of glycine route. This can be attributed to the highest adiabatic flame
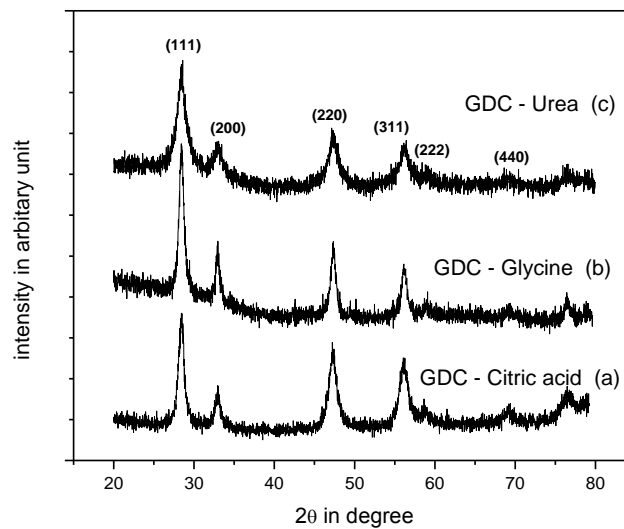
Fig. 3.4 XRD patterns of the powder samples obtained after combustion synthesis using different fuels (a) citric acid (b) glycine and (c) urea

temperature. The powder synthesized by urea route has smallest crystallite size among these three routes. In case of urea route the combustion reaction did not propagate and the condition is far from the adiabatic. Hence, the flame temperature must have been much less than that predicted in Table 3.2. Consequently, the crystallite size should be smallest in this case. However for the removal of carbonaceous materials, the powder was calcined. Therefore the crystallite size increases. TEM images of the combustion synthesized powders prepared using three different fuels are shown in Fig.3.5. The TEM crystallite size data conforms well to the crystallite sizes obtained by Scherrer formula. TEM images show that the crystallites which are often referred as primary particles get agglomerated.

The particle size has been measured for as combustion synthesized powder obtained in citric acid and glycine route. However, for urea route the particle size has been referred for powders calcined at 700 ^{o}C. The powder prepared through citric acid and glycine route show monomodal distribution with median particle sizes 0.4 and 0.43 μm, respectively. However for powders synthesized by urea route bimodal distribution is observed with modes at 0.4 and 1.87 μm, respectively. The larger particle size in urea route indicates formation of agglomerates which do not break on ultrasonic treatment. These large agglomerates are formed during calcinations at 700 ^{o}C where partial sintering of powder takes place.
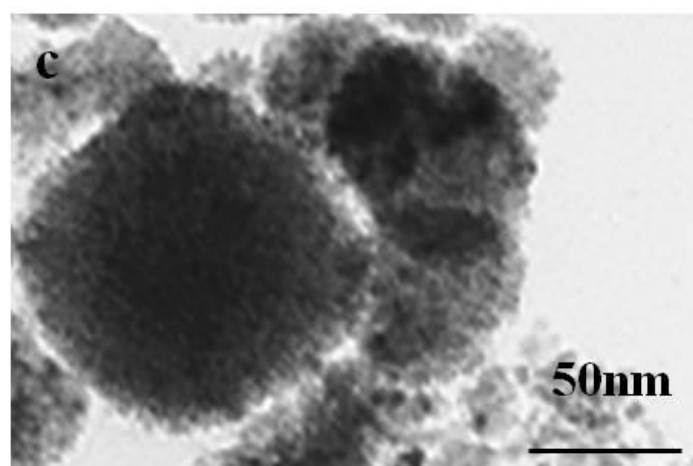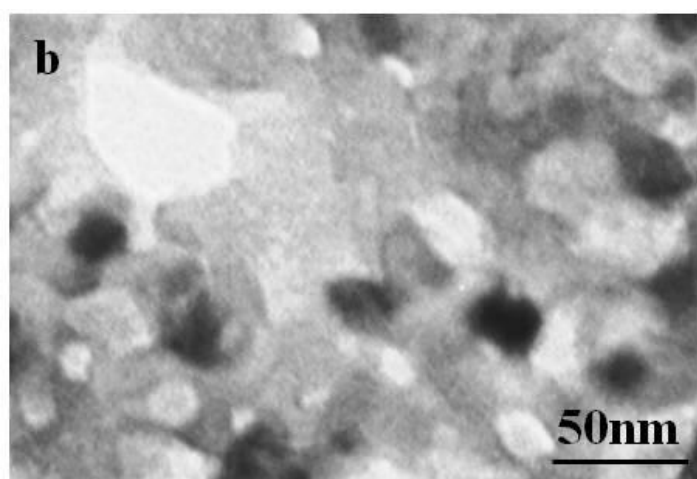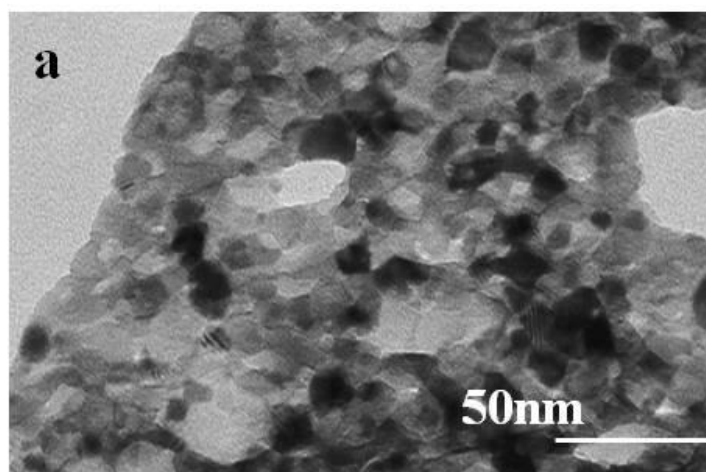
Fig. 3.5 TEM images of the combustion synthesized powders; (a) citric acid route, (b) glycine route and (c) urea route

The densities obtained after sintering at 1250 ^{o}C, 3 h are 98%, 96%, and 86% of the theoretical density for powders prepared through citric acid, glycine and urea route, respectively. The lowest density in urea route is because of presence of hard agglomerates which are difficult to break during compaction. SEM pictures of the sintered pellets are shown in figures 3.6(a-c). The microstructures show submicron grain size. The grain sizes are relatively small in the sintered pellet obtained through urea route. This may be attributed to the lower reactivity of the calcined powder used for sintering

3.3.3 Effect of gadolinia content on powder characteristics

To study the effect of gadolinia concentration on crystallite size, three compositions were selected. Variation of crystallite size with composition for pure ceria, 4 and 18 mol% gadolinia doped ceria is shown in Table 3.3. The crystallite size decreases with increase in gadolinia substitution. The average measured particle sizes and surface areas of different GDC compositions are given in the Table 3.3. The equivalent spherical diameter of the particles has been calculated using the relation:

$$D = \frac{6000}{\rho S} \qquad \qquad \text{.........(3.6)}$$

where, D is the equivalent spherical diameter of the particles (in nm), ρ is the density of the material (in g/cm^3) and S is the measured surface area (in m^2/g). In these calculations the densities for different compositions have been obtained from lattice parameters reported in literature in the form of Vegard's law [156]. The density values taken are 7.24, 7.23 and 7.20 g/cm^3 for pure ceria, 4GDC and 18GDC, respectively.

58
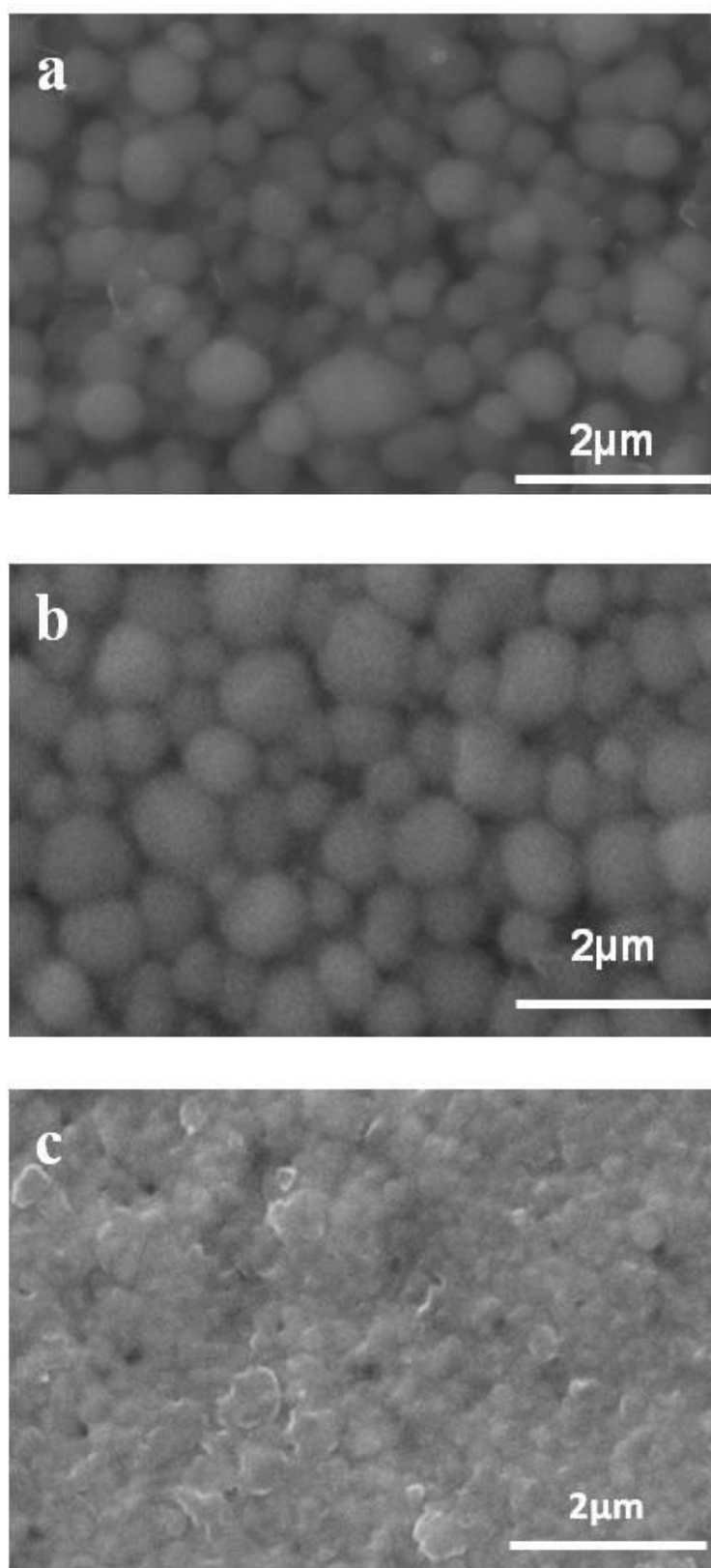
Fig. 3.6 SEM of sintered pellets; (a) citric acid route, (b) glycine route (c) urea route

The values of equivalent particle size are too low in comparison to measured particle size. However, the values are closer to the crystallite sizes. These observations indicate that particles are in agglomerate form of primary particles which are single crystallites. In agglomerates, the primary particles are bonded together by forming necks at the active contact points. The degree of agglomeration increases with increase in gadolinia content as indicated in the variation in particle size. This may be attributed to the more reactive surfaces of the primary particles as the gadolinia concentration increases. With increase in gadolinia concentration the oxygen vacancy concentration increases both in the lattice and on the surface of the primary particles. This makes the surfaces more reactive for higher gadolinia content GDC material. Further, with decrease in crystallite size the total surface area (defective region) increases thus enhancing surface diffusion leading to neck formation during combustion. Neck formation effectively reduces the surface area of agglomerate particles. This is manifested in the lower value of measured surface area compared to crystallite size equivalent surface area as given in Table 3.3.

Table 3.3: Crystallite size, particle size and surface area of combustion synthesized ceria and doped ceria powders

	Pure ceria	4GDC	18GDC
Crystallite size (nm)	18	11	8
Particle size (nm)	510	620	1210
Surface area (m^2/g)	41	44	50
Surface area equivalent particle size (nm)	20	19	17
Crystallite size equivalent surface area (m^2/g)	46	76	104

3.3.5 Sintering behavior of Gd doped CeO$_2$: Effect of Gd content

Three different compositions of GDC were taken for studying the effect of gadolinia content on sintering behaviors. The linear shrinkage as obtained from dilatometric experiment is shown in Fig. 3.7 for all the three compositions. The shrinkage behavior is found to be dependent on the dopant concentration. An initial shrinkage at lower temperatures (e.g. below 500 ^{o}C for 18GDC) is observed in the samples. This becomes prominent at higher gadolinia content samples. During compaction the rearrangement of agglomerates takes place, and contact points develop among the agglomerates. On heating neck formation takes place at the contact points by surface diffusion followed by densification through grain boundary and volume diffusion. As the surface area of 18GDC is more, the initial shrinkage becomes more prominent in this composition.

Significant shrinkage sets in at around 625, 525 and 455 ^{o}C for pure ceria, 4GDC and 18GDC, respectively. This shrinkage is due to the growth of neck regions which are already developed among the primary particles. The decrease in shrinkage initiation temperature is again due to the more reactive particles of higher dopant concentration. Although the shrinkage sets in at a lower temperature the densification process is completed at higher temperature when the dopant concentration is high. It is found that for pure ceria near theoretical density is obtained on firing up to 1100 ^{o}C. The densification process for 4GDC composition completes at around 1225 ^{o}C. This temperature is more than 1400 ^{o}C for 18GDC composition. Shrinkage is found to occur in wider temperature range as gadolinia content increases. As mentioned earlier, the degree of agglomeration increases with increase in gadolinia content. It is likely

that the agglomerates will be harder at higher gadolinia content. Although the hard agglomerates rearrange themselves during cold pressing these may not break completely. This will leave larger inter-particle pores in the green compact. It may be mentioned here that within the agglomerate the pores will be much smaller. Thus the green compact will contain pores with wider distribution in the size of pores. The larger pores take higher temperature and longer time to shrink. Soft agglomerates, as can be expected in pure ceria powder, are likely to break during green compaction and the larger interparticle pores will be eliminated. Hence, densification has been found to occur over a narrow temperature range.
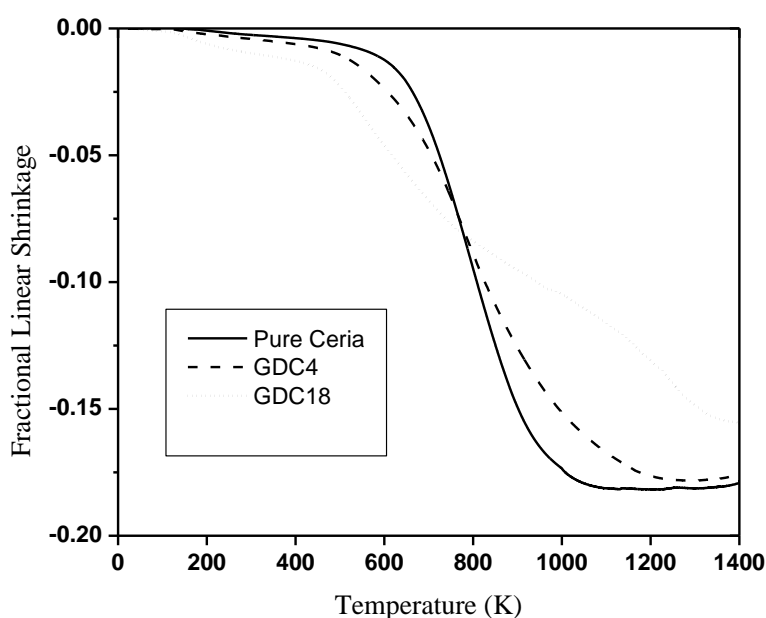
Fig. 3.6 Linear shrinkage as recorded from dilatometer experiments under constant rate (4 ^{o}C/min) of heating

3.4 Summary

GDC has been synthesized by gel combustion route using three different fuels namely, citric acid, glycine and urea. Citric acid and glycine form stable gels with mixed nitrate solutions of cerium and gadolinium and the combustion of the gel produces phase pure nanocrystalline powder without any residual reactant or carbonaceous matter. Urea is a weak complexing agent in mixed nitrate solutions of cerium and gadolinium and in turn it produces inhomogeneous precursor resulting in localized and incomplete combustion on heating. The combustion synthesized powder produced using urea fuel needs to be calcined at 700 ^{o}C. As the gadolinia content increases the combustion temperature increases because of the variation of heat of combustion. Phase pure and nano crystalline GDC powders with different level of gadolinia doping are successfully prepared through citrate nitrate gel combustion route using stoichiometric amount of fuel-to-oxidant. The powders produced using citric acid fuel could be sintered to near theoretical density at 1250 ^{o}C. Shrinkage sets in at a lower temperature as gadolinia dopant concentration increases. Because of higher reactivity of primary particle surface, the agglomerated particle size increases with increase in gadolinia content in gadolinia-ceria system. Due to the formation of hard agglomerates shrinkage occurs over wider temperature range and final sintering temperature is found to increase with increase in gadolinia content.

CHAPTER 4

Ionic conductivity of GDC electrolyte

4.1 Introduction

Solid oxides with fluorite structure, such as, ZrO_2 and CeO_2, when doped with aliovalent cations become oxygen ion conductor and are used as solid-oxide electrolyte in various electrochemical applications [118,159]. Rare earth oxides, such as, Gd_2O_3 and Sm_2O_3, are the most commonly used dopants in ceria. Their doping in ceria introduces vacancies in the oxygen sub-lattice as charge compensating defects. The defect reaction can be presented in Kröger-Vink notation:

$$Gd_2O_3 \xrightarrow{2CeO_2} 2Gd_{Ce}^{'} + 3O_O^{\times} + V_O^{\bullet\bullet} \quad \ldots\ldots\ldots\ldots\ldots.. (4.1)$$
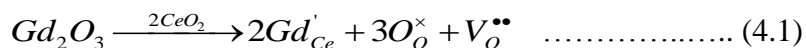
Oxygen ions hop through the vacancies and under a potential gradient a net flux of ions takes place resulting in ionic conductivity. The high oxygen ion conductivity has led to its use as an electrolyte material in solid oxide fuel cells. At higher temperatures and

reducing environment the valence state of cerium ions starts changing from Ce^{4+} to Ce^{3+}. This phenomenon introduces electronic conductivity in the material and restricts its use at higher temperature. Nevertheless, appreciable ionic conductivity and ionic transport number in doped ceria at temperatures lower than 800 ^{o}C make it a candidate electrolyte material for intermediate temperature solid oxide fuel cells (IT-SOFC) [160,43].

The diffusion of oxygen ions through the fluorite structure is a thermally activated process and is associated with an activation barrier. The oxygen ion conductivity increases with increase in temperature following Arrhenius equation. The temperature dependent ionic conductivity is expressed as:

$$\sigma = \sigma_0 \exp\left(\frac{-E}{kT}\right) \quad \text{.........................} \quad (4.2)$$

where, k is the Boltzmann's constant, E is the activation energy for ionic conduction and σ_o is the pre-exponential factor.

The pre-exponential term in Eq. (4.2) increases linearly with oxygen vacancy concentration. The concentration of oxygen vacancies increases with increase in dopant concentration. It may be apparent that the conductivity will increase with dopant concentration. However, for various fluorite based electrolyte systems it is known that conductivity increases with dopant concentration, exhibits a maximum and subsequently decreases with increasing dopant concentration. This is explained as due to the opposite effects associated with increase in the number of vacancies and decrease of vacancy mobility as the dopant concentration increases. At higher dopant concentration oxygen vacancies get associated with cations forming (Gd'$_{ce}$-$V_O^{\bullet\bullet}$- Gd'$_{ce}$) and (Gd'$_{ce}$-$V_O^{\bullet\bullet}$)^0

clusters. This association energy is a function of (a) coulombic interaction between the oxygen vacancy and the dopant cations and (b) the elastic strain field around the defect complex. The vacancies need to overcome these barriers to be mobile leading to oxygen ion conduction. Therefore, it is apparent that activation energy for ion migration increases with dopant concentration.

The ionic conductivity is also influenced by microstructure and impurities as reported by many authors for zirconia and ceria based electrolyte systems [161-166]. In zirconia based electrolyte systems it has been indicated that the grain boundary resistivity is two to three orders of magnitude higher than the bulk conductivity [161,162]. The grain-boundary resistivity originating from the space-charge layers has been discussed in detail by X. Guo [163]. With the logic of very high grain boundary resistivity as compared to the bulk resistivity, it is expected that large grained microstructure is preferable in order to achieve higher conductivity. In YSZ system Verkerk et al. [162] found that the grain boundary conductivity increases linearly with the grain size in small grained (0.3 to 2.4 μm) structure and is constant in large grained structure. On the contrary nanostructured YSZ fabricated by spark plasma sintering have significantly higher grain boundary conductivity in comparison with conventionally processed microcrystalline samples [164,165]. Presence of silica has been reported to affect the grain boundary conductivity significantly [165-168]. In samples having larger grains the total grain boundary area becomes less and there is a possibility that a significant part of grain boundary is covered by non-conducting impurity phase, such as, silica. Mondal et al. [168] has indicated that the specific grain boundary conductivity of the nanocrystalline samples is 1 to 2 orders of the magnitude higher than that of the microcrystalline samples. This has been attributed

to the low silica content and its grain size-dependent segregation in the nanocrystalline samples.

Contradictory results have also been reported in ceria based electrolyte systems. Zhou et al.[169] indicated that $Ce_{0.9}Gd_{0.1}O_{1.95}$ with finest grain size possessed highest grain boundary resistance. On the contrary, Christie and van Berkel [170] measured significantly low overall grain boundary resistance in $Ce_{0.8}Gd_{0.2}O_{1.90}$ samples with sub-micron mean grain size. Enhanced ionic conductivity in nanocrystalline solid electrolyte thin film has also been reported by many authors [171-174]. It has also been reported that decreasing grain size induces electronic conductivity [175]. This makes the generalization more difficult. As discussed by Belleno et al.[176], the electronic conductivity in nanocrystalline undoped or lightly doped ceria is attributed to the formation of space charge layer close to the grain boundary region. The width of the space charge region is inversely proportional to the root of the concentration of ionic defects. Thus, in heavily doped ceria the space charge region is very small and the space charge model is not much relevant [176].

In GDC system maximum conductivity has been reported for 12 mol% Gd_2O_3 content [118]. As mentioned above the conductivity is influenced by microstructure. From the above examples, it seems that the literature is not definitive on the issue of the effect of grain size on ionic conductivity. In order to address this issue, the present investigation is aimed at studying the effect of grain size on the bulk and grain boundary ion conduction behavior in gadolinia doped ceria. GDC containing 12 mol% Gd_2O_3 (12GDC) has been

chosen for this study. It has been reported that in heavily doped ceria samples when measurements are taken in oxidizing atmosphere (air, p_{O_2} = 0.2 atm.) the electronic contribution in the conductivity is not significant and ionic transport number can be considered close to unity [118]. For studying the effect of grain size on conductivity it is important to produce samples with high density and at the same time with different grain size. It has been discussed in the previous chapter that dense microstructure of gadolinia doped ceria can be obtained by low temperature sintering of doped ceria powder produced by gel combustion route. Grain size can be changed by post-firing the dense samples at higher temperatures. In the present investigation different microstructures of 12 mol% gadolinia doped ceria samples have been generated by adopting different firing schedule. The ionic conductivity has been determined from ac impedance data. Impedance spectra of the bulk and grain boundary have been analysed in order to discuss the influence of grain size on the ionic conductivity.

As discussed in Chapter 3, GDC nano-powders of different gadolinia content have been synthesized by solution synthesis routes and the powders have been sintered at 1250 $^{\circ}$C to get near theoretical density. This low temperature sintering of electrolyte material has added advantage in fabricating SOFC cell by co-firing route. As the conductivity dependents on composition and microstructure it is prudent to measure the conductivities of GDC samples of different compositions but prepared under a set of processing condition (starting powders and processing parameters, particularly, sintering parameters). The above investigation on optimization of composition has also been included in the present work.

4.2 Experimental

Gadolinia doped ceria powders with different level of gadolinia doping, synthesized by gel combustion method were used for this study. Pellets of 12 mm diameter were pressed in a uniaxial die and sintered at predetermined temperatures. Few pellets of 12GDC were sintered at 1200 ^{o}C for 3 h. Out of these pellets one set of pellets were further fired at 1400 ^{o}C and another set was fired at 1500 ^{o}C to generate microstructures of different grain sizes. 12 GDC samples sintered at 1200, 1400 and 1500 ^{o}C are referred as GDC12, GDC14 and GDC 15, respectively. Densities of the sintered pellets were determined by water displacement method. The micrographs of the sintered pellet were taken by SEM (Seron Technology, Korea). The SEM images were analyzed to estimate the average grain size by linear intercept method. GDC pellets of different compositions (nGDC, where n = 0, 3, 4, 6, 8, 10, 12, 15 and 18 mol% Gd_2O_3 doped in CeO_2) were also prepared by die pressing followed by sintering at 1250 ^{o}C. The densities of the sintered pellets were measured by water displacement methods and recorded.

Platinum paste was applied on both the flat sides of the sintered samples and baked at 1000 ^{o}C. Electrical measurements were carried out in a frequency response analyzer (Solatron 1260) in the frequency range 0.1 Hz to 10 MHz and in the temperature range 225 – 1000 ^{o}C in air. Resistance offered by different processes for oxygen ion conduction has been determined from complex impedance plots (Z'' vs. Z'). The ac electrical data have been analyzed using Z-view software to separate the contribution of bulk and grain boundary. Arrhenius plot for conductivity values were plotted and activation energies

were calculated for different samples. The impedance data are plotted in form of Bode

plots (plot of Z″ vs. log frequency) and oxygen ion jump frequency have been evaluated.

4.3 Results and Discussion

4.3.1 Densities and microstructures of the sintered 12GDC pellets

The densities of the 12GDC pellets obtained after sintering at 1200 ^{o}C were in the range

of 95 – 96% of theoretical density. The theoretical density of 12GDC has been taken as

7.22 g.cm^{-3} [177-178]. High value of sintered density is in agreement with high

sinterability of the combustion synthesized powder. On further firing at 1400 and 1500 ^{o}C

there was a marginal (less than 1.0%) increment in density. Thus in all the three samples

used in this study the densities remained in the range of 95 – 97% of theoretical density.

The SEM micrographs of the samples fired at 1200, 1400 and 1500 ^{o}C are shown in Fig.

4.1. Significant grain growth with increase in firing temperature is evident from the

micrographs. The dark/bright contrast in these microstructures is due to surface

topography. Energy dispersive X-ray spectra (EDS) do not show the presence of any

impurity element. The average grain sizes as estimated by linear intercept method are 0.2,

0.9 and 1.2 μm for the samples fired at 1200, 1400 and 1500 ^{o}C respectively.

4.3.2 Complex impedance plot: Determination of bulk, grain boundary and total conductivity

The ac impedance data have been plotted in the form of complex impedance curve (plot

of imaginary impedance vs. real impedance) and impedance spectra (plot of imaginary

10 μm

20 μm

20 μm
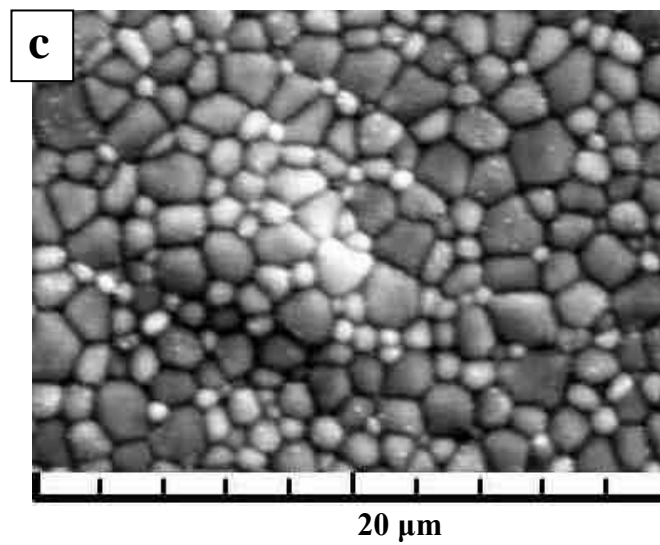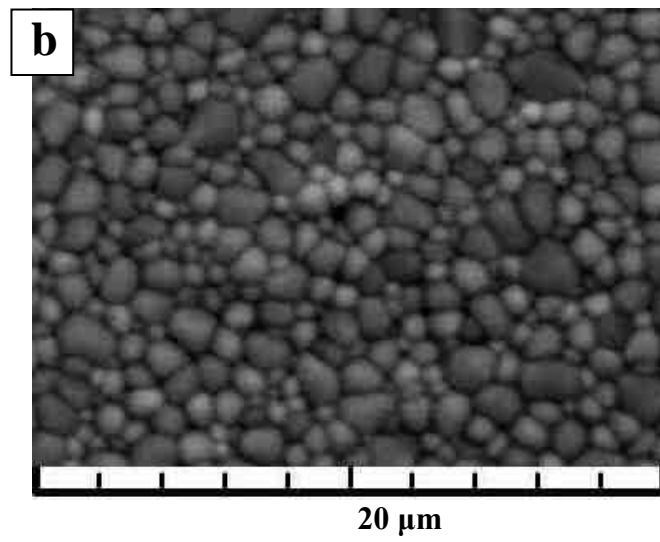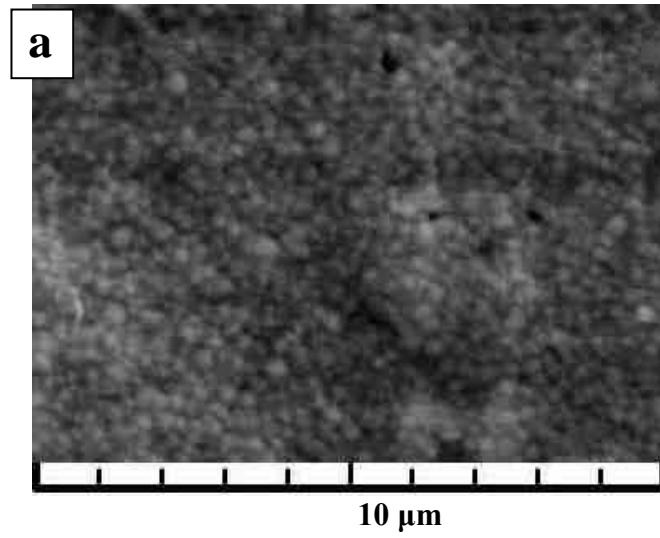
Fig. 4.1: SEM micrographs of the samples fired at (a) 1200, (b) 1400 and (c) 1500 ^{o}C

impedance vs. frequency) in order to analyze the ion conduction behavior of bulk and grain boundary in GDC samples. In general the relaxation time for the oxygen ion transfer through bulk, grain boundary and electrode are well separated and hence distinct arcs are expected for each process in the complex impedance plot [179]. In correlation with the relaxation times the arcs correspond to bulk, grain boundary and electrode properties are in order of decreasing frequency. Resistance of bulk or grain boundary is calculated from the difference between the low and high frequency intercepts of the corresponding arc (extrapolated on fitted semicircle using ZView software) with the real impedance axis. To calculate bulk and grain boundary conductivities, total thickness of all the grains and that of all the grain boundaries are required to be known separately. The grain boundary thickness is considered to be of few nm. Hence, the total thickness of grains can be approximately taken as that of the sample. However, the total thickness of grain boundary is difficult to estimate. Hence, apparent grain boundary conductivity has been used to compare the data. In this the total sample thickness is considered instead of only grain boundary thickness. It may be mentioned here that all the arcs are not necessarily to appear in the impedance plot depending on temperature and the experimental frequency range. As the temperature increases the relaxation time for a process decreases and the response shifts to higher frequency. Also at higher temperature as the sample impedance decreases the inductive component of the circuit dominates at high frequency. Because of the above two factors high frequency responses may not appear in the impedance plots made using experimental data.
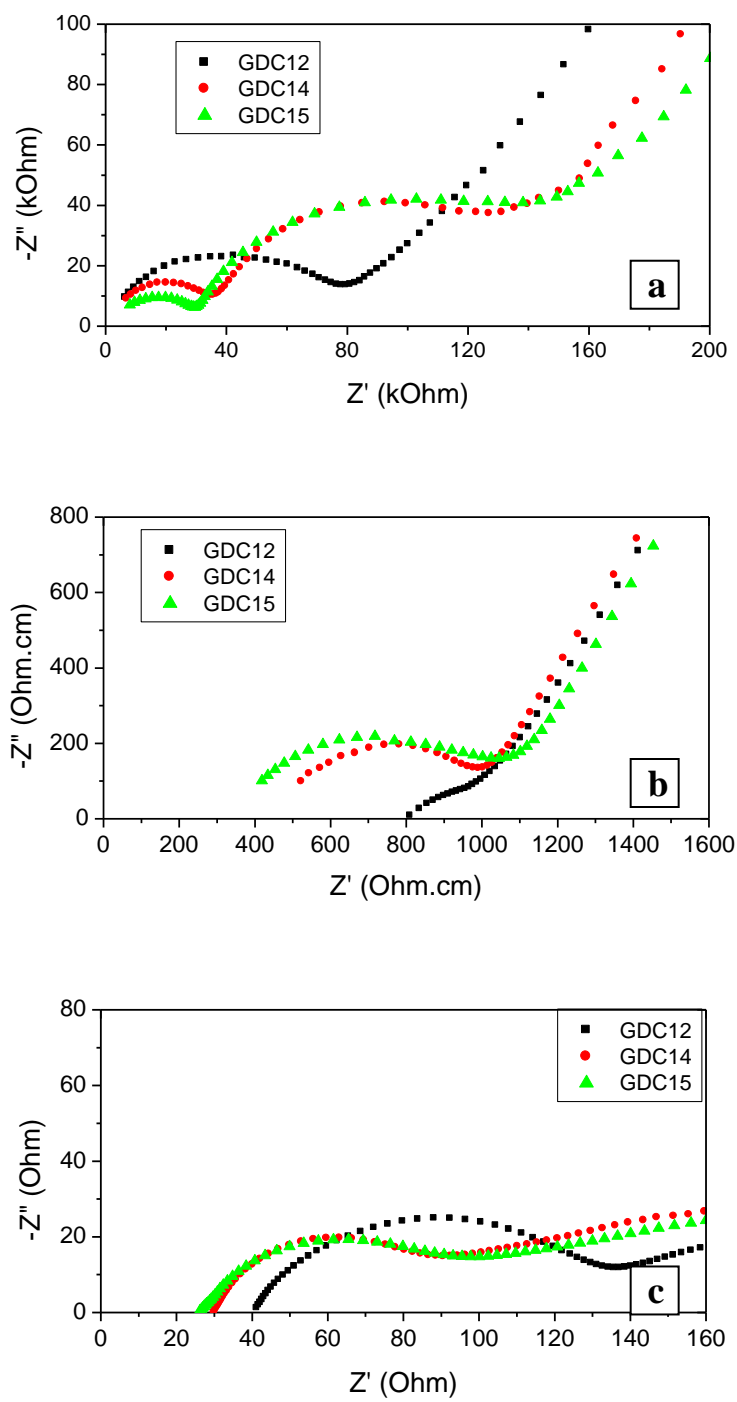
Fig. 4.2: Complex impedance plot of different samples (GDC12, GDC14 and GDC15) at (a) 300 ^{o}C, (b) 500 ^{o}C and (c) 1000 ^{o}C

The complex impedance plots of the three samples at temperatures 300, 500 and 1000 ^{o}C have been presented in Fig. 4.2(a-c). As shown in Fig. 4.2(a), the impedance plots at 300 ^{o}C, bulk and grain boundary arcs are distinct along with rising electrode arcs for GDC14 and GDC15 samples. In GDC12 sample, a broad curve appears instead of two distinct arcs for bulk and grain boundary. In this sample the low frequency intercept of the semicircle with the real impedance axis has been taken as the total resistance. Bulk resistances and grain boundary resistances have been determined separately for GDC14 and GDC15 samples. In the impedance plots at 500 ^{o}C (Fig. 4.2b) the responses from the bulk do not appear and hence, in this case only grain boundary resistances have been determined. Total resistances have been calculated from the low frequency intercept of the grain boundary arcs. At still higher temperature, both the responses from bulk and grain boundary are missed out as seen from the impedance plots at 1000 ^{o}C (Fig. 4.2c). In such cases, the high frequency intercept of electrode arc has been taken as the total resistance.

Fig. 4.3(a) and 4.3(b) show the variation of bulk and grain boundary conductivities with temperature in the form of Arrhenius plot for the samples GDC14 and GDC15. The bulk conductivity is found to be higher in GDC15 sample. The apparent grain boundary conductivities of GDC 14 and GDC15 are very close. The activation energy values for corresponding bulk and grain boundary are given in Table 4.1.
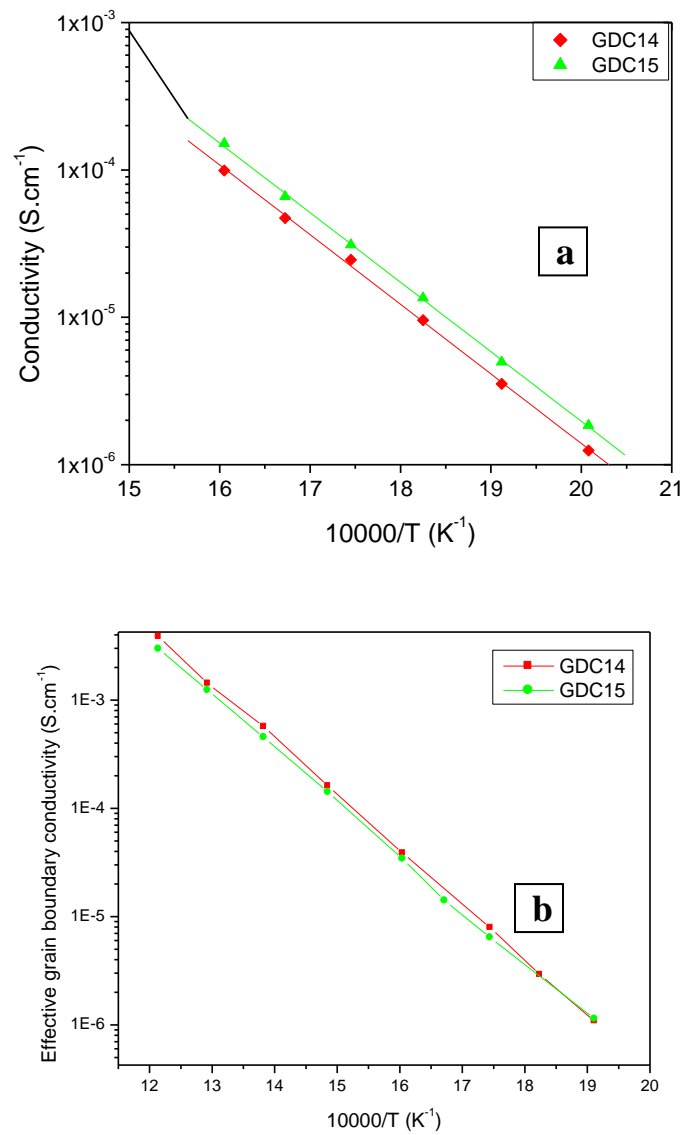
Fig. 4.3 Variation of (a) bulk conductivity and (b) effective grain boundary conductivity

with temperature presented in the form of Arrhenius plot

Table 4.1 Activation energies for the bulk and the grain boundary conduction

Sample	Activation energy (eV) for oxygen ion conduction	
	in bulk	in grain boundary
GDC14	0.94	1.01
GDC15	0.94	0.99
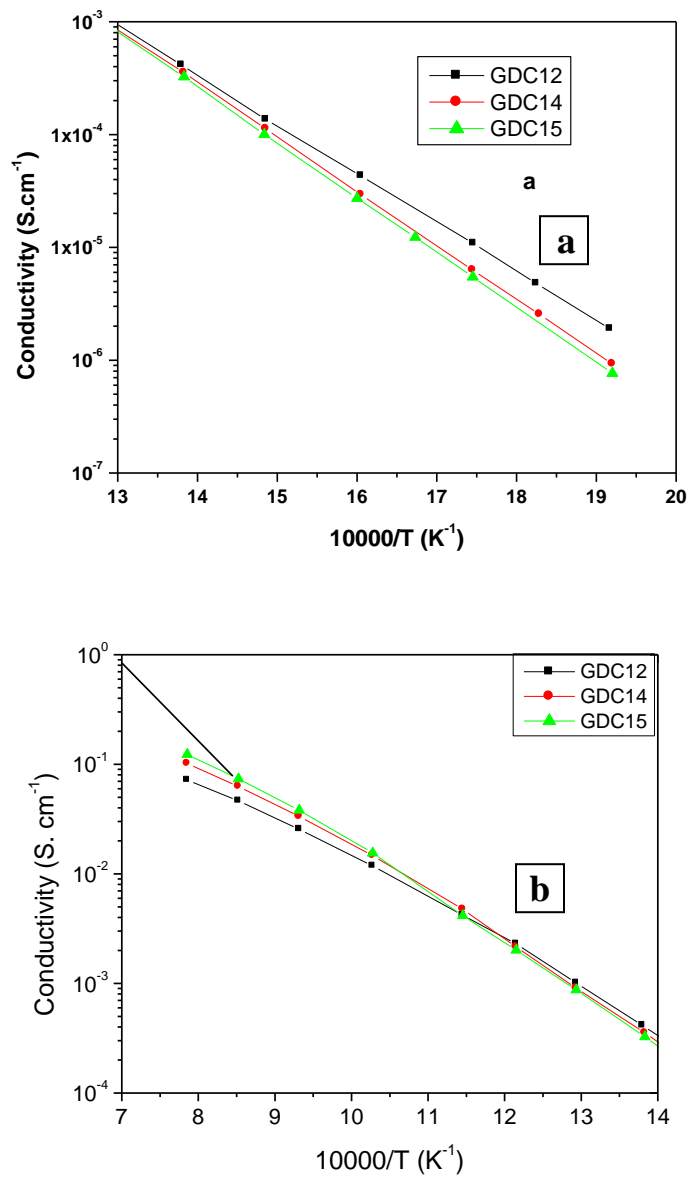
Fig. 4.4: Variation of total conductivity with temperature (a) in lower temperature range,

(b) in higher temperature range

Fig. 4.4 shows the variation of total conductivity with temperature in the form of Arrhenius plot. In the lower temperature range, as shown in Fig. 4.4(a), the total

conductivity increases with decrease in grain size. In the higher temperature range, as shown in Fig. 4.4(b), the total conductivity increases with increase in grain size. The total conductivity remains almost unaffected with firing temperature in the measurement temperature range 400 – 600 ^{o}C. It has been mentioned in the previous paragraph that the bulk conductivity of GDC15 is higher than that of GDC14. Thus the bulk effect is dominant in the higher temperature range. The reverse trend in the lower temperature range may be attributed to higher apparent grain boundary conductivity as the grain size decreases. As the grain size decreases the grain boundary path for ion conduction is believed to be more. Thus the actual grain boundary conductivity increases significantly with decrease in grain size.

4.3.3 Analysis of imaginary impedance spectra

The above observed phenomena can be better understood from the analysis of the imaginary impedance spectra. In the impedance spectra, the frequency corresponding to a peak of imaginary impedance (-Z") can be correlated to successful jump frequency of the oxygen ions [180]. This frequency is characteristics of composition and structural arrangement of atoms. Hence analysis of impedance spectra is expected to give information on oxygen ion hopping through the grain / grain boundary. As the relaxation frequency of bulk is more than that of grain boundary two distinct peaks corresponding to the bulk and grain boundary are expected to appear in the imaginary impedance spectra. It may be mentioned here that presence of impurity phases like silica can change the

77
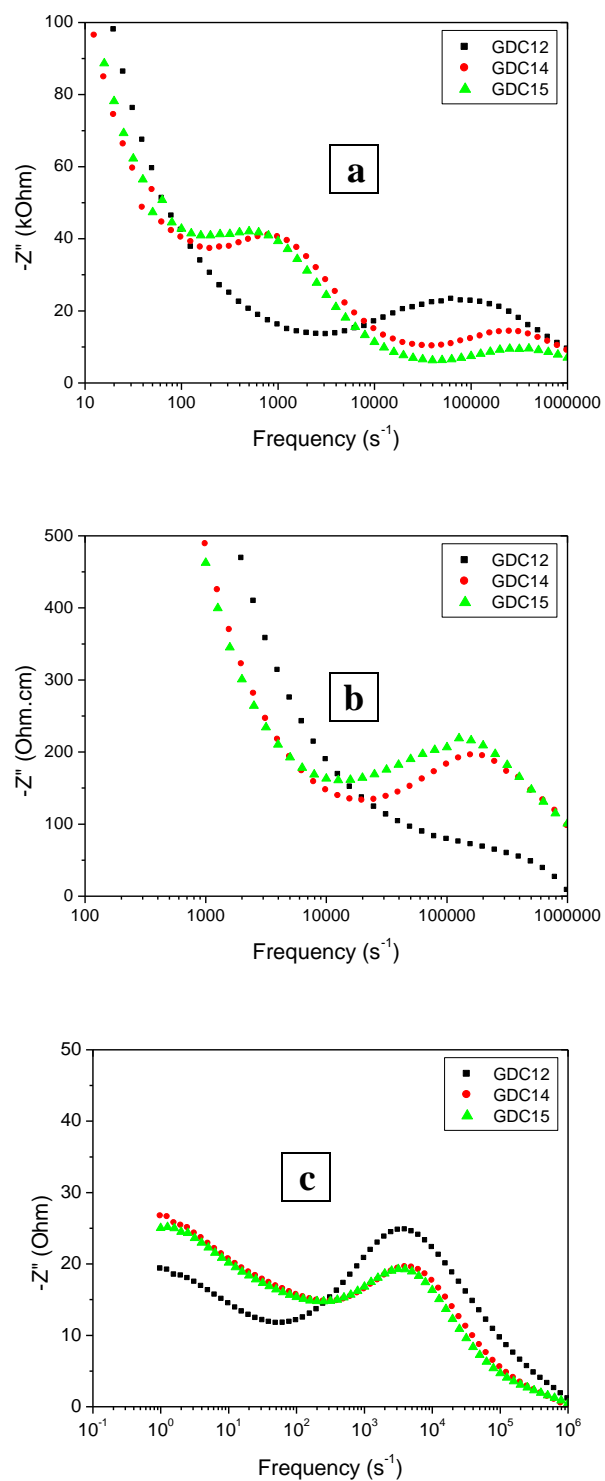
Fig. 4.5 Imaginary impedance spectra of different samples (GDC12, GDC14 and GDC15) at (a) 300 ^{o}C, (b) 500 ^{o}C and (c) 1000 ^{o}C

overall grain boundary resistance by reducing the effective conducting path across the grain boundary. Hence, analysis of measured conductivity data may not reflect true oxygen conduction behavior through the grain boundary. Thus, it will be interesting to analyze the characteristic frequency from the impedance spectra to avoid the complexity arising from partial coverage of grain boundary.

Fig. 4.5 shows the impedance spectra of the samples at 300, 500, and 1000 ^{o}C. The characteristic frequency is found to be influenced by the microstructure. The peaks can be distinguished for the samples GDC14 and GDC15. However, the peak is overlapped in case of GDC12. As shown in Fig. 4.5(a) the characteristics frequency corresponding to bulk in GDC14 is smaller than that of GDC 15 sample. However in the grain boundary the characteristic frequency is more in case of GDC14 sample. At an intermediate temperature, say at 500 ^{o}C as shown in Fig. 4.5(b), the bulk behavior does not appear. Observation of the grain boundary behavior shows that the characteristic frequency of GDC14 sample is more than that of GDC15 sample.

The variations of characteristic frequency with temperature for both bulk and grain boundary are shown in Fig. 4.6. In the overlapped peak of the GDC12 sample (Fig. 4.5(a)) the peak does not extend to the frequency corresponding to the grain boundary arc. Therefore, the grain boundary relaxation takes place at much higher frequency than that of other two samples fired at higher temperature. The peak frequency is in between the characteristic frequencies of bulk and grain boundary for GDC14 and GDC15 samples. This behavior indicates that the characteristics frequency of the bulk decreases and that of the grain boundary increases in GDC12 in comparison with GDC14 and

GDC15 samples. From the above analysis it can be said that characteristics frequency of the bulk decreases as the grain size decreases. Also the grain boundary characteristic frequency increases with decrease in grain size.
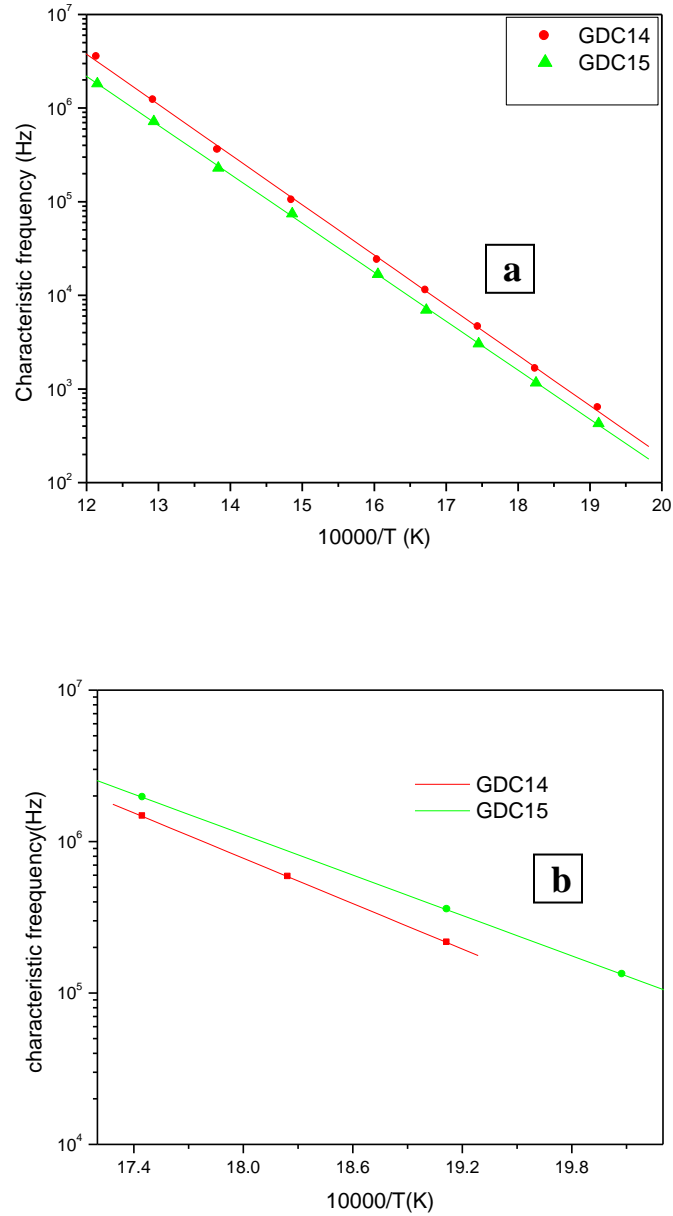
Fig. 4.6 Variation of hopping frequency with temperature (a) bulk and (b) grain boundary

Minute observation of Figure 11 of an article by Chen et. al. [164] reveals the trend of increase in grain boundary relaxation time (i.e. decrease in grain boundary characteristics frequency) with increasing sintering temperature in the range of 1200 to 1500 ^{o}C. The grain size was reported to increase with increase in sintering temperature as usually expected.

4.3.4 Grain size effect

The change in characteristic frequency can occur due to change in composition in the bulk / grain boundary by partitioning of solute at different firing temperatures. However the change in characteristic frequency is very significant in case of GDC12 sample having very fine grained structure. It is difficult to explain the significant shift of the grain boundary characteristic frequency by compositional changes due to partitioning of dopant. The shift towards higher frequency as the grain size decreases may be attributed to low angle grain boundary in nanostructured material. The change in the characteristic frequency of the bulk with grain size is also consistent. From the basic conductivity equation it can be seen that the characteristic frequency is related to the lattice vibration frequency. The results are indicative that the lattice vibration frequency is influenced by the grain size. Overall the bulk characteristic frequency decreases and grain boundary characteristic frequency increases with grain size in the fine grained structure.

4.3.5 Variation of conductivity with composition

Bulk and grain boundary ionic conductivities have been evaluated separately along with total conductivity for GDC samples of varying gadolinia content. Fig 4.7 shows the

variation of bulk ionic conductivity values (σ_g) of different compositions at various temperatures. At lower level of gadolinia concentration the bulk conductivity is found to increase sharply with gadolinia substitution. There is a plateau in the conductivity maxima at a doping level of 10 to 12 mol% gadolinia. On further gadolinia doping a regular decrease in the conductivity value is observed.
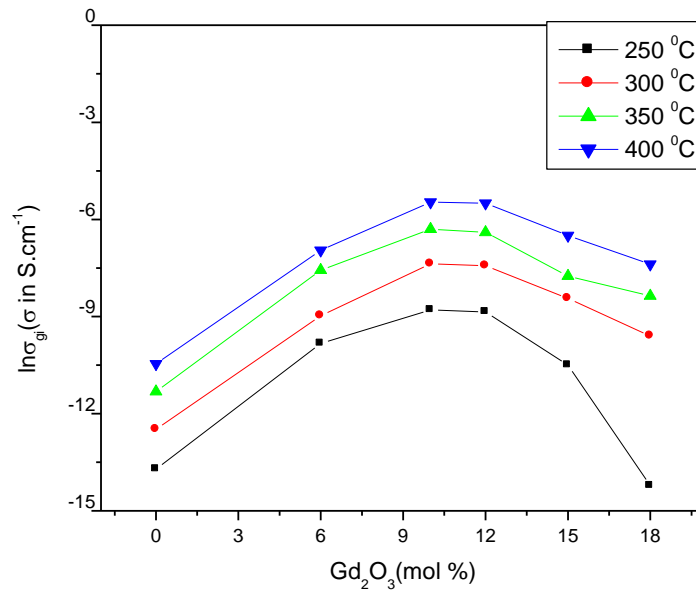
Fig 4.7: Variation of lattice conductivity with composition at different temperatures

Similar to the previous section in the analysis of grain boundary conductivity, 'apparent grain boundary' or 'effective grain boundary conductivity' has been used to present the data. While calculating the apparent grain boundary conductivity, the total thickness of the sample is taken into consideration. Fig. 4.8 shows the variation of grain boundary conductivity with composition. A very high grain boundary resistance is observed in the dilute region. For pure CeO_2 the apparent grain boundary resistance value is 1000 times
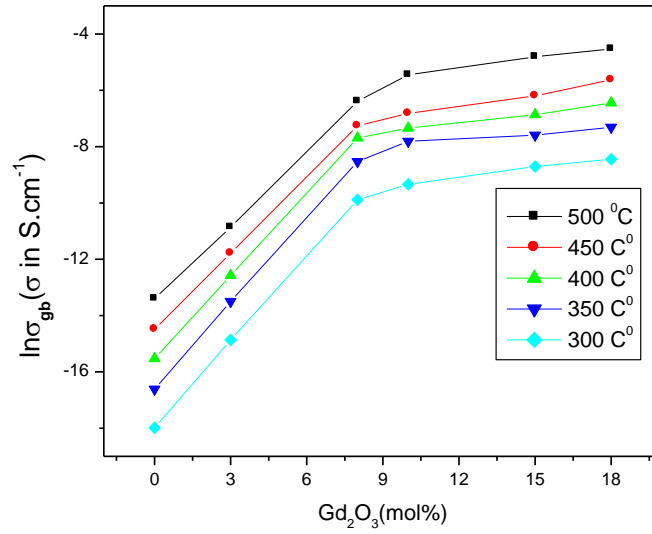
Fig. 4.8: Variation of grain boundary conductivity with composition at different temperatures

higher compared to 3GDC. It has been reported that the thickness of the grain boundary and effective grain boundary area decreases with gadolinia substitution [183]. Hence, the resistance contribution from the grain boundary decreases with gadolinia doping. There is a sharp increase in the grain boundary conductivity up to 6GDC and then the increase in conductivity is not significant. A plateau in the grain boundary conductivity was observed above 15GDC.

The variation total conductivity with composition is given in Fig. 4.9. There is a smooth increase in conductivity value with increase in gadolinia content. In the dilute region the conductivity was controlled by the grain boundary conductivity. The ratio of grain boundary resistance to the total resistance decreases from 95% to 58% as gadolinium content varies from 0 to 6 mol%. It has been observed that highest conductivity is

obtained in the composition range of 10GDC to 12GDC. However at higher gadolinia concentration, defect association leads to lowering of the effective concentration of oxygen vacancies. At higher doping level the bulk conductivity dominates. Hence, increase in gadolinia content leads to decrease in the overall conductivity.
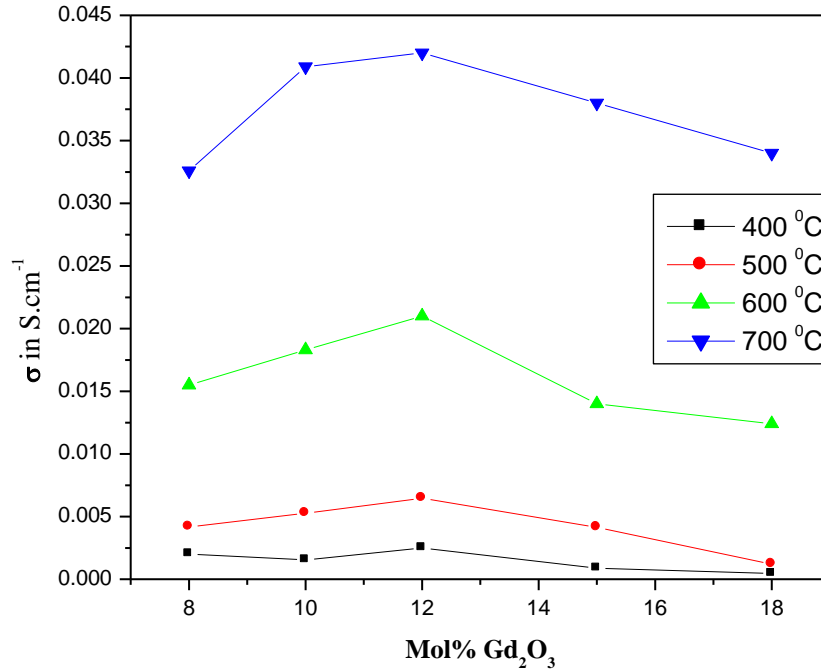
Fig. 4.9 Variation of total conductivity with composition

4.3.6   Activation energies for ionic conduction

The conductivity values at different temperature are represented by Arrhenius plots. Arrhenius equation for conductivity is expressed as follows,

$$\sigma = \sigma_0 \exp\left(\frac{-E}{kT}\right) \qquad \dots (4.2)$$

Taking natural logarithm of both sides, the equations (4.2) become:

$$\ln(\sigma) = \ln(\sigma_0) - \frac{E}{kT} \qquad \dots (4.3)$$

Graph of ln(σ) vs 1/T is plotted to calculate the value of activation energy. The variation of activation energy for bulk and grain boundary conduction with varying composition of gadolinia doping is shown in Fig. 4.10. It has been observed that for bulk conduction, there is no appreciable change in the activation energy up to 5mol% Gd_2O_3 doping. On further doping of Gd_2O_3 the activation energy increases. This increase in activation energy is attributed to the association of the oxygen vacancy with the dopant metal cations. The activation energy for grain boundary conduction in the dilute region is very high. This higher activation energy is attributed to very high grain boundary thickness [183]. There is a rapid decrease in the activation energy for grain boundary conduction and a minimum is observed in the range 10GDC to 15GDC. Increase in activation energy is observed on further increase of gadolinia content. From the work of Avila-Paredes et al.[183] it has been seen that with gadolinia doping the thickness of the grain boundary decreases and hence the activation energy decreases. At still higher doping level there is increase in activation energy due to increased space charge layer thickness [183].

The Arrhenius plot for total conductivity is not linear over the entire temperature range. At intermediate temperature region the activation energy has two parts namely association enthalpy and migration enthalpy. At higher temperature region dissociation of vacancies takes place. The activation energy at high temperature known as migration enthalpy is not varies much with composition, whereas the association enthalpy varies

with composition. The curve of activation energy with composition is shown in Fig. 4.11.

This shows a minimum at around 10-12 mol% doping.
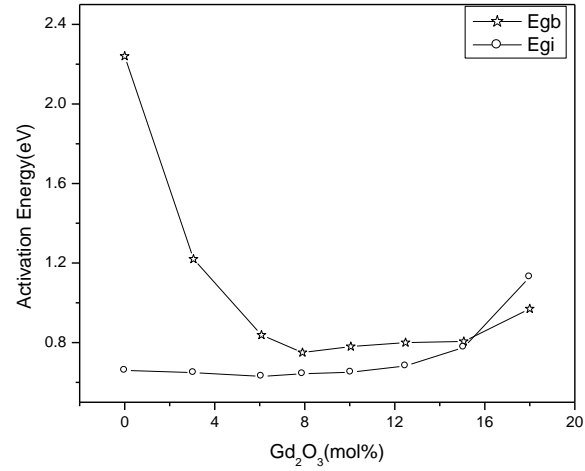
Fig. 4.10 Variation of activation energy of grain and grain boundary with composition
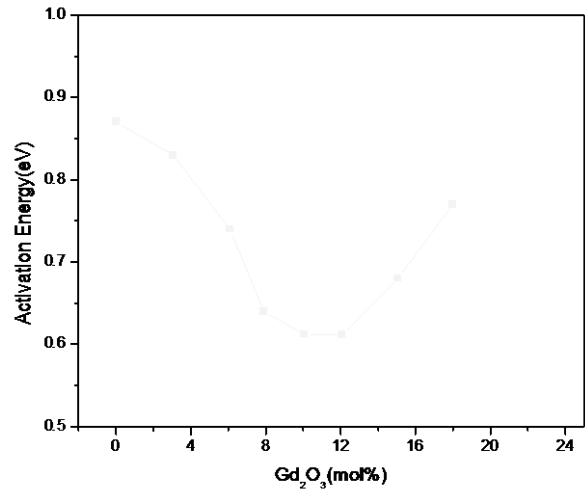
Fig. 4.11 Variation of activation energy with composition

4.4 Summary

Gadolinia substituted ceria with dense and fine grained microstructure can be prepared by low temperature sintering of combustion synthesized powder. The grain boundary conductivity increases and bulk conductivity decreases as grain size becomes finer. As a consequence, at lower temperature maximum conductivity is obtained with fine grained structure and at higher temperature conductivity is more with coarse grained structure. Thus from technological point of view fine grained microstructure is preferable for application at lower temperatures. The analysis of impedance spectra reveals that the relaxation frequency is influenced by the grain size. The relaxation frequency of the bulk decreases and that of grain boundary increases with grain size in the fine grained structure. Gadolinia doping in cerium oxide produces oxygen vacancies responsible for the ionic conductivity. With increase in gadolinia doping conductivity increases and reaches a maximum value at 10 to 12 mol% doping. On further substitution of gadolinia, conductivity decreases. Lattice/ grain interior conductivity follows the same pattern as total conductivity. However, grain boundary conductivity decreases rapidly with gadolinia doping and remains almost same for 6GDC to 15GDC. The activation energy for total conduction have a minimum for 10-12GDC. Activation energy for lattice conductivity remains same up to 6GDC and increases on further substitution. Activation energy for grain boundary conductivity decreases rapidly and attains a minimum at 10GDC.

CHAPTER 5

Synthesis and characterization of

NiO- GDC composite for SOFC anode

5.1 Introduction

The performance of a SOFC depends on the internal resistance of a cell during operation. The internal resistance mainly depends on the electrolyte resistance and the polarisation resistance at the electrode-electrolyte interface. In an electrode supported cell thin electrolyte can be integrated to minimize the resistance coming from electrolyte. The electrolyte resistance depends on the material and thickness of the electrolyte layer. For dense GDC electrolyte of nominal thickness of about 20 μm the area specific resistance is about 0.1 $\Omega.cm^2$. Anode supported cell having thin electrolyte has been reported extensively in the literature [184-192]. Nickel has good catalytic property towards hydrogen oxidation and is widely used in the anode structure in the form of a composite of nickel and the electrolyte material. Nickel has higher coefficient of thermal expansion compared to GDC electrolyte. However, in the nickel–GDC composite the thermal

expansion coefficient matches quite well with the electrolyte material. Also, presence of electrolyte material in the anode structure extends the triple phase boundary area. Therefore, Ni-GDC composite is a potential anode material for GDC electrolyte based IT-SOFC [193-194].

Apart from the electrode composition the microstructure plays an important role. The electrochemical reaction at the anode is heterogeneous in nature. The heterogeneous reactions at the anode takes place at the triple phase boundary (TBP) area where the pores, the Ni phase and the YSZ electrolyte meet. Hence the triple phase boundary should be as large as possible for better catalytic activity. At the same time the continuity of nickel phase need to be maintained throughout the anode structure in order to keep TBPs active through better current collection. Fine microstructure is expected to have better TBP area. Also fine NiO particle ensures electrical percolation in the sintered anode structure. Therefore it is required to have ultrafine NiO powder with narrow size distribution for effective control over latter stage processing and sintering properties i.e control over final microstructure and performance of the fuel cell. Increase in the Ni amount increases the conductivity, however themal expansion coefficient (TEC) also changes drastically. Conductivity value decrease with decrease in nickel content and there exist a threshold value below which the conductivity falls drastically. NiO was taken as precursor for the Ni-GDC anode fabrication. At the high operating temperature and reducing atmosphere of the anode NiO transforms into Ni. NiO-electrolyte composite close to 1:1 weight ratio has been used by many authors [195,196]. After reduction of NiO in the anode, there should be continuity among the nickel particle for better current collection. The minimum amount of nickel to GDC ratio for which there will be a

continuous network among Ni particles is called percolation ratio which is around 30 weight %.

GDC powder for preparation of anode structure has been described in Chapter 3. Fine NiO powders can be prepared by various wet chemical methods [197-200]. Gel combustion method is an attractive method for preparing fine powders without calcination. Optimization of fuel to oxidant leads to final product in a single step in many occasions. In the present investigation ultra fine NiO has been synthesized by combustion route and physical characterization of the powder was carried by x-ray diffraction, laser scattering, scanning electron microscope, transmission electron microscope, and EDS. Electrical conductivity of NiO-GDC has been measured in H_2 atmosphere.

5.2 Experimental

5.2.1 Synthesis of fine NiO powder

Fine NiO has been synthesized by solution combustion route using nickel nitrate as oxidant and citric acid as fuel. Calculated amount of $Ni(NO_3)_2.6H_2O$ was dissolved in deionised water. Required amount of citric acid as calculated from propellant chemistry was added to the metal nitrate solution with constant stirring on a hot plate. After dehydration, a viscous gel is formed and further heating of the gel leads to an exothermic reaction with evolution of large amount of gaseous molecules. The flowchart for the preparation of fine NiO powder through combustion route is shown in Figure 5.1. The

decomposition behaviour of the dried precursor gel from combustion synthesis was carried out on a TG-DSC instrument (SETARAM: SETSYS evolution) in flowing air atmosphere. X-ray diffraction of the as synthesized powder was taken in an X-Ray diffractometer (Philips, model: PW1830) in the 2θ range from $20 - 80^o$ with a step size of 0.02^o. The as-synthesized powder was calcined at 700 ^{o}C and X-ray diffraction pattern of the calcined powder was recorded. The particle size of the calcined powder was taken in a laser diffraction particle size analyzer (HORIBA, Model: LA500). The morphology of the calcined powder was observed using a scanning electron microscope (Model: SERON 2000, South Korea) and a transmission electron microscope (TEM).
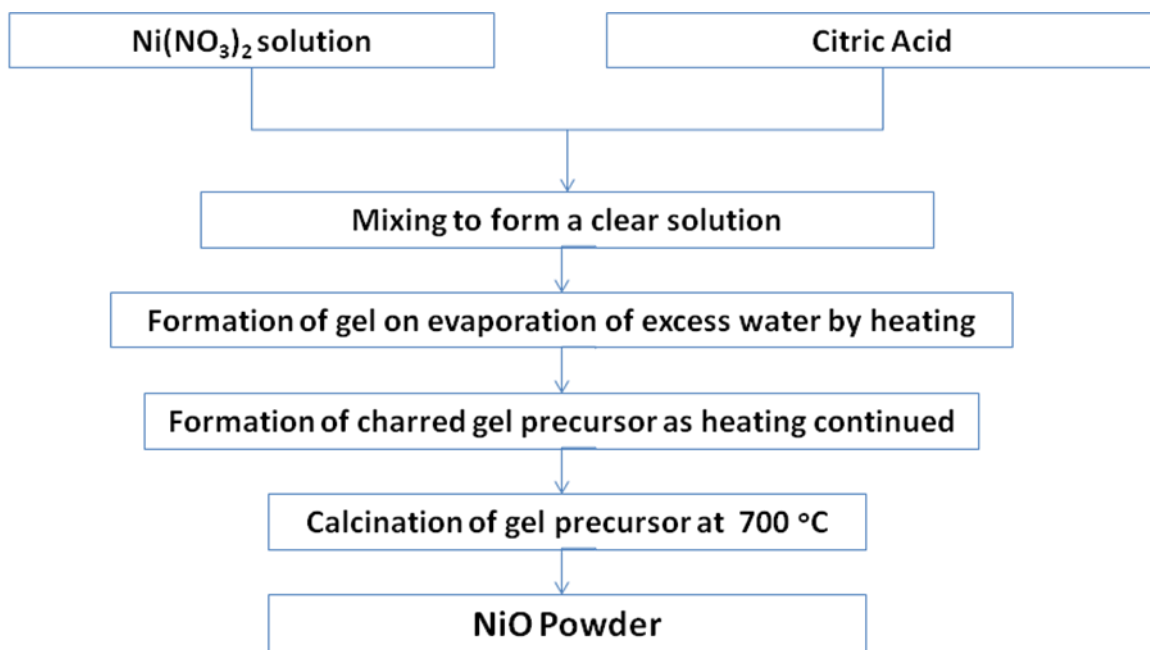
Fig. 5.1: Flowchart for the preparation of fine NiO powder through combustion route

5.2.2 Preparation of NiO-GDC powder

NiO and GDC powders were taken in weight ratio 1:1 and mixed in a ball mill in ethanol medium for 6 h. After mixing, the powder was dried under IR lamp. Pellets of 12 mm in diameter were prepared by uniaxial die compaction at a pressure of 180 MPa. The green pellets were sintered at 1350 ^{o}C and the densities of the sintered pellets were measured by water displacement method. The micrographs of the sintered pellets were taken in a scanning electron microscope (Model: SERON 2000). Distribution of the NiO and GDC phases in the sintered pellet was confirmed by energy dispersive X-ray spectroscopy (EDS) (Oxford make). Rectangular bar pellets of ~20 mm length and 6×6 mm^2 cross sectional area were prepared by cold compaction in a rectangular die pressing at a pressure of 180 MPa. The bar pellet was sintered at 1350 ^{o}C and treated in hydrogen atmosphere to facilitate reduction of NiO into metallic Ni. Electrical conductivity measurement of Ni-GDC bar specimen was carried out by dc four probe technique in hydrogen environment using a source meter. Microstructure of the reduced pellet was carried out by a SEM.

5.3 Results and Discussion

5.3.1 Synthesis and characterisation of fine NiO powder

In the synthesis of NiO powder, nickel nitrate and citric acid were taken in molar ratio 9:5 as per propellant chemistry. Nickel nitrate acts as an oxidiser and citric acid acts as

fuel to enable combustion reaction. TG-DSC graph of the dried gel-precursor in the combustion route is shown in Fig. 5.2. The initial mass loss in the range 80-200 ^{o}C is attributed to the loss of water molecules left in the gel. There was a sudden mass loss at 370 ^{o}C and an exothermic peak corresponding to the mass loss is an indicative of combustion reaction. After the combustion there is gain in mass as reflected in the TG pattern. The as-synthesized powder in the solution combustion route using citric acid as fuel was calcined at different temperatures. A minimum calcination temperature of 700 ^{o}C is required for phase formation as indicated in the X-ray diffraction pattern. The X-ray diffraction patterns of the as-synthesized powder and calcined powder are shown in Fig. 5.3. Peaks corresponding to NiO and metallic Ni phases are present in the XRD pattern of as-synthesized powder. This is attributed to the reducing environment prevailing in the combustion reactor. Initial Ni content in the as synthesized powder is converted to NiO leading to a mass gain in the TG-DSC graph. It may be noted that for taking right quantity of NiO powder to get NiO-GDC mix powder it is required to have single NiO phase in the powder. From the XRD pattern of the calcined powder it is observed that only NiO peaks are present. Therefore, calcination at 700 ^{o}C fully oxidises Ni particles that were present in the as-synthesized powder. Particle size distribution of calcined powder was measured by laser diffraction particle size analyzer and the median particle size is found to be 0.69 micron. From XRD line broadening the crystallite size has been calculated to be 7 nm. These results suggest that the calcined powder is agglomerates of nm size crystallites.
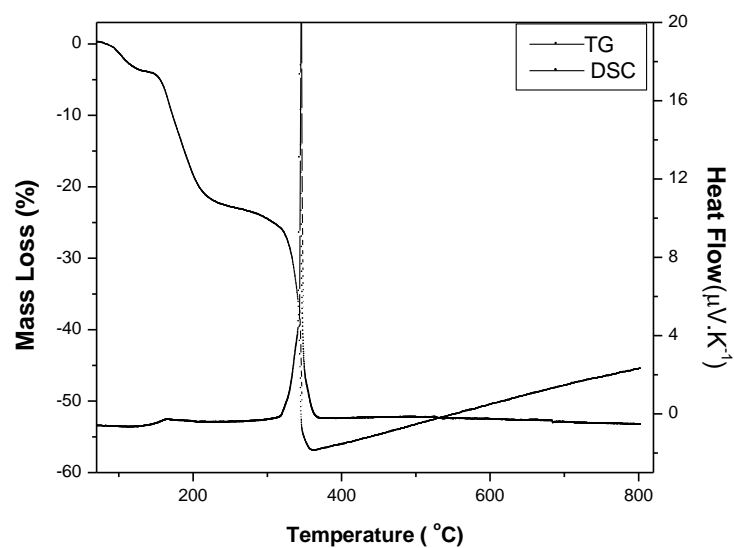
Fig. 5.2: TG-DSC pattern of gel precursor of NiO in the combustion method
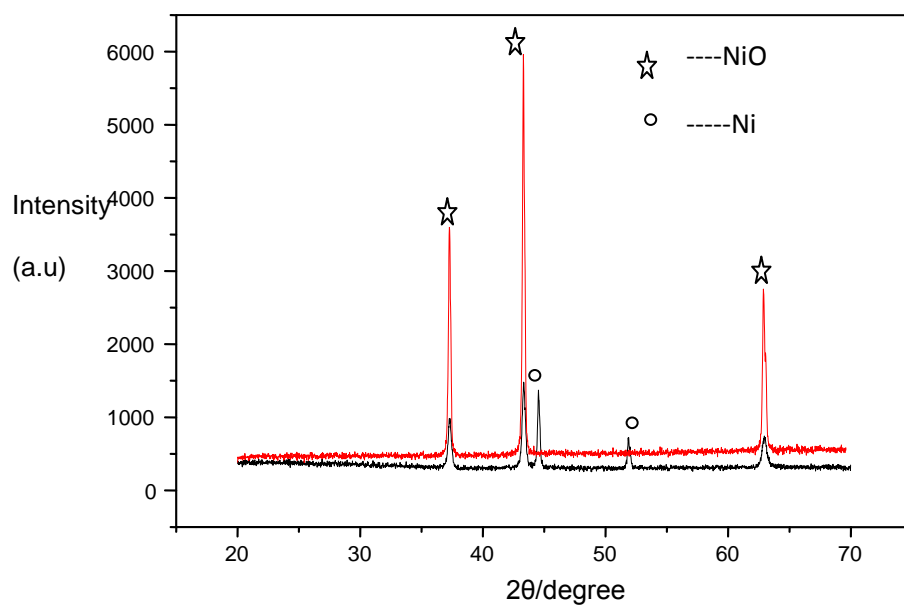
Fig. 5.3: X-ray diffraction pattern of as-synthesized (black line) and calcined (red line)
NiO powder
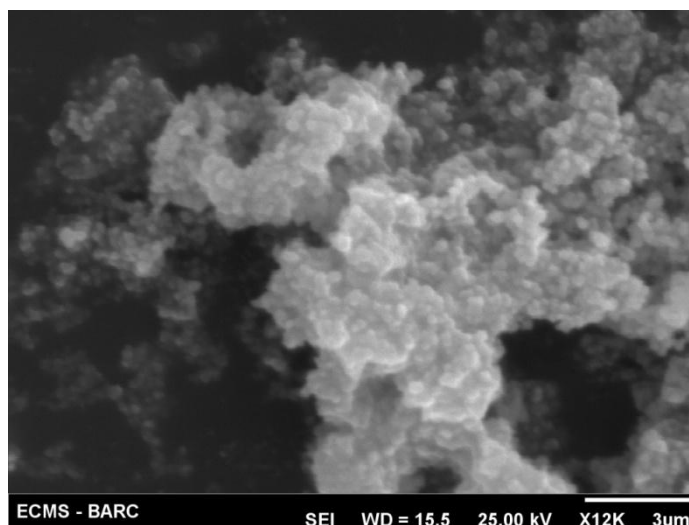
Fig.5.4: SEM micrograph of the calcined NiO powder
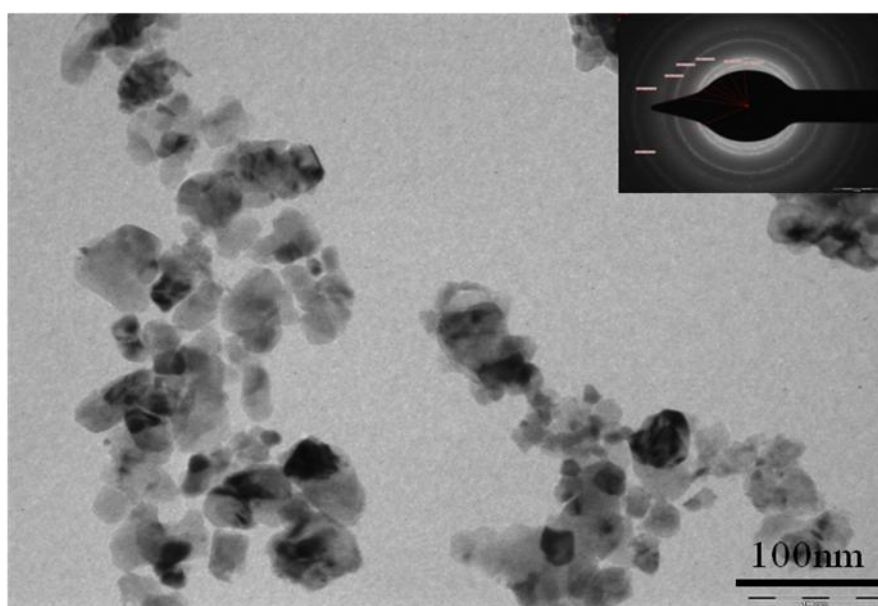
Fig. 5.5: TEM image of calcined NiO powder showing nm size primary particles

The insert show SAED pattern

The SEM micrograph of the calcined powder is shown in Fig.5.4. Submicron size agglomerates are observed in the SEM micrograph. The size of the agglomerate

corroborates the results obtained from laser diffraction particle size analyser. Though submicron size particles are observed in the SEM micrographs, finer details are not clear. Nano size primary particles are clearly observed in the TEM micrographs as shown in Fig. 5.5. The average size of the primary particles in the calcined powder is about 15 nm. These nano size particles are bound by weak van-der-waals force forming agglomerates that can break easily during compaction of powder.

5.3.2 Characterisation of NiO-GDC sintered pellet

Fig. 5.6 shows the scanning electron micrograph of the sintered NiO-GDC pellet. Two different phases are distinctly identified in the micrograph. One phase has networked structure of larger grains of size in the range of 1 to 2 μm. The grain size of other phase is relatively finer (<1 μm). The finer grains also form a networked structure. At some places the finer grains are present in agglomerated form. Pores are present in the microstructure and the porosity is 15% as measured by water displacement method. The porosity is expected to increase in the Ni-GDC cermet structure after reduction. In order to identify the phases in the composite structure EDS analysis has been carried out. It is observed from the micrograph that the GDC electrolyte particles have grown up to micron size though fine nano size particles are used as initial material. The EDS element scan of the NiO-GDC surface and the corresponding secondary electron micrograph is shown in Fig. 5.7. The element scans indicate that larger grains correspond to GDC phases and smaller grains are of NiO phase.
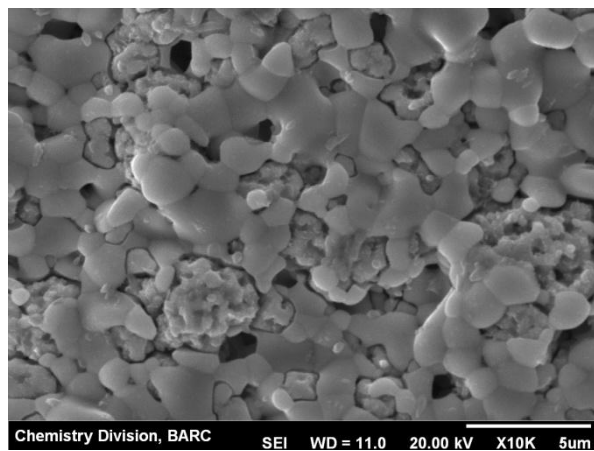
Fig. 5.6: SEM micrograph of NiO-GDC pellet sintered at 1250 ^{o}C
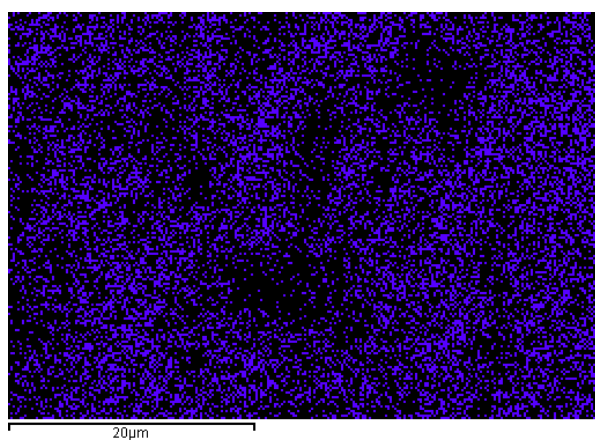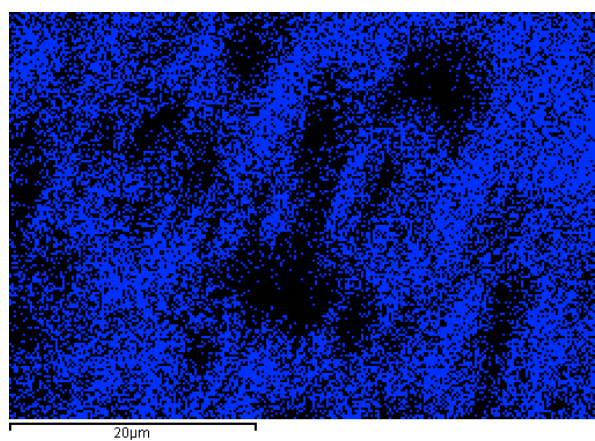
Gd Mapping

Ce Mapping
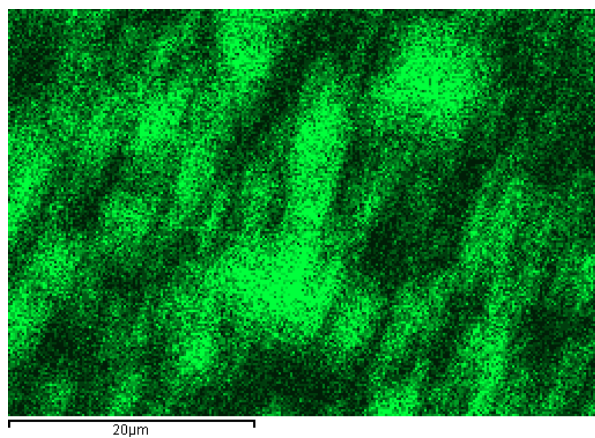
Ni Mapping
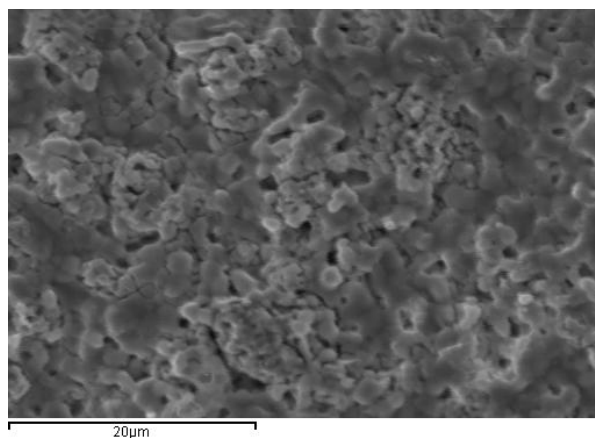
SE image

Fig. 5.7: EDS element scan of the NiO-GDC surface and the corresponding SE image

5.3.3 Characterisation of Ni-GDC cermets

The electrical conductivity of the Ni-GDC bar specimen measured by four probe DC technique is shown in Fig.5.8. Metallic behaviour is observed in the conductivity plot, where conductivity decreases with increasing temperature. The electronic conductivity of GDC is very low compared to Ni in the cermet composition. Hence total conductivity is controlled by the conductivity of networked nickel phase in the anode. At temperatures below 400 ^{o}C conductivity value more than 1500 S.cm^{-1} has been obtained. The conductivity remains around 1200 S.cm^{-1} even at 800 ^{o}C which is the upper temperature limit of IT-SOFC operation. Ni coarsening has been addressed in the literature when Ni cermet is used for prolonged time. This leads to decrease in conductivity of the anode as well as reduces the triple phase boundary area. In the present study the conductivity has been measured at 800 ^{o}C for 72 h continuously. No appreciable decrease in the conductivity has been observed. Low temperature operation as well as uniform distribution of GDC phases prevents coarsening of nickel particles. The SEM micrograph of a sintered and reduced NiO-GDC pellet is shown in Fig. 5.9. More than 30% porosity was observed in the reduced pellet as confirmed from the water displacement data.
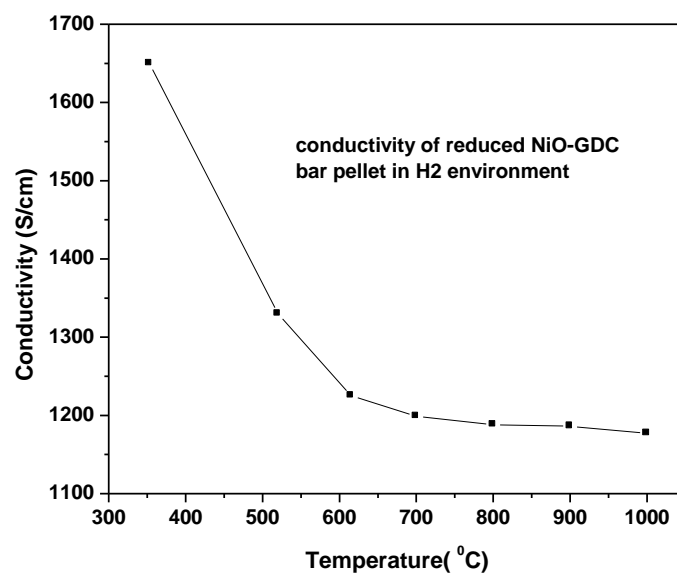
Fig: 5.8 Variation of conductivity with temperature of a reduced NiO-GDC bar pellet
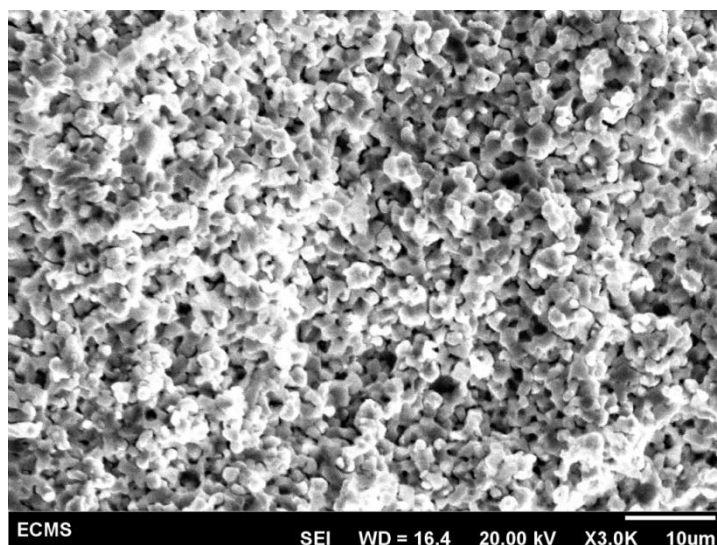
Fig: 5.9 SEM micrograph of the reduced Ni-GDC pellet

5.4 Summary

Phase pure nano-size NiO powder has been prepared by gel combustion and subsequent calcination at 700 ^{o}C. NiO-GDC anode prepared by mixing combustion synthesized GDC and NiO powders followed by sintering at 1250 ^{o}C shows networked structure of both GDC and NiO phases. The electrical conductivity of Ni-GDC cermet is well above 1200 S.cm^{-1} and the electrical conductivity is found to be stable over long time. The results suggest that Ni-GDC cermet prepared using nano-sized starting powder can form an anode structure having long term stability.

CHAPTER 6

Synthesis and Characterization GdCoO₃ based Cathode Material

6.1   Introduction

Solid Oxide Fuel Cell (SOFC) is an energy conversion device which can produce electricity by electrochemical reaction between a fuel (e.g. hydrogen, natural gas) and oxygen in an efficient and environment friendly manner[160,43]. SOFCs are required to be operated at high temperatures (in the temperature range of 800 -1000 ^{o}C) and therefore, one of the technological hurdles in SOFC technology is in getting compatible materials with long term durability. Lowering the operating temperature suppresses degradation of cell components and thereby increases the durability of the cell and widens the choice of materials in stack design. However, operation of SOFC at lower temperature implies lower electrode kinetics, resulting in large interfacial polarization resistance and lower electrolyte conductivity. In order to maintain high efficiency of SOFC in the intermediate temperature range (600-800°C) there is a need to develop new materials and improved cell fabrication techniques.

Gadolinia doped ceria is reported to have appreciable ionic conductivity and ionic transport number to make it a candidate electrolyte material for intermediate temperature SOFC (IT-SOFC) [43,118,160,201]. This electrolyte material needs to be integrated with suitable electrode materials having good electro-catalytic activities in the operating temperature range. The electrode material must have high electronic conductivity and thermal expansion coefficient matching with the electrolyte material. Further, the electrode material must have chemical compatibility with electrolyte material in the conditions prevailing during fabrication and operation.

Perovskite materials with general formula ABO_3 (A = La and other rare earth metals, Ca, Sr, Ba etc.; B = Mn, Fe, Co, Ni etc.) are widely used as cathode materials in SOFCs [202-205]. In general, doped cobaltites are reported to have better electro-catalytic activities for oxygen reduction reaction as well as higher electronic conductivities than other electrode materials [204-207]. However, thermal expansion coefficient values of many cobaltites are significantly higher than that of GDC electrolyte material. Large mismatch in thermal expansion coefficient with the electrolyte material may result in delamination at the electrode-electrolyte interface or cracking of the electrolyte layer [208]. Among the different rare earths that form lanthanide cobaltite perovskites the thermal expansion coefficients of the cobaltites decrease in the order of La, Pr, Nd, Sm and Gd [205]. Thus $GdCoO_3$ can be a potential electrode material. Thermal expansion coefficient of cobaltites is also influenced by substituting 'A' sites or Co sites with suitable elements. Substitution of La sites in $LaCoO_3$ with aliovalent dopants, such as Sr, is reported to increase oxygen vacancy in the cobaltite structure. This results in increase in ionic

conductivity and also increase in thermal expansion coefficient. The increase in ionic conductivity can have a beneficial effect by way of enhancement of the triple phase boundary area. As the reaction at the cathode is heterogeneous in nature, larger triple phase boundary (TPB) area will lead to better reaction kinetics and consequently decrease in area specific resistance (ASR) at the interface. The high thermal expansion coefficient is often brought down close to the thermal expansion coefficient of the electrolyte material by doping Co sites with Fe, Mn etc. [204-205]. However, electro-catalytic activity is likely to be reduced by doping the Co sites. Therefore, among the lanthanide cobaltites, gadolinium cobaltate has been taken in the present study. Sr doping has been studied and reported by many authors. Ba has larger ionic radius and is expected to reduce the thermal expansion coefficient. It is expected that there will be decrease in is the TEC value and increase in the ionic conductivity with barium substitution. The TEC of cathode material can also be tuned close to that of the electrolyte material by the composite electrode approach [204,209-211]. This use of $GdCoO_3$ in association with GDC electrolyte is expected to have beneficial effect in decreasing the thermal expansion coefficient and extending the triple phase boundary area. The triple phase boundary area can be increased by using fine particles of electrode material and tailoring the microstructure [212-213]. Therefore ultrafine powders of Ba doped Gd cobaltite has been synthesized by wet chemical route and composite electrode approach has been adopted in the present study.

There are various solution synthesis routes (e.g. co-precipitation, hydrothermal, sol–gel, solution polymerization, solution combustion etc.) that have been used to prepare fine

mixed oxide powders in narrow particle size distribution. Solution polymerization is one of these routes that uses less expensive starting materials and produces phase pure oxide ceramic powders [214]. In the present study, $GdCoO_3$ and barium substituted (10 and 15 mol %) $GdCoO_3$ powders have been synthesized by solution polymerization route. The characteristics of the synthesized powder and functional properties of the sintered material have been evaluated.

6.2   Experimental

6.2.1   Preparation of precursor powders of GdCoO₃ and Ba-doped GdCoO₃

Fine powder of $GdCoO_3$ was synthesized by solution polymerization method starting with metal nitrates, and a mixture of sucrose and polyvinyl alcohol (PVA) as polymerizing agents. $Gd(NO_3)_3.6H_2O$ (purity > 99.9%, Indian rare Earth Limited, India) and $Co(NO_3)_2.6H_2O$ (purity > 99.98%, Alfa Biochem, India) were taken in 1:1 molar ratio and dissolved in deionized water. Sucrose and PVA were added to the mixed nitrate solution with stirring on a hot plate. The quantity of sucrose and PVA (10% W/V) were 4 moles and 0.8 moles per mole of metal nitrate. The pH of the solution was maintained at around 1.0 by adding citric acid to the solution. Viscous gel was formed on dehydrating the solution on a hot plate. Further heating led to charring of the gel and formation of black precursor powder. Precursor powders of barium substituted (10 mol% and 15 mol %) $GdCoO_3$ powders were also prepared by solution polymerization as described above. $Ba(NO_3)_2$ (purity > 99.0%, E-Merck, India) was used for the synthesis of doped gadolinium cobaltite.

6.2.2 Thermogravimetry and Calcination of precursor powders

Thermo-gravimetry (TG) and Differential Scanning Calorimetry (DSC) of $GdCoO_3$ precursor powder sample was carried out on a TG-DSC instrument (SETARAM Setsys Evolution 1600). In this experiment platinum crucible was used and the sample was heated at a rate of 10 ^{o}C/min upto 1000 ^{o}C in flowing air environment. Based on the TG analysis the precursor powders of all three compositions were calcined at 800 ^{o}C. The flow sheet for the preparation of $GdCoO_3$ and Ba-doped $GdCoO_3$ powders is given in Fig. 6.1.
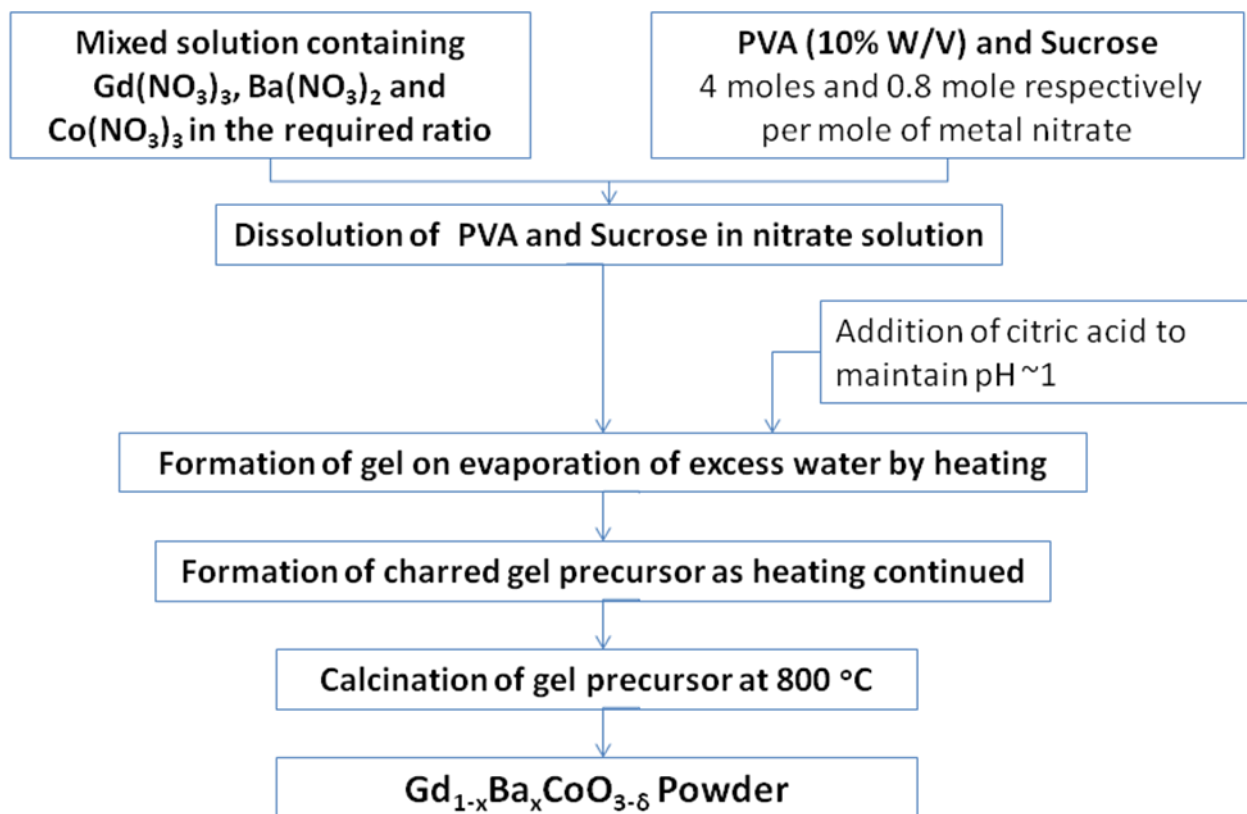
Fig. 6.1: Flow sheet for the preparation of $GdCoO_3$ and Ba-doped $GdCoO_3$ powders

6.2.3 Characterisation of calcined powders

Room-temperature X-ray diffraction (XRD) pattern of the calcined powders were recorded with an X-ray diffractometer (model PW1830, Philips) using Ni-filtered CuK_α radiation in the 2θ range from 10 to 70°. The phase purity of the calcined powder was confirmed by matching with standard PCPDF data. A small amount of $GdCoO_3$ calcined powder was dispersed in alcohol using ultrasonicator and subsequently deposited over a copper grid by dropping a droplet of the suspension over it. The carbon coated copper grid was used for observing the powder morphology by a transmission electron microscope (TEM).

6.2.4 Cold compaction and sintering of calcined powders

Cylindrical pellets of 6 mm diameter $\times$ 6 mm height (approx.) were prepared by uniaxial die pressing the calcined powders of each composition at 165 MPa. Shrinkage behavior of the powder compacts were studied using a dilatometer (model: SETARAM, SETSYS Evolution 1700) under a constant rate of heating (4 ^{o}C/min) upto 1300 °C. Based on the shrinkage study the green compacts of all three compositions were sintered at 1200 ^{o}C, 3 h. Densities of the sintered pellets were determined by water displacement method. The micrographs of the sintered pellets were taken by Scanning Electron Microscope (SERON 2000).

6.2.5 Evaluation of functional properties

Coefficient of thermal expansion (CTE) of the sintered pellets of all three compositions were determined from ambient to 1000 ^{o}C by using the same dilatometer that was used for sintering study. Rectangular bar samples of dimension 20 mm (L) $\times$ 5 mm (W) $\times$ 5 mm (B) were prepared by compacting pure and barium doped $GdCoO_3$ powders in a rectangular die followed by sintering at 1200 ^{o}C, 3 h. Four probe DC technique was used to measure conductivity of the rectangular bar shaped samples using a source meter unit.

6.3 Results and discussion

6.3.1 Synthesis of $GdCoO_3$ and Ba-doped $GdCoO_3$ powders

In the present work, PVA and sucrose have been used for synthesis of $GdCoO_3$ and Ba-doped $GdCoO_3$ powders by solution polymerization route. The details of synthesis are described in chapter 2. Metal nitrates in the aqueous solution are known to coordinate with the polymer formed by the mixture of PVA and sucrose at elevated temperature. The cation ratio is expected to be maintained in the gel network till the gel dries out and forms a charred mass. The charred mass is black in color and contains carbonaceous materials that need to be removed through calcination in air. To avoid the formation of hard agglomerates the calcination temperature is required to be as low as possible.

TG-DSC of the precursor powder (charred mass) gives an insight of different steps that occur during calcination. Fig. 6.2 shows the TG-DSC curves of the $GdCoO_3$ powder

precursor when heated in air. Continuous mass loss takes place up to 730 ^{o}C and thereafter mass gain is recorded in the temperature range from 730 to 780 ^{o}C.
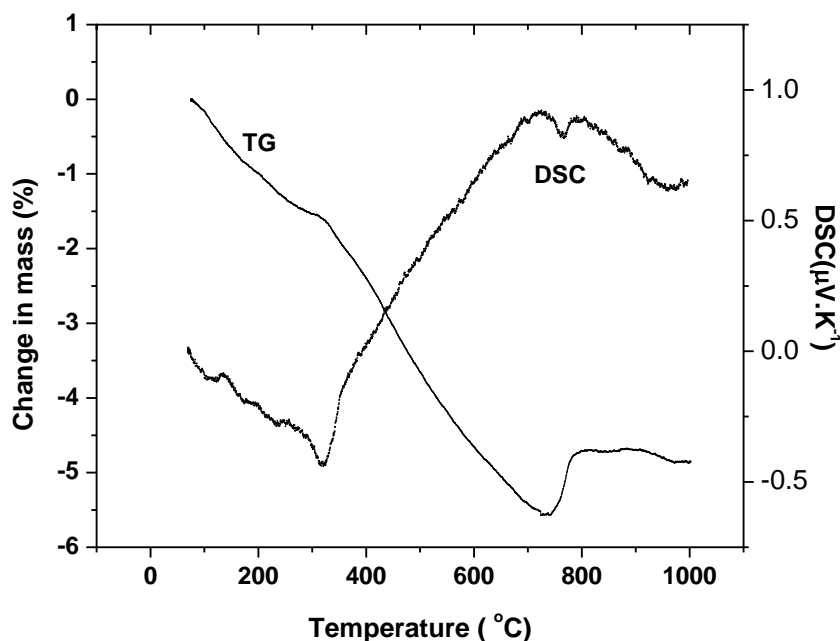
Fig. 6.2: TG-DSC curves of the GdCoO$_3$ powder precursor obtained by solution polymerization route

In the mass loss region two distinct portions can be identified. The slope of the DSC curve is found to change sharply at 310 ^{o}C. The mass loss upto 310 ^{o}C could be attributed to decomposition of PVA and sucrose and loss of water molecules. Further mass loss in the temperature range from 310 to 730 ^{o}C is due to burning of residual carbonaceous materials. The overall mass loss upto 730 ^{o}C is only 5.5%. It may be mentioned here that in this synthesis route metal nitrates act as oxidizer and helps in removing large quantity of carbonaceous material during drying of the gel. The weight gain in the temperature

from 730 to 780 ^{o}C is attributed to oxygen pick up associated with valency state change of Co^{2+} to Co^{3+} and formation of perovskite $GdCoO_3$ phase. At higher temperature the mass remains constant upto 920 ^{o}C. From the results as discussed above, the calcination temperature of the precursor powders was fixed at 800 ^{o}C for all the three compositions.

6.3.2 XRD of GdCoO$_3$ and Ba-doped GdCoO$_3$ powders

The X-ray diffraction pattern of $GdCoO_3$ powder obtained after calcinations is shown in Fig. 6.3. All the peaks in the X-ray diffraction pattern could be indexed to perovskite $GdCoO_3$ phase as reported in literature [215].
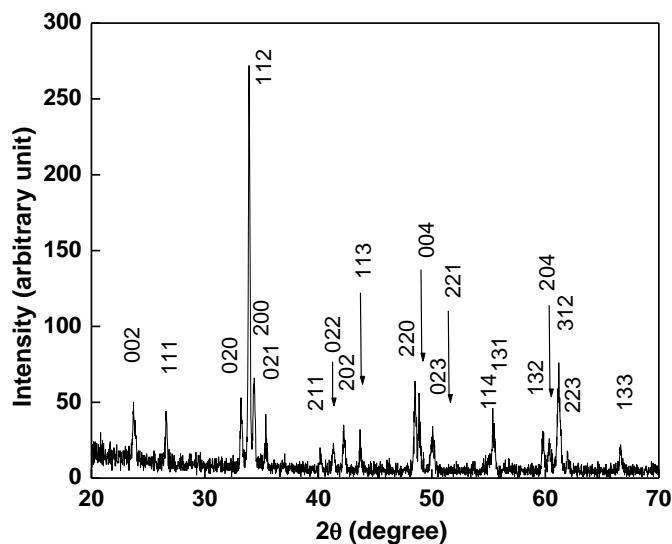
Fig. 6.3: X-ray diffraction pattern of GdCoO$_3$ powder (calcined at 800 ^{o}C)

The diffraction patterns of all the three compositions are shown in Fig. 6.4. The reference patterns for barium doped samples are not available in the literature. A shift in peak

109

position is observed in the diffraction pattern with respect to pure $GdCoO_3$. However, the perovskite type orthorhombic structure of $GdCoO_3$ remains unchanged in the range of barium substitution. No extra peak has been observed in the diffraction pattern indicating the complete solubility of barium in $GdCoO_3$ perovskite phase in the experimental range of substitution. As the ionic radius of Ba^{2+} is higher compared to Gd^{3+}, an increase in cell volume is expected.
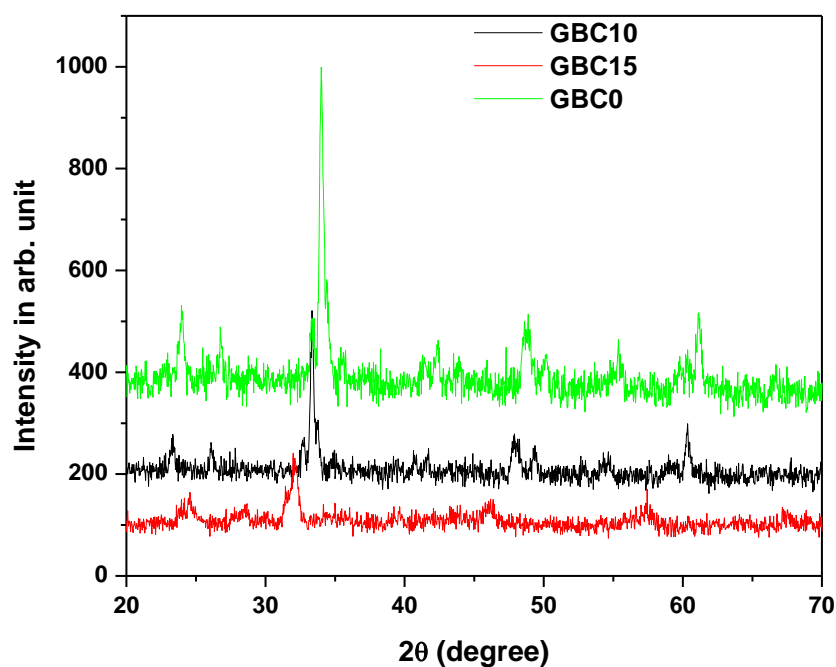
Fig. 6.4: X-ray diffraction pattern of Ba-substituted $GdCoO_3$ powder (calcined at 800 ^{o}C)

6.3.3 Morphology of calcined powder

The TEM micrograph of the calcined $GdCoO_3$ powder is shown in Fig. 6.5. The powder particles are found to be agglomerates of nano-size primary particles. The average primary particle size is about 30 nm. These agglomerates are soft in nature and break

110

during processing. Therefore, it can be inferred that solution polymerization process is capable of producing phase pure nano-crystalline GdCoO$_3$ powder.
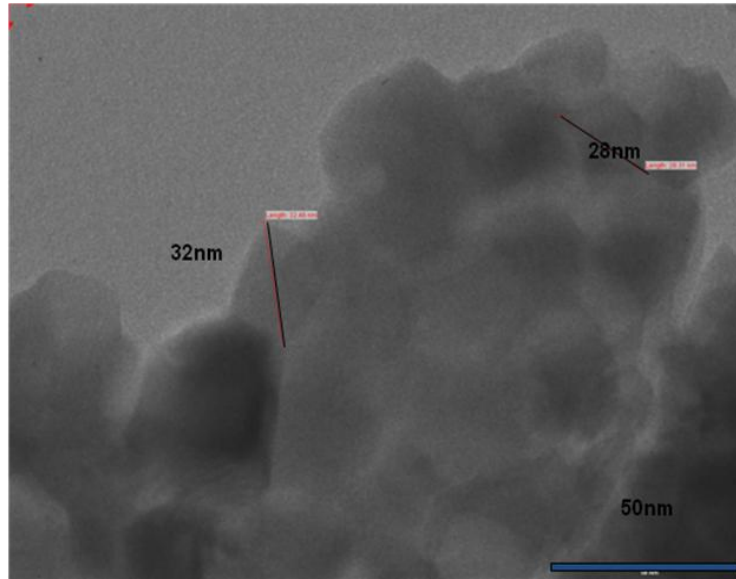
Fig. 6.5: TEM image of phase pure GdCoO$_3$ powder (calcined at 800 ^{o}C)

6.3.4 Sintering of GdCoO$_3$ and Ba-doped GdCoO$_3$ powders

The linear shrinkage (in terms of % change in length, Y) of GdCoO$_3$ and Ba doped GdCoO$_3$ green pellets on heating, as obtained from dilatometric experiment, is shown in Fig. 6.6(a-d). From the shrinkage pattern it is observed that linear shrinkage starts at around 850 ^{o}C for pure GdCoO$_3$ and 840 and 930 ^{o}C for 10 and 15 mol% barium doped GdCoO$_3$, respectively.
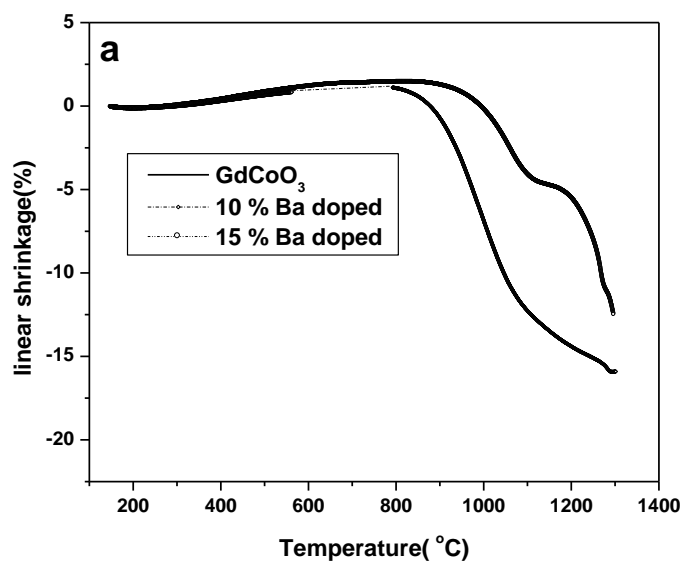
Fig. 6.6 (a) Shrinkage pattern of green pellets on heating in air upto 1300 ^{o}C

The differential curves of the shrinkage pattern are shown along with the shrinkage curve, which show the maximum shrinkage temperatures. For $GdCoO_3$ maximum shrinkage takes place at 1040 ^{o}C, and it is same for 15 mol% barium doped $GdCoO_3$. However, maximum shrinkage takes place at 990 ^{o}C for 10 mol% barium doped $GdCoO_3$. Therefore, $GdCoO_3$ based powders obtained by solution polymerization method can be sintered to full density by holding at these temperatures. For all compositions there are two stages of shrinkage. The two stage shrinkage behavior is attributed to the change in oxygen non-stoichiometry at higher temperatures.
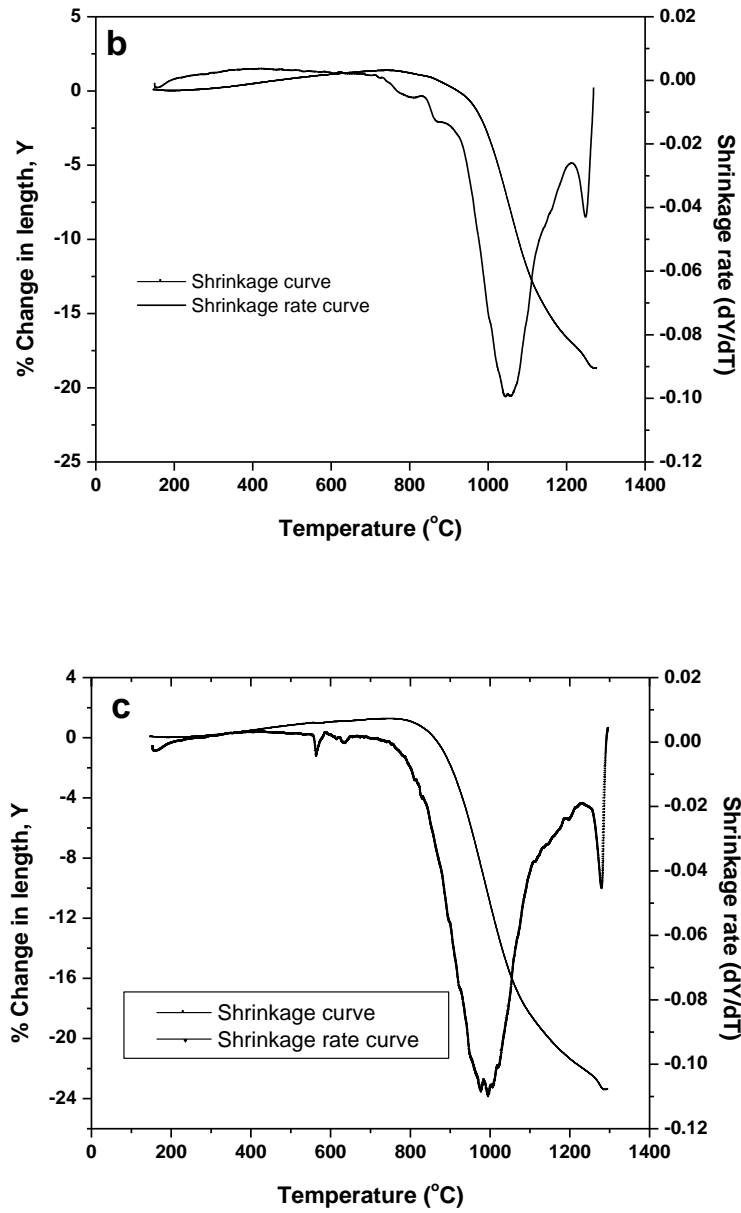
Fig. 6.6: Shrinkage pattern of green pellets on heating in air upto 1300 ^{o}C (b) GdCoO$_3$

(C) 10GBC

113
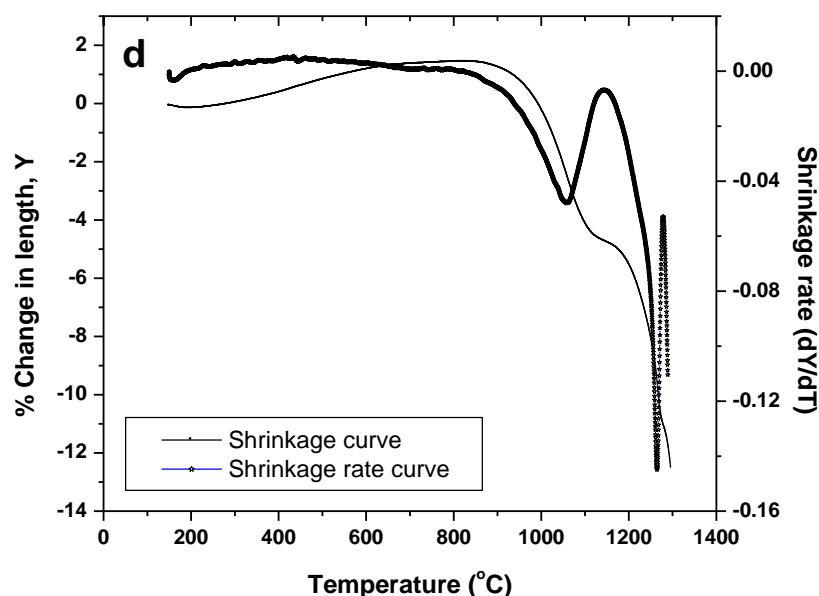
Fig. 6.6(d): Shrinkage pattern of green pellets of 15GBC on heating in air upto 1300 ^{o}C

Maximum shrinkage takes place in the first stage itself for pure and 10 mol% barium doped samples. However for 15mol% barium doped samples only 5 % shrinkage takes place up to 1168 ^{o}C and overall shrinkage of 11 %. It has been observed that the overall liner shrinkage decreases with barium doping. In the shrinkage rate curve a sudden increase in the shrinkage rate is observed at a temperature above 1200 ^{o}C. This may be attributed to the instability of $GdCoO_3$ phase at higher temperature [216].

In the present study $GdCoO_3$ has been sintered at 1200 ^{o}C for 3 h avoiding the instability region. The XRD pattern of the sintered sample is shown in Fig. 6.7. All the peaks in the XRD pattern could be indexed to perovskite $GdCoO_3$ phase. This confirms the stability of the perovskite $GdCoO_3$ phase upto 1200 ^{o}C.
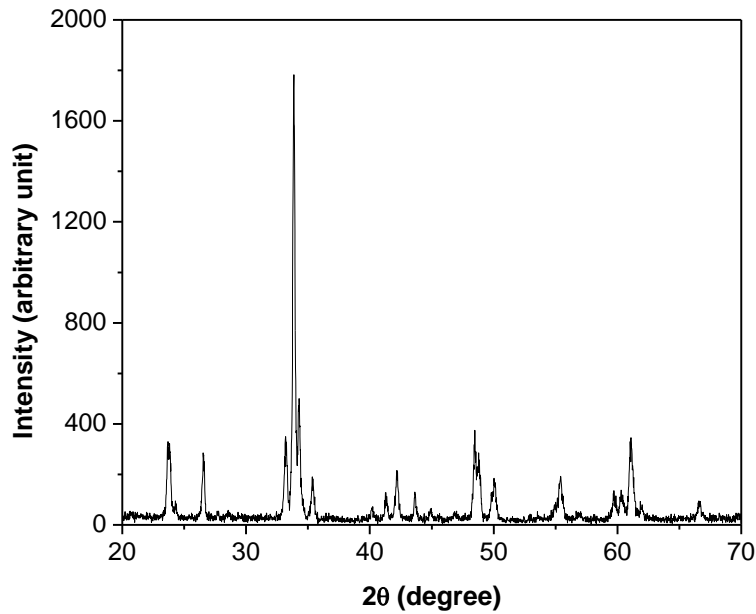
Fig.6.7: X-ray diffraction pattern of $GdCoO_3$ sintered at 1200 ^{o}C

From the shrinkage patterns it can be concluded that, $GdCoO_3$ based powders obtained by solution polymerization method can be sintered by holding at 1200 ^{o}C. In the present study all three compositions have been sintered at 1200 ^{o}C for 3 h to obtain dense samples that have used for measuring coefficient of thermal expansion and electrical conductivity. The sintered densities as measured by water displacement method were found to be 94 – 96% of theoretical density. The microstructures of the three dense $GdCoO_3$ based pellets sintered at 1200 ^{o}C are shown in Fig. 6.8.
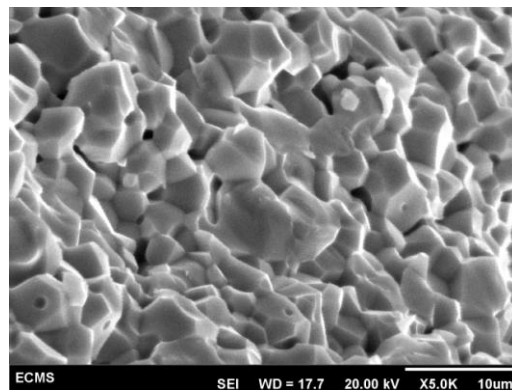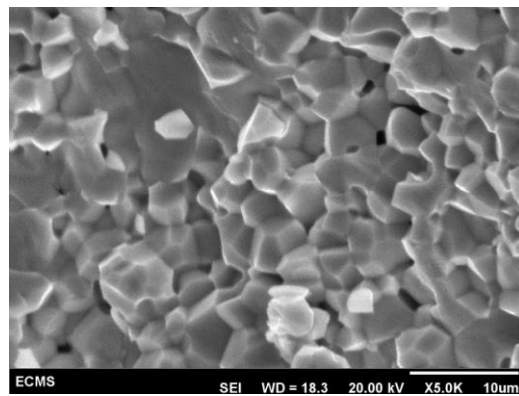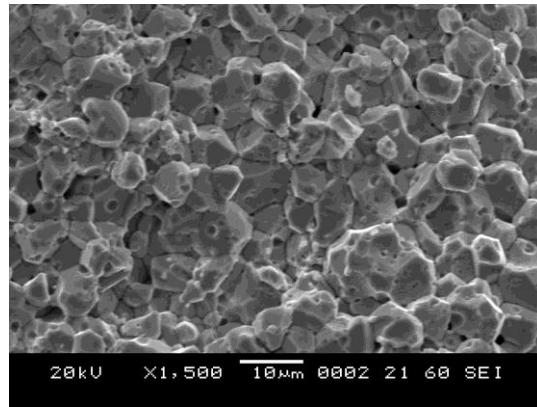
Fig. 6.8: SEM micrograph of pellet sintered at 1200 ^{o}C (a) GdCoO$_3$ (b)10GBC (c)

15GBC

6.3.5 Coefficient of thermal expansion

The percentage linear thermal expansion $[e_T = (\Delta L_{T-200})/L_0]$ of sintered $GdCoO_3$ in the temperature range from 200 to 1000 ^{o}C is shown in Fig. 6.9. The average value of coefficient of thermal expansion (α_T) has been estimated from the slope of the thermal expansion curve using the relationship: ($\alpha_T = e_T/\Delta T$). The average CTE is found to vary from 16×10^{-6} K^{-1} to 25×10^{-6} K^{-1} in the temperature range from 200 to 1000 ^{o}C. The average CTE remains on the lower side in the low temperature range. Steeper slope of the thermal expansion curve between 350 and 600 ^{o}C indicates average CTE as high as 25×10^{-6} K^{-1} in this temperature range. This phenomenon can be explained by lattice expansion associated with lattice oxygen loss leading to formation of oxygen vacancies.
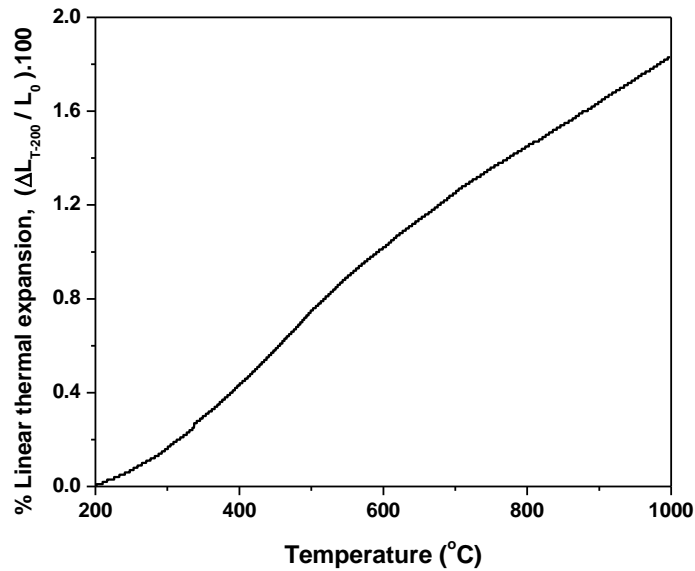
Fig. 6.9: Linear thermal expansion curve of $GdCoO_3$ sintered at 1200 ^{o}C

The TEC values of GdCoO$_3$ are much higher compared to the GDC electrolyte material. The GDC electrolyte material with nominal composition Ce$_{0.8}$Gd$_{0.2}$O$_{1.9}$ has an average TEC about 12.5 ×10^{-6} K^{-1} [217]. To avoid large mismatch in TEC a mixture of GdCoO$_3$ and GDC electrolyte material has been used in the evaluation of its electrochemical performance as a SOFC cathode material. The thermal expansion behavior of this composite electrode material has been discussed later.
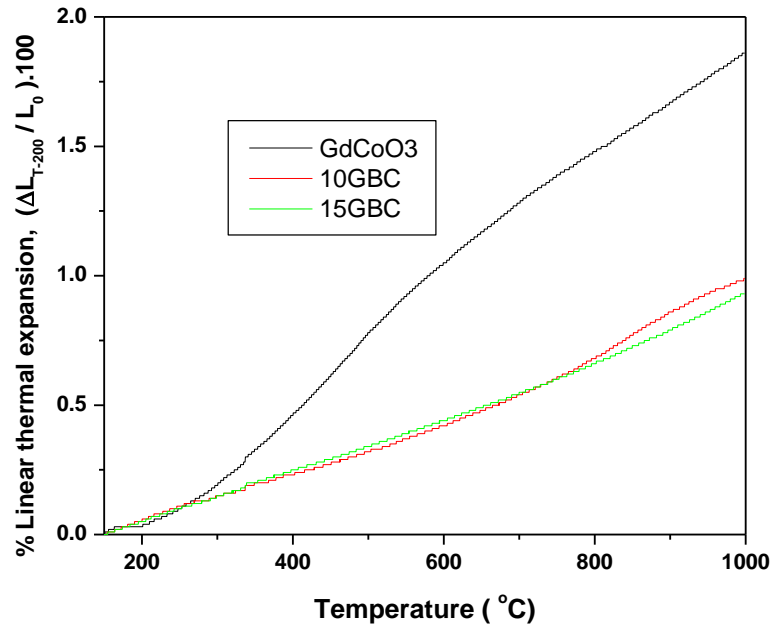
Fig. 6.10: Linear thermal expansion curve of GdCoO$_3$, 10 and 15 mol% barium doped samples

Fig. 6.10 shows the percentage linear thermal expansion of sintered GdCoO$_3$ and barium doped GdCoO$_3$ in the temperature range from 200 to 1000 ^{o}C. With 10% and 15% barium doping the average TEC value of GdCoO$_3$ was decreased to 13 and 12.5 ×10^{-6} K^{-1}

, respectively. With barium substitution the coefficient of thermal expansion as low as 10×10^{-6} K^{-1} is obtained in the intermediate temperature region (500-800 ^{o}C). Hence barium substitution has some positive effect on the thermal expansion coefficient of GdCoO$_3$ for use in SOFC as a cathode material. The thermal expansion coefficient is not linear from ambient to 1000 ^{o}C. There is a change in slope at around 600 ^{o}C. This change in thermal expansion value is associated with the change in oxygen non-stoichiometry of the material at higher temperature. This change in TEC is also reflected in the conductivity value as will be discussed later.

6.3.6 GdCoO$_3$-GDC composite

As mentioned earlier, GdCoO$_3$-GDCcomposite electrode has been used in the present study in order to have thermal expansion matching with GDC electrolyte. For the evaluation of CTE of this composite electrode material, the powder mixture of GdCoO$_3$ and GDC was sintered at 1200 ^{o}C In order to check the compatibility of these two materials XRD of the sintered material was carried out. XRD pattern of the composite sample sintered at 1200 ^{o}C is shown in Fig 6.11. The peaks corresponding to GDC are most prominent in the XRD pattern. The peaks corresponding to the GdCoO$_3$ apparently does not appear in the pattern. However, some additional peaks of low intensity appear in the pattern. It is observed that that there is no shift in the peak positions corresponding to GDC. This suggests that GDC has apparently not reacted with GdCoO$_3$. Also it was shown earlier in Fig. 6.8 that GdCoO$_3$ is stable on heating upto 1200 ^{o}C. Therefore,

suppression of GdCoO₃ peaks in the XRD pattern of the composite need to be analyzed further.
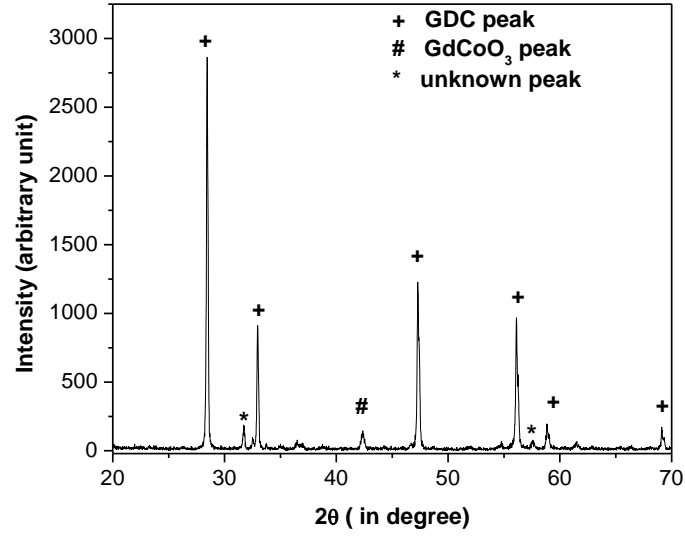
Fig. 6.11: X-ray diffraction pattern of GdCoO₃ –GDC mixture sintered at 1200 ᵒC
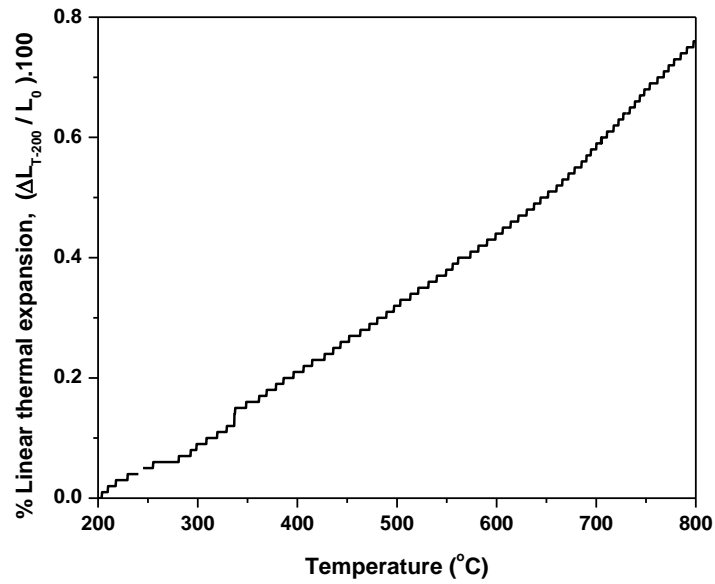
Fig.6.12 Linear thermal expansion curve of GdCoO₃-GDC composite sintered at 1200 ᵒC
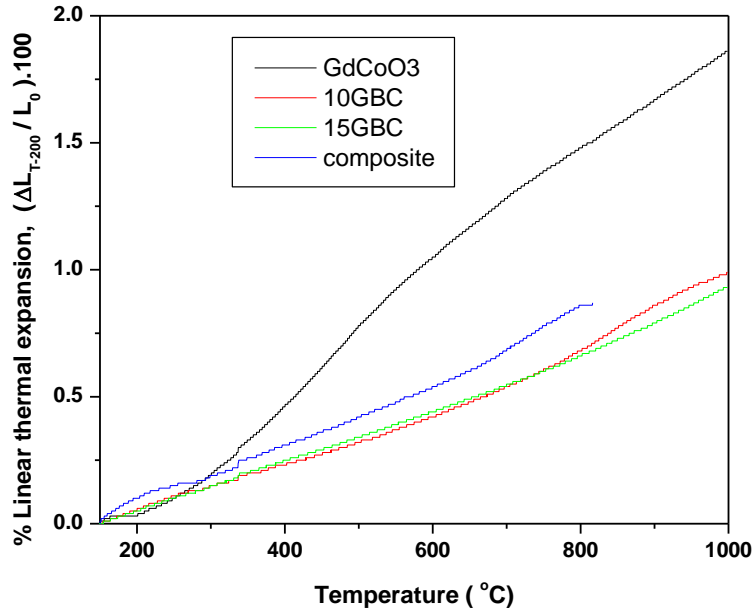
Fig.6.13: Linear thermal expansion curve of Ba doped $GdCoO_3$ and $GdCoO_3$-GDC

composite sintered at 1200 ^{o}C

Fig. 6.12 shows the thermal expansion curve of the composite sample sintered at 1200 ^{o}C. The average value of the coefficient of thermal expansion of the composite is calculated to be 12.9×10^{-6} K^{-1} in the temperature range 200-800 ^{o}C. This value is close to the CTE of GDC electrolyte material. Fig 6.13 shows the thermal expansion curves of gadolinium cobaltite doped with different levels of barium and compared with thermal expansion curve of the composite ($GdCoO_3$-GDC). TEC of barium doped samples are lower compared to pure $GdCoO_3$ and the composite ($GdCoO_3$-GDC).

6.3.7 Electrical conductivity of GdCoO$_3$

Fig. 6.14 shows the electrical conductivity of the sintered GdCoO$_3$ and barium doped GdCoO$_3$ pellets at different temperatures in the form of Arrhenius plot. High electrical conductivity has been observed in this material at intermediate temperatures. The measured conductivity is about 580 S.cm^{-1} at 800 ^{o}C. This value is in between the conductivity of La$_{1-x}$Sr$_x$CoO$_3$ (~1200 S.cm^{-1}) [218] and La$_{1-x}$Sr$_x$MnO$_3$ (~130 S.cm^{-1}) [219]. This higher value of conductivity is sufficient for current collection for SOFC cathode applications.
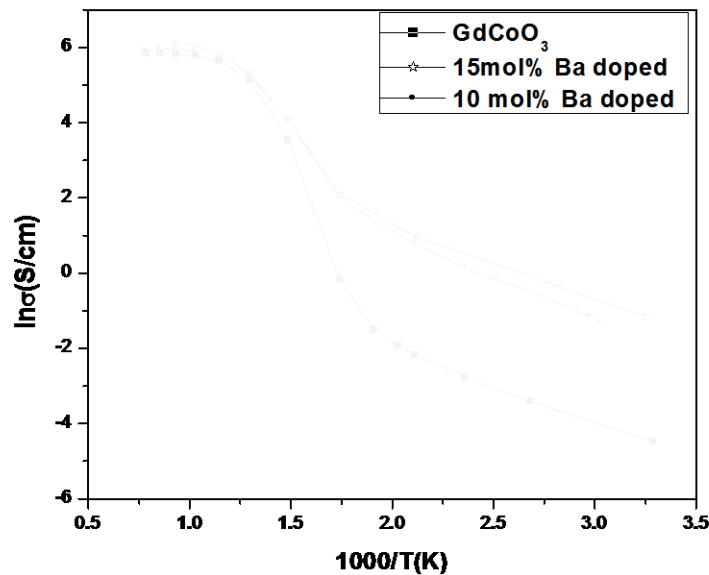
Fig. 6.14 Electrical conductivity of dense GdCoO$_3$ pellet sintered at 1200 ^{o}C

There is a change in slope of the Arrhenius plot of conductivity at around 400 ^{o}C indicating the change of conduction mechanism. The activation energies calculated from

the Arrhenius plot are 0.3 and 0.1 eV in the lower and higher temperature regions respectively. Low activation energy of the order of 0.1 eV may be attributed to the Mott type hopping conduction, i.e. small polaron hopping, between Co^{2+} and Co^{3+}. At lower temperature range additional activated mechanism for charge disproportionation reaction $(2Co^{3+} \rightarrow Co^{2+} + Co^{4+})$ [220] need to be considered and hence, the activation energy is higher. With barium doping the room temperature conductivity increases, attributed to the formation of holes responsible for increased electrical conductivity.

.

6.3   Summary

Phase pure nanocrystalline gadolinium cobaltate ($GdCoO_3$) powder has been synthesized by solution polymerization method and subsequently calcining the derived precursor at 800 ^{o}C. The synthesized powder has good sinterability and could be sintered to near theoretical density at 1200 ^{o}C. The thermal expansion coefficient of $GdCoO_3$ remains higher in comparison to GDC electrolyte. However, in $GdCoO_3$–GDC composite electrode matching CTE has been obtained. The electrical conductivity increases with increase in temperature and conductivity above 400 S.cm^{-1} has been obtained at 800 ^{o}C. The area specific resistance of the interface between composite electrode and electrolyte material is reasonably low and the value can be further brought down through optimization of process parameters. The results suggest that $GdCoO_3$ is a potential candidate material for application as SOFC cathode material.

CHAPTER 7

Evaluation of Electrode Performance by Electrochemical Impedance Spectroscopy (EIS)

7.1 Introduction

A significant fraction of internal resistance of a cell comes from the interfacial polarization at the electrode-electrolyte interface. The interfacial polarisation resistance depends on the catalytic activity of the electrode material and the length of the triple phase boundary. The electrochemical reaction occurs at the triple phase boundary (TPB), where the electrolyte, electrode and porosity (gas phase) co-exists. Absence of any of these three phases leads to hindrance to this electrochemical reaction [221].

In a cathode layer oxygen is passed through the porous layer and is reduced at the electrode-electrolyte interface as follows:

$\frac{1}{2} O_2$ (gas) + $2e^-$(cathode) $\longrightarrow$ O^{2-}(electrolyte)
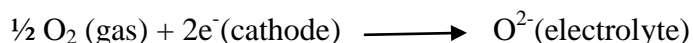
Though this reaction is heterogeneous in nature, the catalytic reaction is quite different from the normal reactions. The elementary reaction at the TPB is shown schematically in Fig. 7.1. At the TPB, any scarcity of reactants or accumulation of reaction products may lead to decrease in the rate of electrochemical reaction (concentration polarization). For these reasons, microstructure and composition play an important role in determining the reaction rate.

To increase this TPB two approaches are adopted. First, a mixed ionic and electronic material is used where mobility of both ions and electrons takes place in the single phase electrode. So the oxygen reduction reaction can also occur at the cathode surface away from the electrolyte. In the second approach a composite electrode comprising of cathode material and electrolyte material in definite proportion is used. The reaction sites for the electrochemical reduction of the oxygen are enhanced with this porous composite electrode where electrical conductivity of the cathode and ionic conductivity of the electrolyte contributes in extending the reaction zone in contrast to a pure electronically conducting material.

Many authors pursued a composite electrode (mixture of electrode and electrolyte in definite ratio) approach to decrease this polarization resistance [222-225]. Several others have gone for a mixed ionic and electronic conductor (MIEC) to improve the performance [226-228]. In an electrode layer both composition and microstructure can be tailored for better result.
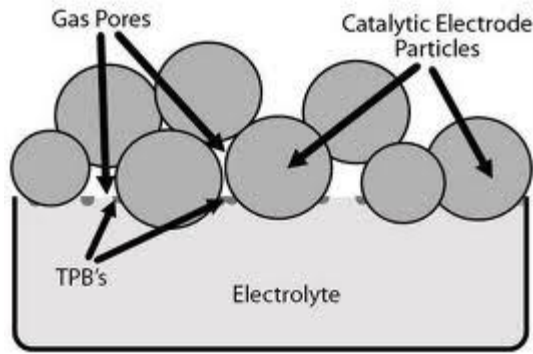
Fig.7.1: Schematics of triple phase boundary area (TPB)
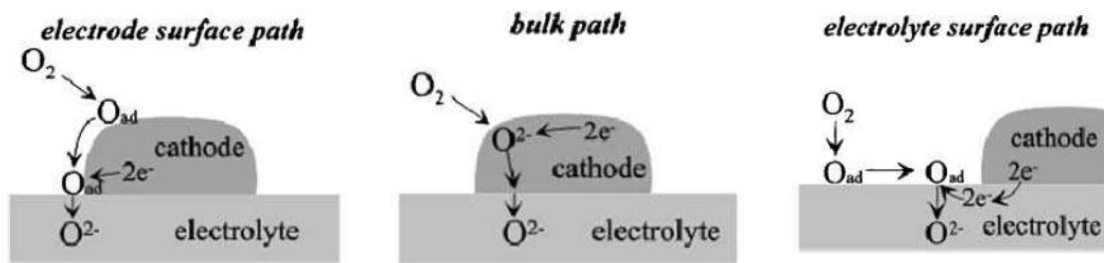
Fig.7.2: Schematics of the oxygen reduction reaction paths at cathode

The elementary reactions at the cathode consist of few surface reactions and bulk phenomena. The diatomic molecule (O_2) under goes several intermediate steps in the oxygen reduction reaction. These reactions are limited to the TPB and nearby area [229,230]. There are three elementary reactions at the cathode and these are [231,232] (a) Adsorption of oxygen molecule on the cathode surface, dissociation of oxygen molecule on the cathode surface, dissociation into anions and incorporation into the bulk of the cathode, (b) Transport of the anion towards the electrolyte through the cathode, and (c)

Transfer of anion from cathode to electrolyte. Though there are three primary reaction paths, several steps may be rate limiting for the oxygen reduction reaction. Since the cathodic polarization resistance is the biggest contributor for the cell resistance, optimization of cathode catalytic property will govern the overall performance. The cathodic reaction path for perovskite type cathode material is explained by Fleig [233]. The three possible paths for oxygen transport namely cathode surface path, the bulk path and the electrolyte surface path are shown in Fig. 7.2. These three paths correspond to an electronic conductor, an MIEC conductor and a composite electrode. Reaction at the cathode may take place through any route or combination of all the three. However the actual reaction path depends on temperature, oxygen partial pressure at that point and microstructure. Therefore, it is difficult to predict the exact rate limiting steps in the oxygen reduction reaction. However, doing experiments at various oxygen partial pressures, with well defined microstructure gives an insight of the actual reaction path ways and limiting steps. In the present chapter, doped $GdCoO_3$, a mixed ionic and electronic conductor has been used as cathode material and composite electrode approach has been adopted to decrease the polarization resistance.

In the composite cathode the electron transfer reactions is shown in Fig. 7.3. Oxygen reduction reaction takes place whole over the MIEC cathode and addition of electrolyte layer extends the TPB length. Hence better ASR is observed.
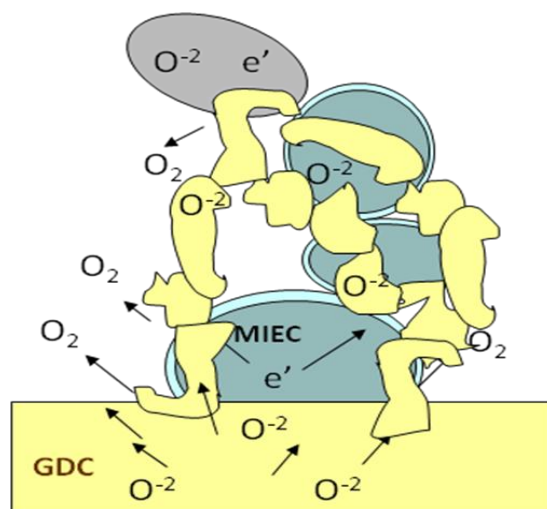
Fig. 7.3: Electrochemical reactions in a composite cathode

Nickel is a promising material for a SOFC anode because of its higher catalytic activity for hydrogen oxidation reaction and dehydrogenation of hydrocarbons. Current research on SOFC anode deals with development of anode material capable of operating on natural gas, without carbon deposition resulting from catalytic cracking. Ceria based anodes have potential to suppress carbon deposition at anode while operating with natural gas [234-236]. For avoiding the sintering of the anode material it has been used along with the electrolyte material (GDC). However, the amount of electrolyte has to be optimised in the anode composition. With electrolyte addition the resistance of the anode material increases. Again, the higher mobility of lattice oxygen and higher concentration of vacancies in the doped ceria system increases the catalytic surface (TPB) from the interface to whole surface of the mixed conductor [237]. The catalytic properties at the anode side are measured by AC impedance spectroscopy and the reaction rate has been analyzed by from the impedance graph. In the present chapter symmetric cells has been fabricated using this anode material and characterized by impedance spectroscopy.

7.2 Experimental

7.2.1 Cathode symmetric cell fabrication

Symmetric cells were prepared by depositing the electrode materials on dense GDC electrolyte. Dense GDC discs of 12 mm diameter × 2 mm thick were prepared by die pressing fine GDC powder in a uniaxial die followed by sintering at 1250 ^{o}C. Fine GDC powder synthesized by combustion method was used for this purpose. The final dimensions of the sintered pellets were ~1.5 mm in thickness and ~11mm in diameter. Slurry of the electrode materials was prepared in terpineol medium using ethyl cellulose as binder. Slurries of the cathode materials were prepared by mixing the power with terpinol (in weight ratio 1:1) in a ball mill for more than 24 hours for better mixing and homogenization. In some cases graphite pore former (10 wt %) was added in the slurry during the ball milling stage for developing porosity in the sintered body. Different cathode compositions which have been prepared are listed in Table 7.1.

The symmetric cells were prepared by brush painting the cathode slurry on both the parallel faces of the GDC electrolyte material. Care was taken to ensure that the cathode layers on both the sides are not in contact with each other. After application of cathodes on both the sides of the GDC electrolyte discs the samples were fired at 1100 °C to form symmetric cell. In some experiments an electrolyte slurry prepared in the similar manner in terpinol medium was applied over the dense electrolyte layer prior to the cathode coating.

Table 7.1: Different cathode compositions used for making symmetric cells

Cathode material code	Cathode material composition
GC	pure $GdCoO_3$
GB10C	$Gd_{1-x}Ba_xCoO_{3-\delta}$ (x = 0.1)
GB15C	$Gd_{1-x}Ba_xCoO_{3-\delta}$ (x = 0.15)
GC-GDC	$GdCoO_3$-GDC composite powder
GB10C-GDC	$Gd_{1-x}Ba_xCoO_{3-\delta}$ –GDC composite; x = 0.1
GC-GDC-G	GC-GDC with 10% graphite pore former
GB10C-GDC-G	GB10C-GDC with 10% graphite pore former
GB15C-GDC-G	GB15C-GDC with 10% graphite pore former

7.2.2 Anode symmetric cell fabrication

For characterization of NiO-GDC anode material, symmetric cells have been prepared with GDC electrolyte material. NiO and GDC in weight ratio 1:1 was ball milled in ethanol medium for intimate mixing. Organic slurry of the electrolyte material (GDC) was prepared in terpinol medium. NiO-GDC powder was pre-compacted in a pellet form at 65MPa pressure using a uniaxial die. Keeping the pellet inside the die, electrolyte slurry was applied through a brush over the anode pellet. After drying of the electrolyte layer, NiO-GDC powder was filled in the same die and pressed at 150 MPa pressure. This resulted in a thin layer of electrolyte sandwiched between two thick anode layers. The whole symmetric cell was co-pressed at 1250 ^{o}C. This type of symmetric cell

fabrication has been adopted to simulate the condition of a co-pressed and co- sintered anode supported cell where electrolyte and anode are co-pressed and sintered together.

The symmetric cells prepared as mentioned above were mounted in a Probostat® (Norweigian Electro Ceramics AS, Norway) sample holder using spring load. Both sides of the symmetric cells were connected through platinum electrodes using platinum mesh. Impedance measurements of the symmetrical cells were carried out in the temperature range from 700 to 900 $^{\circ}$C. A Solartron 1260 frequency response analyzer was used for the impedance measurement in the frequency range 10^5 to 0.1 Hz. The applied ac voltage amplitude was set at 30 mV. Cathode symmetric cell measurements were done in flowing air atmosphere where as anode symmetric cells were tested under humidified hydrogen atmosphere. The area specific resistance (ASR) for interfacial polarisation, R_p, was evaluated from the complex impedance plots using Z-view software. The micrographs of the fractured surfaces of the symmetric cells were taken using scanning electron microscope.

7.3 Results and Discussion

As mentioned above, $GdCoO_3$ based electrodes have been integrated with GDC electrolyte by various approaches. The performance of electrodes has been evaluated by electrochemical impedance spectroscopy. The complex impedance plots have been normalized for unit cell constant in order to compare the performances of electrodes. The results have been discussed in correlation with microstructure of the electrode-electrolyte interface.

7.3.1 Symmetric cells formed using pure and Ba-doped GdCoO$_3$

Fig.7.3 shows the complex impedance plots of symmetric cells formed using GC and GB10C at different temperatures. The ASR values obtained at different temperatures are given in Table 7.2. It has been observed that the ASR value decreases with increase in temperature. This is due to increase in catalytic activity of the cathode materials with increase in temperature. Although this trend is very clear in case of GB10C electrode, the variation of ASR with temperature has been found to be abrupt. There is a large difference in the thermal expansion coefficient of pure GdCoO$_3$ and GDC electrolyte material. This is likely to result in delamination at the interface during heating and cooling. Fig. 7.4 shows the SEM micrographs of the electrode-electrolyte interfaces of the symmetric cells formed using GC and GB10C electrode. Delamination at the interface is clearly visible in the microstructures. Therefore, the contact between the electrode and electrolyte may change in a non-predictive manner depending on applied spring load of the sample and temperature.

At 900 ^{o}C, ASR values are as high as 6 and 3 ohm.cm^2 for GC and GB10C, respectively. These values are too high for practical applications. Small contact area due to separation of cathode layer at the interface is primarily responsible for the high values of ASR.
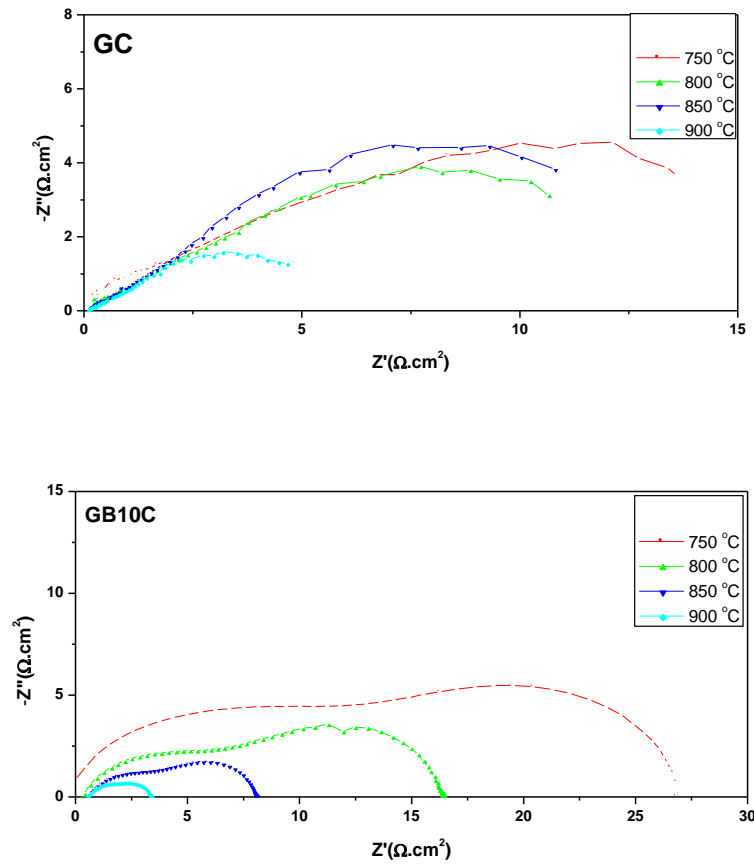
Fig 7.3 Complex impedance plots of symmetric cells of GC and GB10C.

Table 7.2: ASR values of symmetric cells of GC and GB10C at different temperatures

Temperature (^{o}C)	ASR of symmetric cells ($\Omega.cm^2$)	
	GC electrode	GB10C electrode
750	16	27
800	14	16
850	12.5	8
900	6	3
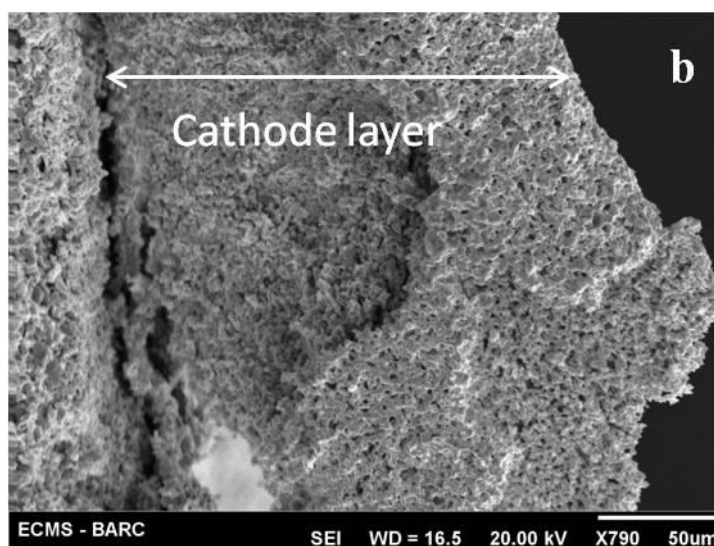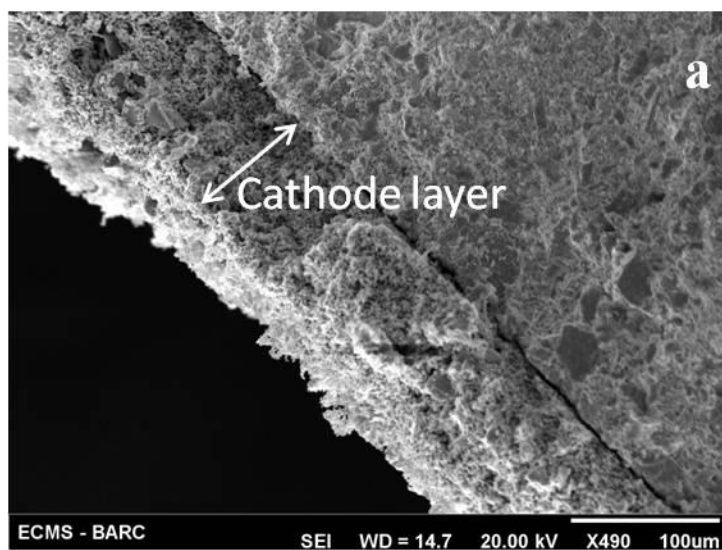
Fig. 7.4: SEM micrographs showing the electrode-electrolyte interfaces. (a) GC electrode
(b) GB10C electrode

7.3.2 Effect of electrolyte interlayer on ASR value

In the previous section it has been observed that thermal expansion plays an important role in determining the interfacial microstructure and the ASR value. The triple phase boundary area can be improved through better adherence of electrode material to the electrolyte. With this objective a very thin layer of electrolyte was deposited over the dense electrolyte pellet. After drying of this interlayer, cathode layer was applied. As the electrolyte interlayer and the cathode layer were sintered at a temperature lower than the sintering temperature of the electrolyte material, porosity was expected in the interlayer. However, due to very thin layer the increase in the cell resistance is not expected to be significant. The variation of ASR value with temperature for two cathode compositions, GC and GB10C with an interlayer of porous thin electrolyte layer is shown in Fig 7.5. It has been observed that with addition of inter layer of GDC, the ASR value of GC cathode decreases from 6 to 3 ohm.cm^2 at 900 ^{o}C and from12 to 7 ohm.cm^{-1} at 800 ^{o}C. Similarly, for GB10C cathode the ASR value decreases from 4 to 2 ohm.cm^2 at 900 ^{o}C and from 16 to 7 ohm.cm^2 at 800 ^{o}C.

SEM micrographs of the two sample interfaces are shown in Fig. 7.6. Porous interlayer of GDC is clearly seen from both the micrographs. However, an overall decrease in porosity is observed for the cathode layer. Both interlayer and the cathode layer are sintered at 1150 ^{o}C for sticking of porous electrolyte layer with the sintered electrolyte layer. Though there were some improvements in the ASR value with interlayer addition, it was not sufficient for appreciable decrease in the polarization resistance.
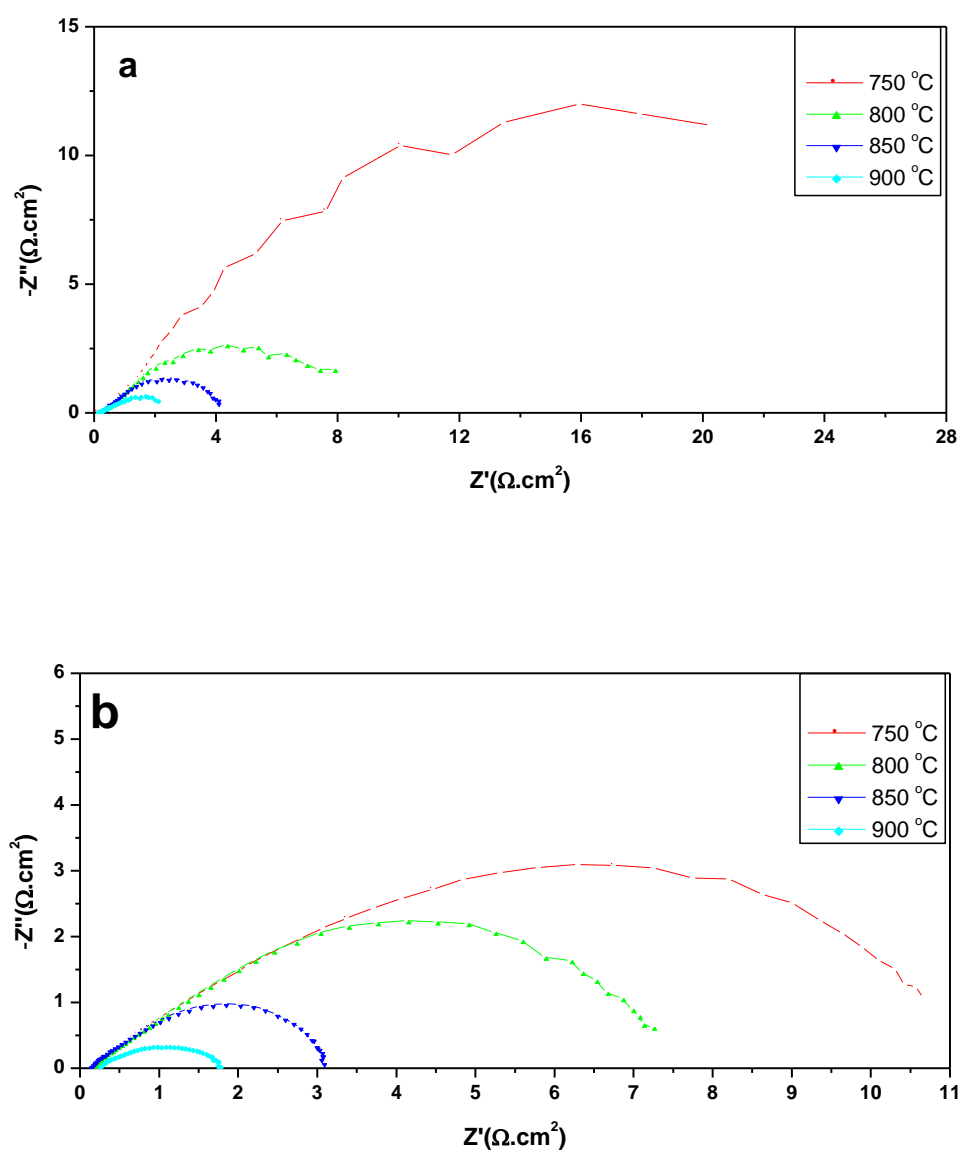
Fig 7.5 Complex impedance plots of symmetric cells formed using electrolyte interlayer (a) GC (b) GB10C
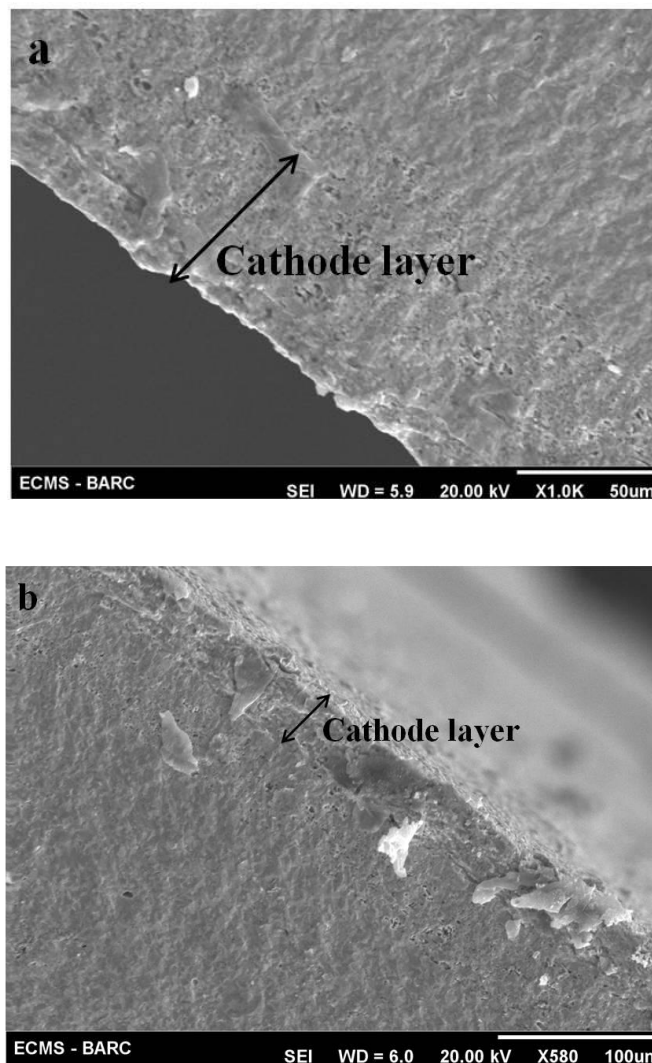
Fig. 7.6 SEM micrographs showing the electrode-electrolyte interfaces of symmetric cell formed using GDC interlayer. (a) GC electrode (b) GB 10C electrode

7. 3.3 Symmetric cells using composite electrode

As discussed in previous chapter, mismatch in thermal expansion coefficient can be circumvented to a large extent by composite electrode approach. In composite electrode a mixture of cathode and electrolyte is used as cathode layer for improving the catalytic surface. In the present investigation a mixture of cathode material and electrolyte material

was taken in the weight ratio 1:1. Fig. 7.7 shows the impedance plots of symmetric cells formed using composite electrodes
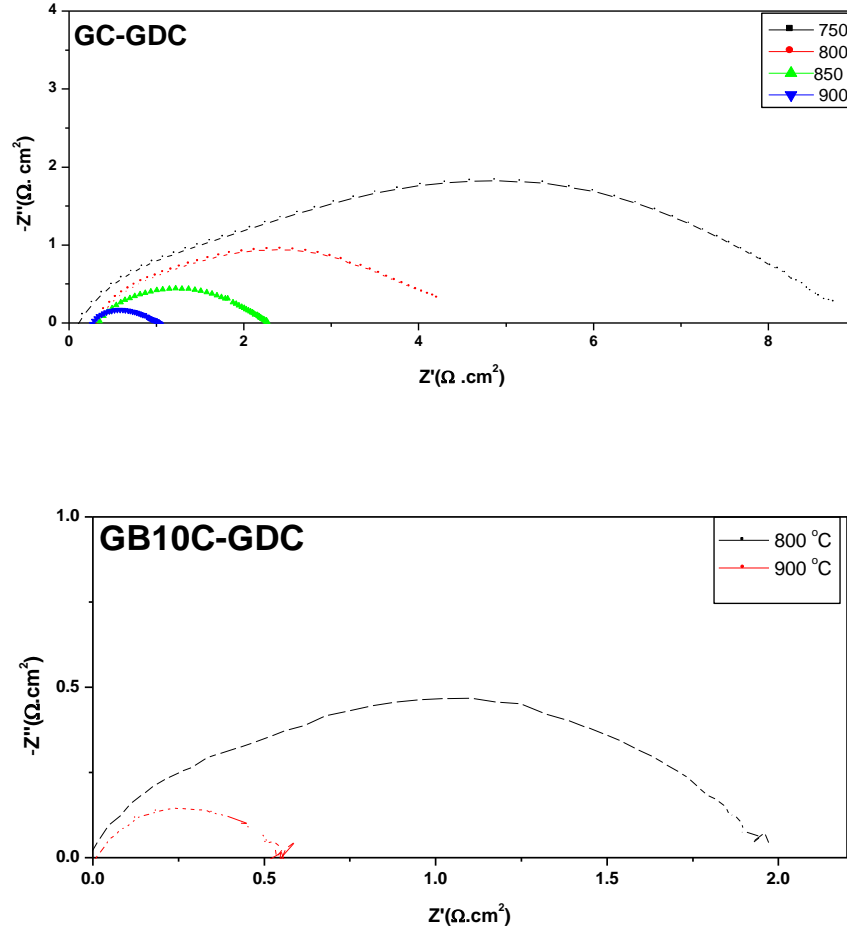
Fig. 7.7: Complex impedance plots of symmetric cells formed using composite electrodes

The ASR values for the composite cathode using pure $GdCoO_3$ were 4.2 and 1.0 ohm.cm^2 at 800 and 900 ^{o}C, respectively. The ASR value of 10mol% barium doped composite cathode samples are 1.9 and 0.6 ohm.cm^2 at 800 and 900°C, respectively. These lower values of ASR can be attributed to the extension of triple phase boundary in

the composite electrode. There are two distinct advantages of the composite cathode, one is the enhancement of the catalytic property by way of increasing the TPB length and the other is the matching of thermal expansion coefficient with the electrolyte material.
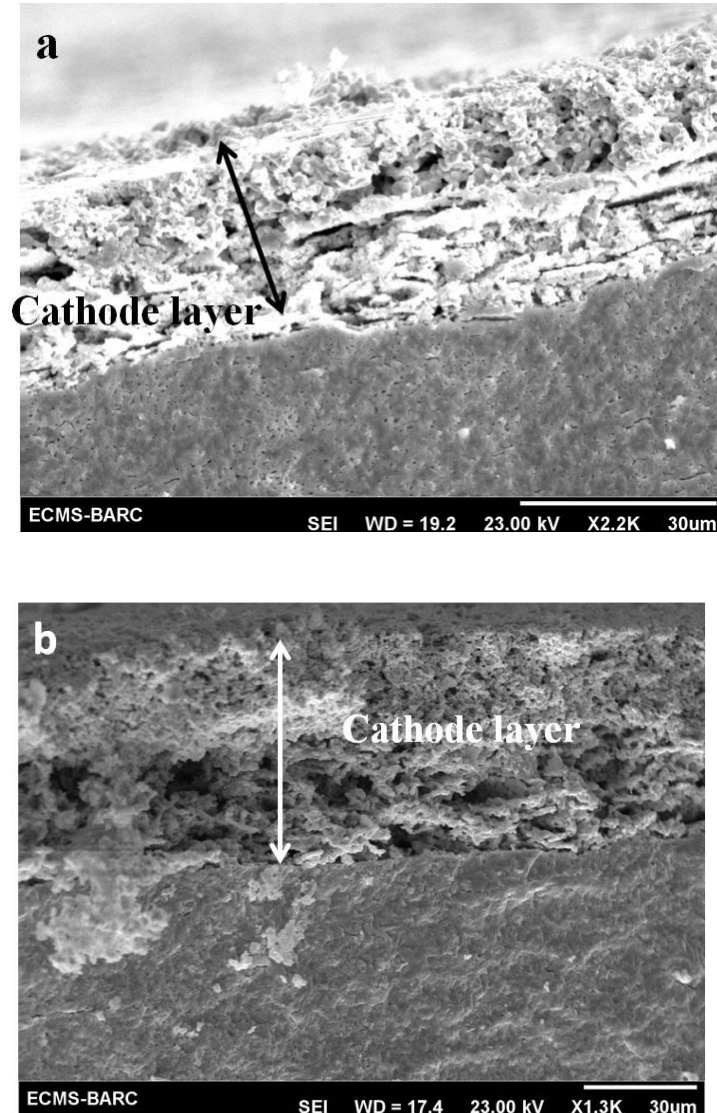
Fig. 7.8 SEM micrographs showing the electrode-electrolyte interfaces of symmetric cell formed using composite electrode (a) GC-GDC electrode (b) G10BC -GDC electrode

The scanning electron micrographs of the symmetric cells with composite cathode using $GdCoO_3$ and Ba doped (10 mol %) $GdCoO_3$ are shown in Fig. 7.8. At the interface, good

adherence of the cathode and the electrolyte is observed with fine porosity and interconnected porosity extending to the whole cathode layer. This increased porosity also helps in increasing the triple phase boundary area. In a composite cathode, both materials have different shrinkage kinetics, hence uniform porosity is developed over the entire area and better TPB is achieved.

7.3.4 Effect of pore former on interfacial polarization

As observed in the micrographs of composite electrodes pore structure develops in the electrode without addition of pore former. Porosity in the electrode can be further improved with addition of pore former. Very high amount of porosity leads to decrease in the conductivity value. In the present study graphite (10 wt.%) has been used as pore former during the slurry preparation stage. Fig. 7.9 shows the complex impedance plots for composite cathode powders mixed with 10 wt.% graphite pore former. ASR values for GC-GDC-G, GB10C-GDC-G and GB15C-GDC-G at 850 ^{o}C are 0.5, 0.3 and 0.3 ohm.cm^{2}, respectively. It has been observed that with barium substitution the ASR value decreases. However for GB10C-GDC-G and GB15C-GDC-G samples, there is no appreciable change in the ASR value. At 900 ^{o}C the ASR value for GB10C-GDC-G sample is as low as 0.09 ohm.cm^{2}. The SEM micrographs of the three symmetric cells after experiment are shown in Figure 7.10. From the micrograph it is clear that fine cathode particles are well distributed in the network of bigger electrolyte particles and there is continuity in the cathode network. Combinations of large and fine pores are observed in the microstructure. The larger pores are developed due to graphite burn out

during firing and the finer pores are developed inherently in the composite cathode. For a particular porosity level, well distributed fine pores are expected to provide higher TPB area in the electrode structure. Cathode polarization resistance lower than $0.1 ohm.cm^2$, makes Ba-doped $GdCoO_3$ as a candidate SOFC cathode material.

Table 7.3 ASR values of symmetric cells of GC and GB10C at different temperatures

Temperature (^{o}C)	ASR of symmetric cells ($\Omega.cm^2$)		
	GC-GDC-G electrode	GB10C-GDC-G electrode	GB15C-GDC-G electrode
800	1.0	0.7	0.8
850	0.5	0.3	0.3
900	0.25	0.09	--
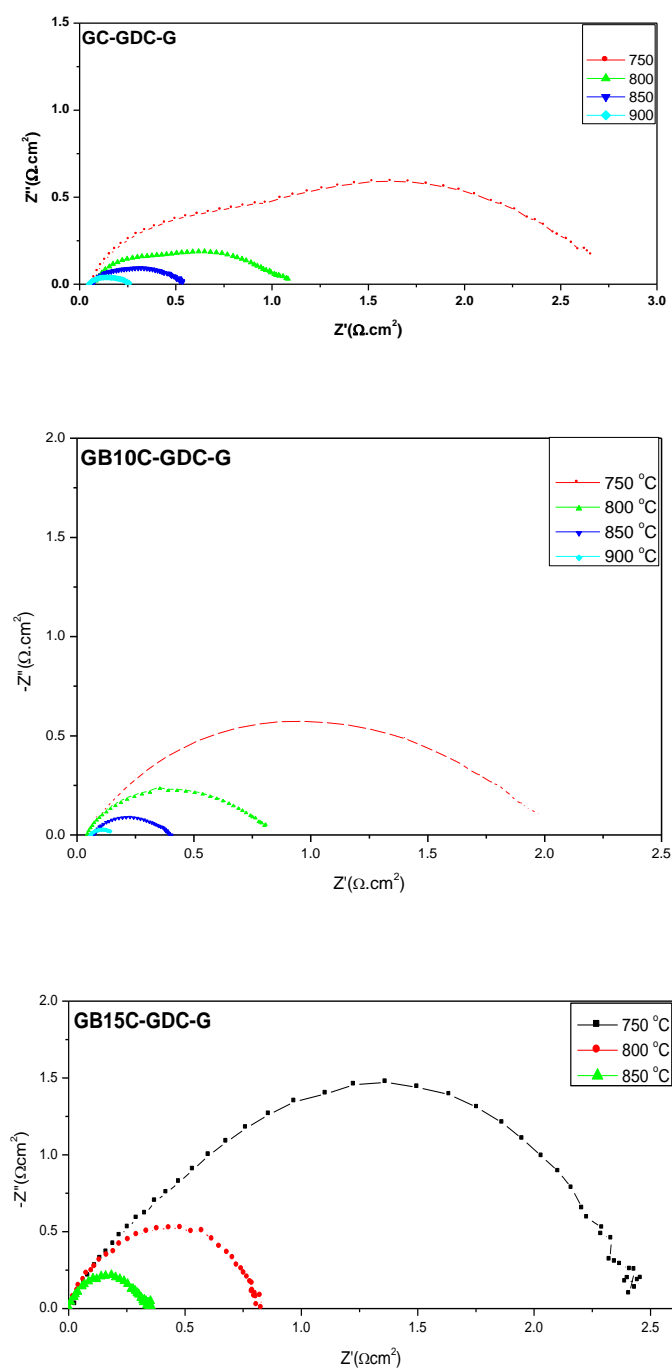
Fig. 7.9 Complex impedance plots of symmetric cells formed using composite electrodes.
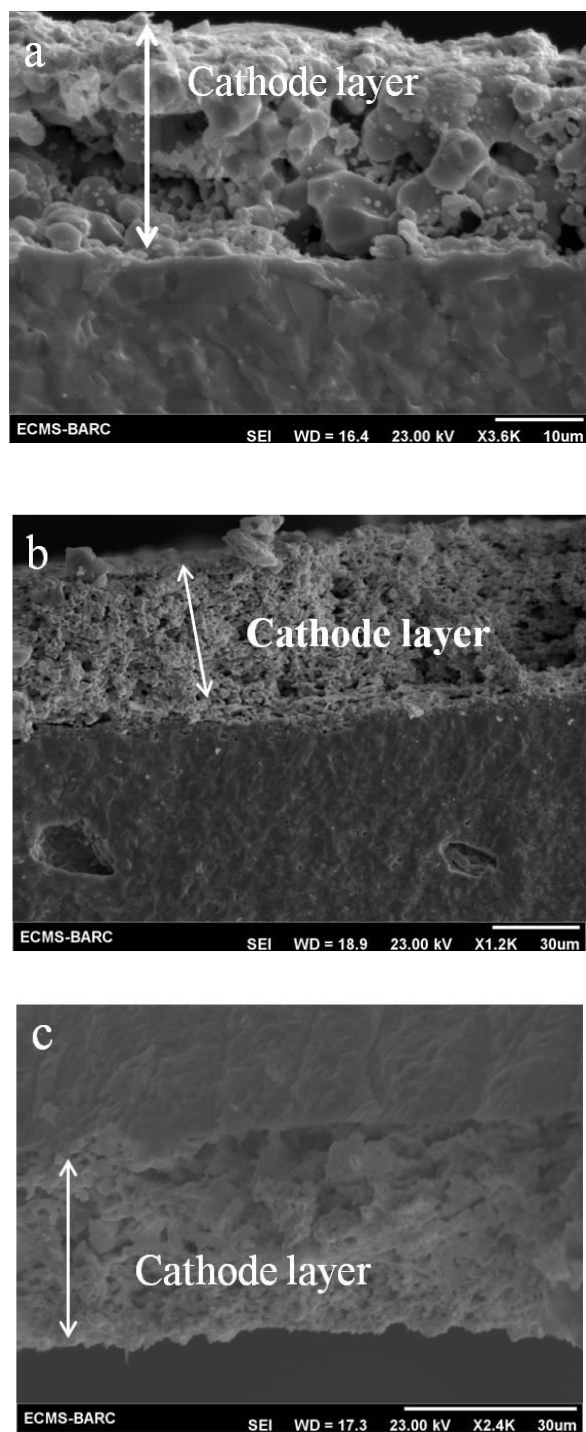
Fig. 7.10 SEM micrographs showing electrode-electrolyte interfaces of symmetric cells

of (a) GC-GDC-G electrode (b) GB10C-GDC-G electrode (c) GB15C-GDC-G electrode

7.3.5 Characterization of anode symmetric cell

Anode material comprising of NiO-GDC composite (1:1 weight ratio) was ball milled vigorously prior to use as SOFC anode material. Here, thin electrolyte layer was developed between two thick anode layers for symmetric cell measurement. As anode supported single cells will be fabricated for cell testing, this approach was adopted for developing thin electrolyte based symmetric cells, instead of conventional thick electrolyte supported symmetric cells. Impedance measurements were carried out in hydrogen environment to ensure the anode environment of a fuel cell. The variation in the area specific resistance with temperature is shown in Fig 7.11. ASR value as low as 0.06ohm.cm^2 was obtained at 600 ^{o}C and 0.048ohm.cm^2 at 800 ^{o}C. This very low value of ASR is helpful for good cell performance.
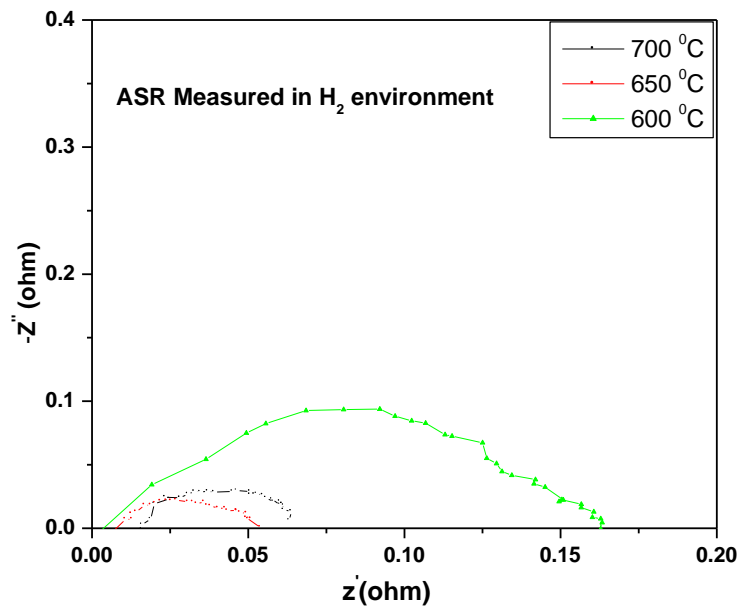
Fig.7.11 Variation of ASR with temperature for NiO-GDC/GDC symmetric cell

The SEM micrograph of the symmetric cell after the experiment is shown in Fig 7.12. This shows a dense electrolyte and a porous anode layer. Since the surface nickel particles are oxidised to NiO, there seems a decrease in porosity in the anode layer. However, 17% porosity is developed by the reduction of NiO to Ni, as per simple mathematics. Long term study will be carried out on to evaluate the performance of the anode layer with aging.
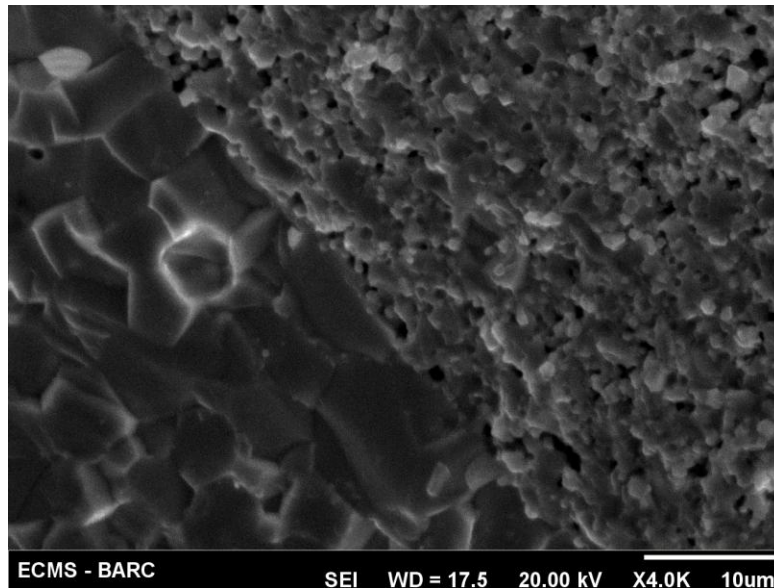
Fig: 7.12 SEM micrograph NiO-GDC/GDC symmetric cell

7.4 Summary

Thermal expansion of $GdCoO_3$ and Ba doped $GdCoO_3$ are higher compared to GDC electrolyte material. Hence separation of cathode layer takes place in the fabrication stage

of the symmetric cell using these materials alone. With addition of an interlayer of thin electrolyte layer between the cathode and electrolyte layer improves the ASR value compared to the pure cathode material and gives adherence of cathode to the electrolyte. However, the ASR value of pure cathode material and cathode layer with inter layer of electrolyte are in the higher side for practical applications. When a composite of cathode and electrolyte material is used in the symmetric cell, a huge decrease in the ASR value is observed. With the addition of electrolyte to the cathode composition both catalytic property and thermal expansion co-efficient is improved. Addition of pore former in the cathode slurry initiates large pores for better transport of reactants to the reaction site. For the NiO-GDC/GDC symmetric cells, thin layer of electrolyte offers very low value of polarization resistance. With respect to the total cell resistance, the contribution of anode is negligible. Long term study on the performance anode layer should be carried out to evaluate the ageing effect.

CHAPTER 8

Fabrication and characterization of single cells

8.1 Introduction

SOFC single cells can be fabricated in various configurations. The two basic configurations that have been widely used are tubular and planar. In each of these configurations, the cell can be anode supported, cathode supported or electrolyte supported. Anode supported planar SOFC has been widely documented in literature [238-241]. Higher power density is normally reported in anode supported planar design mainly due to lower internal resistance of the cell and better current collection. In anode supported planar configuration co-firing has been reported to be an economic route to integrate electrolyte and electrode. The interface formed by this route is reported to have reasonably low polarization resistance [239,241,242]. In general, co-firing approach is not suitable for fabricating cathode supported SOFC. The co-firing temperature is primarily decided by the sintering temperature of the electrolyte material. As reported in Chapter 3, GDC electrolyte prepared using combustion synthesized nano-powders could be sintered to its near theoretical density at 1250 ^{o}C. However, at this temperature the

147

chemical compatibility between cobaltite cathode and GDC electrolyte materials remains very poor [Ref. Chapter 6]. The chemical compatibility of NiO (precursor of Ni) and GDC at the sintering temperature is proven through the innumerable works published in the literature. Therefore, it is more practicable to fabricate a single cell by initially integrating NiO-GDC anode support with electrolyte by co-firing followed by forming the cathode layer by firing at a lower temperature.

Various ceramic processing techniques can be adopted to fabricate anode supported single cell. The anode support has been fabricated by different techniques, such as, doctor blade tape casting, pressing, coat mixing, gel casting and vacuum slip casting [240-247]. As a significant part of internal resistance of a cell comes from the electrolyte resistance, it is desirable to have a thin and impervious electrolyte layer in order to improve the performance of the cell. Fabrication of thin electrolyte film over electrode support can be achieved by various processes, namely, magnetron sputtering, screen printing, wet powder spraying, dip coating, plasma spraying, physical vapor deposition etc. [240,246-248]. Fabrication of both anode support and thin electrolyte layer by doctor blade co-casting has been reported in literature [249-253]. The electrolyte thickness in the half cells formed by this route typically remains in the range of 20 to 50 μm. Although the internal resistance of a cell increases with electrolyte thickness it has been reported that redox stability of the cell increases with increase in electrolyte thickness. Therefore, doctor blade co-casting route can be an attractive and economically viable approach in fabricating planar cell. In the present work anode supported half cells have been fabricated by two different approaches. In the first approach the anode support has been

fabricated by uniaxial pressing and the electrolyte layer has been integrated by brush painting using terpinol based slurry followed by co-firing. In the second approach doctor blade co-casting method has been adopted to fabricate anode supported half cell. The cathode layer has been formed over the dense GDC electrolyte layer by screen printing. Finally, the cells have been tested for their performance.

8.2 Experimental

8.2.1. Starting materials

NiO and 12 mol% GDC nano-powders both prepared by gel combustion route have been mixed in 1:1 weight ratio and used for fabrication of anode support. The gel combustion synthesized GDC powder has been used for making the electrolyte layer. Barium doped gadolinium cabaltite (GBC10) powder of composition $Gd_{0.9}Ba_{0.1}CoO_{3-\delta}$ prepared by solution polymerization method has been used as the cathode material.

8.2.2 Fabrication of anode supported half cell by uniaxial pressing

Anode composition was prepared by mixing NiO and GDC powders in weight ratio 1:1 through wet ball milling using stabilised zirconia balls, ethyl alcohol solvent and 1% polyvinyl butyral binder. The powder mixture was dried under an IR-lamp. The dry powder mixture was compacted uniaxially in a hydraulic press at 120 MPa pressure to get

NiO-GDC disc of 25 mm diameter × 2 mm thick (approximately). The density of the green compact was about 55% of theoretical density.

GDC ink was prepared by mixing GDC nano-powders and terpinol (solvent) in a Spex$^{(\circledR)}$ mill. A thin layer of GDC ink was applied on one side of NiO-GDC substrate by brush painting. After drying of the electrolyte slurry, the bi-layer was co-sintered at 1350 ^{o}C.

8.2.3 Fabrication of anode supported half cell by co-casting

8.2.3.1 Preparation of NiO-GDC slurry for tape casting

The tape casting slurry primarily consists of powder, solvent, dispersant, binder and plasticizer. For the preparation of anode slurry for tape casting, NiO and GDC powders were taken in 1:1 weight ratio. The slurry composition was optimised based on preliminary experiments. The formulation used in the preparation of the slurry in the present study is given in Table 8.1. Initially powders, solvent and dispersant were mixed in a ball mill for 12 h. Then the slurry was mixed with binder and plasticizers in the ball mill for 24 h for thorough mixing of all the ingredients.

8.2.3.2 Preparation of GDC slurry for tape casting

For the preparation of tape casting slurry of GDC, the powder was taken and mixed with other ingredients with quantity as given in Table 8.1. The mixing procedure remained same as mentioned above.

Table 8.1: Formulation used for the preparation of tape casting slurries

Ingredients		Quantity (wt.%) of ingredients for preparation of anode slurry	Quantity (wt.%) of ingredients for preparation of electrolyte slurry
Powder	Powder as mentioned	59 NiO-GDC (1:1)	50.4 GDC
Dispersant	Oleic acid	3.2	3.0
Solvent	Ethanol	17	21
	MEK	17	21
Plastisizer	PEG 400	0.6	0.6
Binder	PVB 90	3.2	3.0

8.2.3.3 Co-casting using doctors blade

Doctor blade co-casting approach was adopted in the fabrication of anode-electrolyte half cell in-planar configuration. In this approach, the second layer was cast over the first cast layer without removing it. The doctor blade tape casting machine (EPH, Engineering Associates INC, OREM, UTAH) used in the present study for making green tapes is shown in Fig. 8.1. The blade is moveable on a glass plate by a motor driven machine with controlled speed. A carrier film is generally used for easy removal of the green tape.
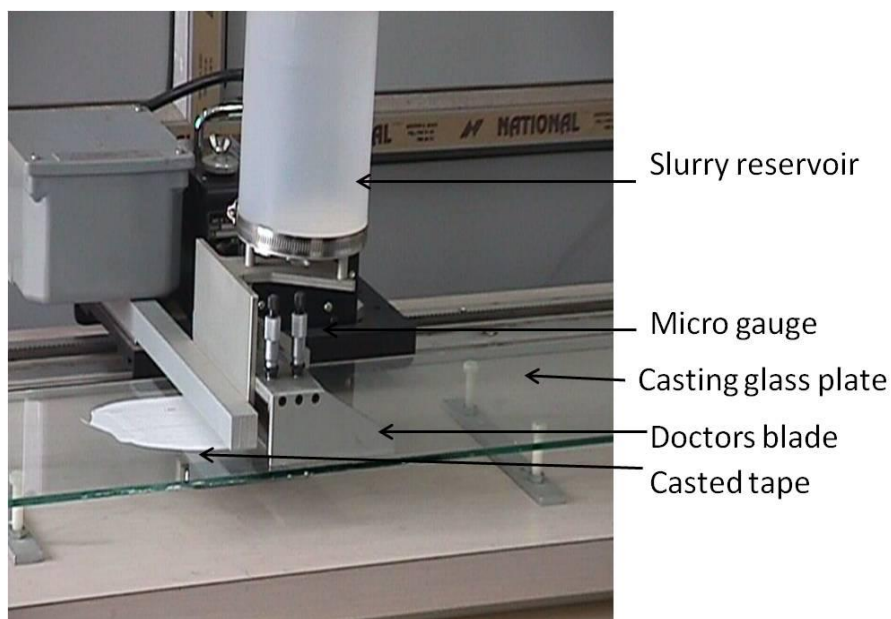
Fig. 8.1: Doctors' Blade tape casting machine

The slurry is poured in front of the doctor blade and the moving blade spreads the slurry over the carrier film. Silicon coated mylar carrier film was used in our experiments. Tape was cast on the side of the film that has lower wet-ability for the slurry i.e. silicon coated surface. The speed of the blade was adjusted to 40 cm/min in all the experiments. Thickness of the green tape was adjusted by suitably adjusting the blade gap through a screw gauge mounted over the casting head. Different blade gaps were used to get tapes of different thickness. It was observed that for good adhesion, the subsequent layer need to be cast in the time period of 1 to 2 minutes. For anode supported planar cell fabrication, tape of electrolyte was first cast on the mylar film. Thereafter, anode slurry was cast over the electrolyte layer. Green tapes were dried for more than 24 h at ambient temperature. Green tapes were punched to make discs of 25 mm dia.

8.2.3.4 Sintering of the tapes

The green bilayer tapes (in the form of circular disc of 25 mm dia.) were placed on a dense alumina plate. A porous alumina weight was placed over the green tapes and sintered at 1350 $^{\circ}$C, 6 h. A heating rate of 1°C / min. and a cooling rate 2 $^{\circ}$C / min. were used during sintering. About 20% shrinkage in the lateral direction was observed in most of the cases. The final diameters of the sintered half cells were measured to be within 20 to 21 mm.

8.2.4 Integration of anode supported half cell with cathode

GBC10-GDC composite was used as a cathode functional layer. For this, GBC10 and GDC powders were taken in 1:1 weight ratio and mixed with 5 wt.% carbon black as pore former. A terpineol based slurry of GBC10-GDC composite powder was prepared in a Spex mill$^{®}$. The slurry was coated over dense GDC electrolyte layer of the sintered NiO-GDC/GDC bilayer by screen printing. Over the GBC10-GDC composite layer a terpineol based slurry of GBC10 + 5 wt.% carbon black was coated by brush painting. The cathode layers were sintered by heating at 1100 $^{\circ}$C, 2 h in static air.

8.2.5 Performance testing of single cells

Single button cells of 20 mm dia were taken in the experiment. The active cathode area in these planar cells was about 2 cm^{2}. The performance testing of the cells were carried out

using Probostat^{TM} (NorECs, Norway) set up. The sample fixing assembly is shown in Fig. 8.2. The cells were fixed over an alumina tube with ceramic sealant (Aremco CeraBond 885).
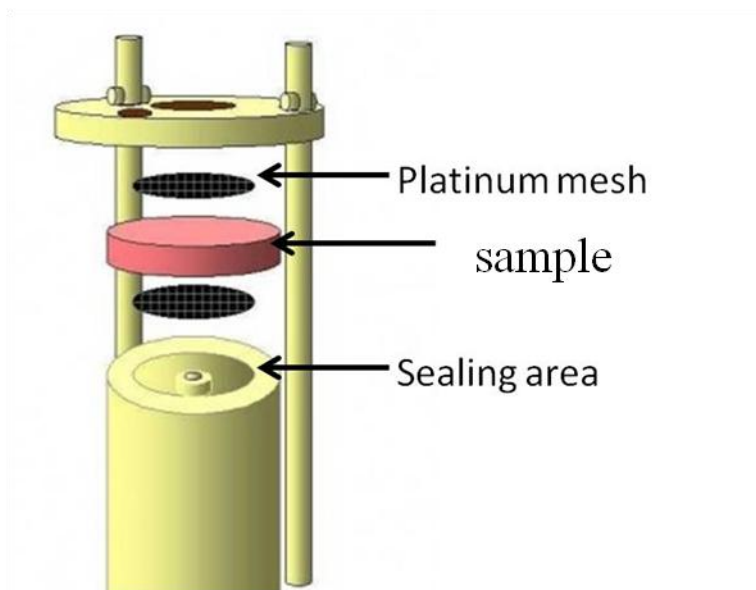
Fig. 8.2: Sample fixing assembly in the Probostat unit

The sealant was baked at desired temperature as mentioned by the supplier. Platinum mesh was used as current collector on the cathode side and nickel mesh on the anode side. About 2 cm^2 cathode area was used for current collection. On both the anode and cathode side electrical connections were made for current lead wire and voltage lead wire. A vertical tubular resistance heated furnace was used for maintaining the temperatures. Humidified hydrogen gas (composition: about 97% H$_2$ + 3% H$_2$O) was passed over anode side (inside alumina tube) and oxygen in the cathode side. The flow rates of the gases were suitably adjusted by rotameter. I-V characterization of the cells was carried out using electronic load and a nano-voltmeter. Current to voltage response

of the cells were recorded at 800 ^{o}C. The cell resistance (ohmic + interfacial polarization) was measured from the linear portion of the I-V curve. After the testing of the cells, the microstructures of the complete cells were observed in scanning electron microscope (Seron Technology, Korea).

8.3 Results and discussion

8.3.1 On the fabrication of anode supported half cell through doctor blade tape casting

The electrode and electrolyte thickness in the sintered half cell depend on the corresponding thicknesses in the green co-cast tape. The thickness of a green tape can be controlled by the blade gap (opening between the doctor blade and the cast surface). Table 8.2 shows the variation of thickness of the tape at different blade gap adjusted. Based on the results a blade gap of 200 μm was used for casting the electrolyte layer. Thereafter, anode layer was cast over the green electrolyte tape using a blade gap of 800 μm.

Table 8.2: Variation in the thickness of the tape in drying and at sintering stage for NiO-
GDC anode and GDC electrolyte tape

	Blade gap (µm)	Thickness of green tape (µm)	Thickness of the sintered tape (µm)
Anode	200	~70	50
	400	~160	110
	800	~450	360
Electrolyte	200	~90	70
	400	~230	190
	800	~580	460

.
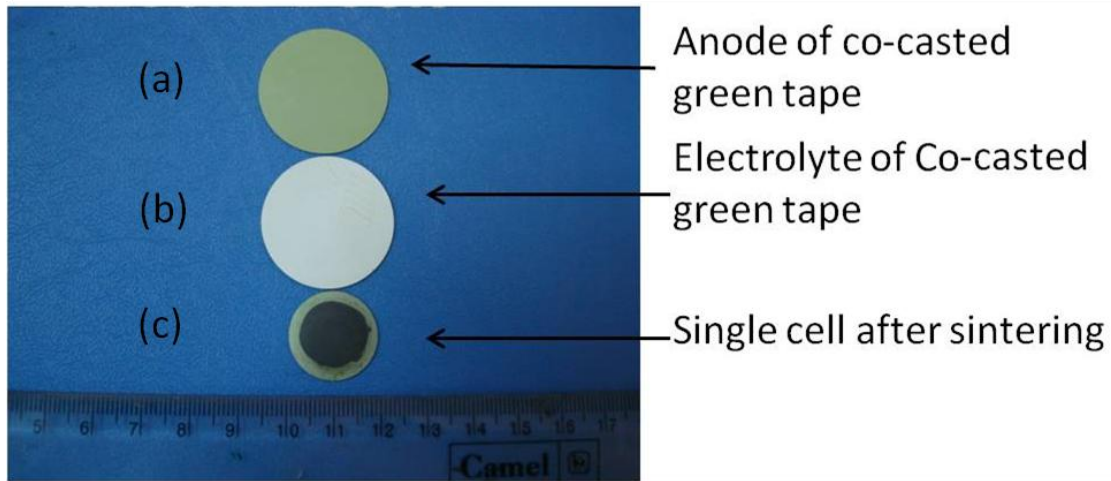
Fig. 8.3: Anode and electrolyte layer of green tape and sintered single cell

Fig. 8.3 (a-b) shows the photographs of the green bilayer tape. The NiO-GDC anode layer appears to be green in colour and the GDC electrolyte layer is off-white in colour. Fig. 8.3 (c) shows the photograph of a single cell obtained after co-firing the bilayer and subsequently integrating with cathode layers.

A lateral shrinkage of around 20% is observed in the sintered cell. In the sintered cell the electrolyte layer becomes transparent. Black cathode layer was applied over the electrolyte layer leaving a 2 mm wide rim at the periphery. The cell is fixed with the alumina tube of test assembly by applying glass sealing material along the rim of dense electrolyte.

Fig. 8.4 shows the SEM micrograph of anode-electrolyte half cell at low magnification. As shown in Fig. 8.4(a) the thickness of electrolyte and anode layers are about 50 μm and 400 μm, respectively. Good adherence is observed between the anode and electrolyte layers as seen in the SEM micrograph of Fig. 8.4(b). Fig. 8.5 (a) and (b) show the SEM micrographs of the sintered electrolyte and anode layers at higher magnification. Impervious electrolyte layer and porous anode layer is clearly visible in the micrographs.
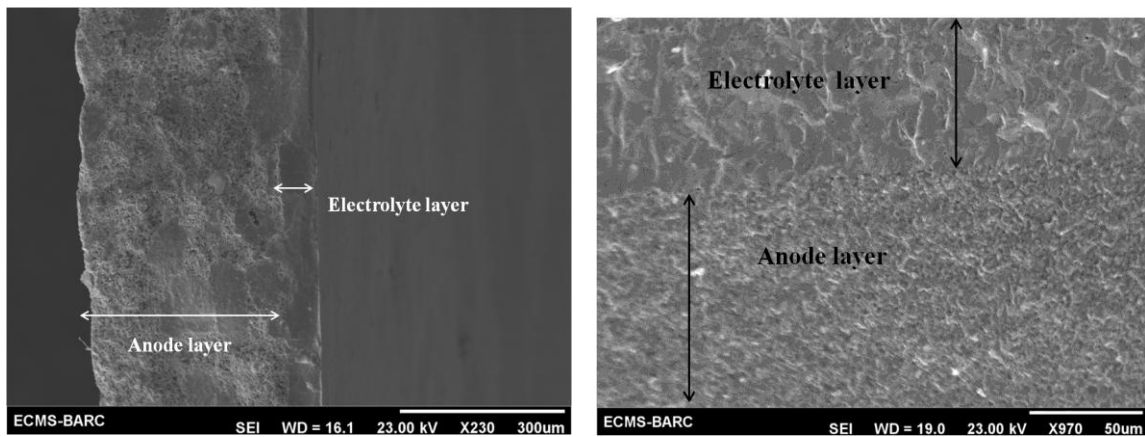
Fig. 8.4: SEM micrograph of anode-electrolyte half cell at low magnification; (a) 230 X, (b) 970 X.
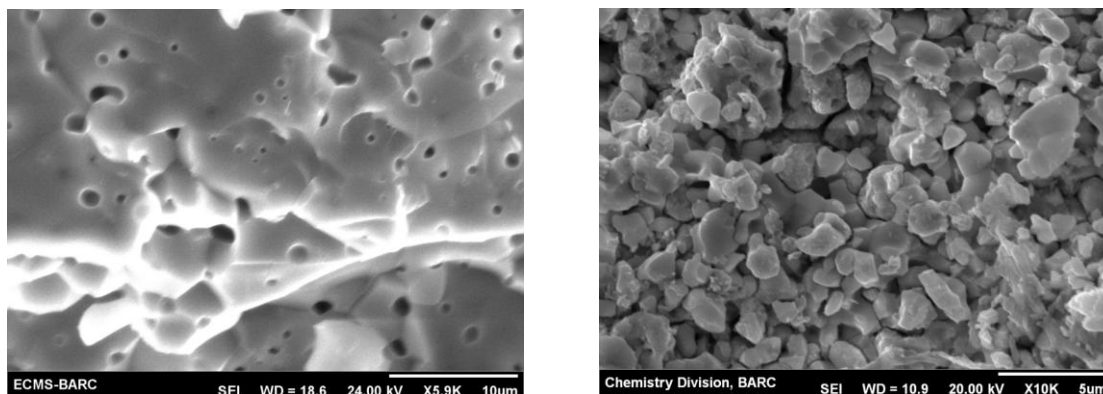
Fig. 8.5 SEM micrographs of (a) GDC electrolyte and (b) NiO-GDC anode of the sintered bilayer

8.3.2 I-V characteristics of anode supported cell prepared by uniaxial die pressing

The I-V characteristics of the cell prepared though die-pressing route is shown in Fig. 8.6. A maximum power density of 80 mW/cm^2 was obtained at 800 ^{o}C from this cell. The SEM micrograph of the cell after testing is shown in Fig. 8.7. Dense electrolyte of 70 – 90 μm thickness was observed in the microstructure. The non-uniformity in thickness is due to the defects generated during uniaxial pressing. The electrolyte layer has good adherence with both the cathode and anode layer. The lower value of power density of this cell may be due to deficiency in current collection.
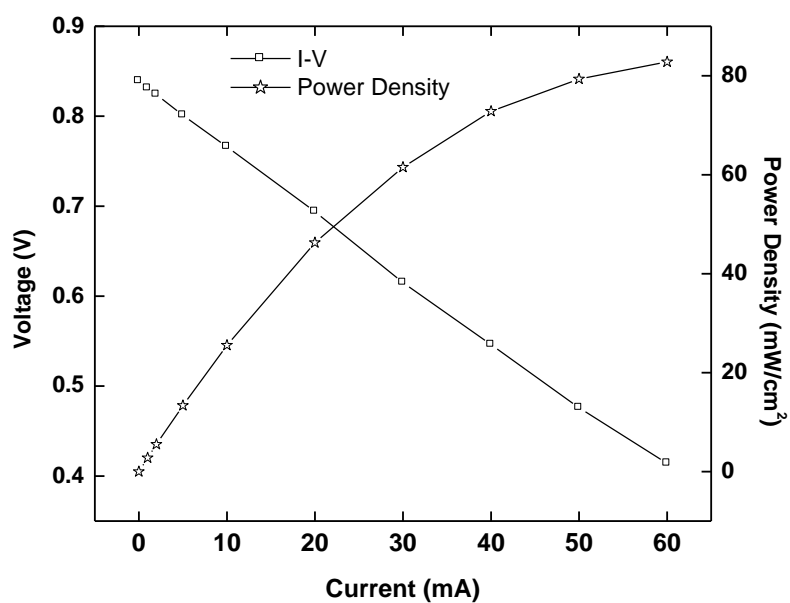
Fig. 8.6: I-V characteristics of single cell fabricated by tape casting
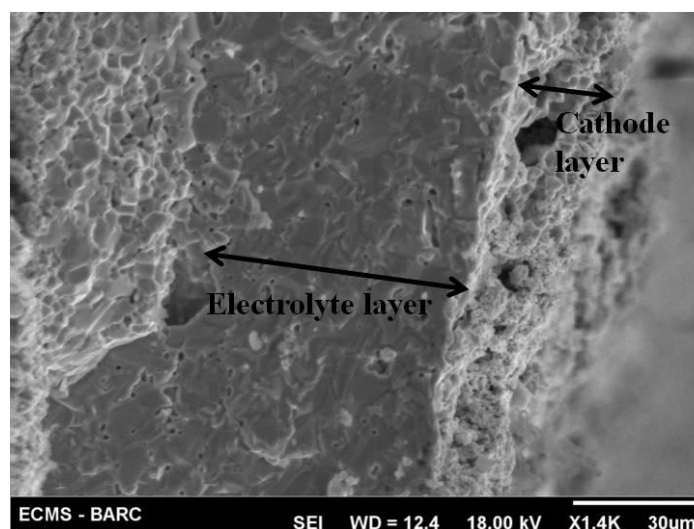
Fig. 8.7: SEM micrograph of single cell fabricated by die pressing (after cell testing)

8.3.2 I-V characteristics of anode supported cell prepared by tape casting

The I-V characteristics of the cell prepared by doctor blade tape casting method is shown in Figure 8.8. A maximum power density of 85 mW/cm^2 was obtained from this cell. Figure 8.9 shows the SEM micrograph of the cell after the cell testing. Dense electrolyte of uniform thickness (~50 µm) is observed in the microstructure. The electrolyte layer has good adherence with both the cathode and anode layer.
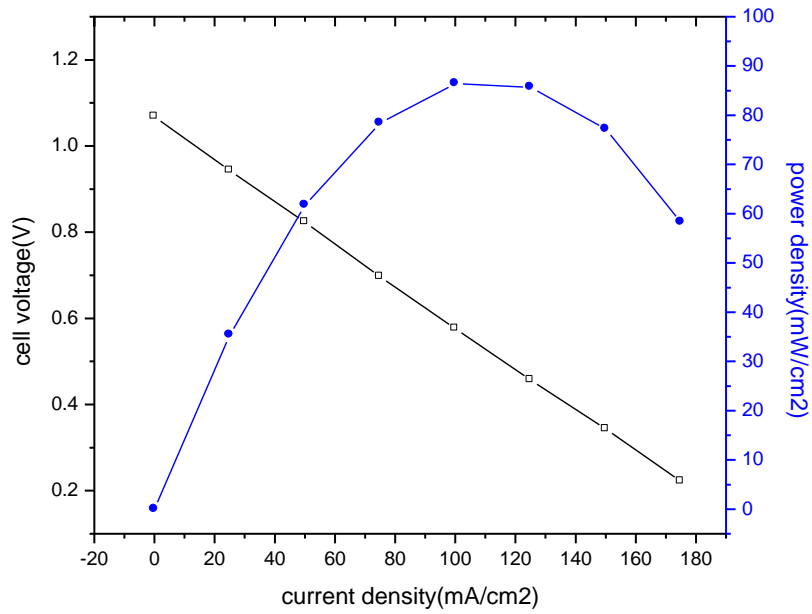
Fig 8.8: I-V curve of single cell fabricated by tape casting
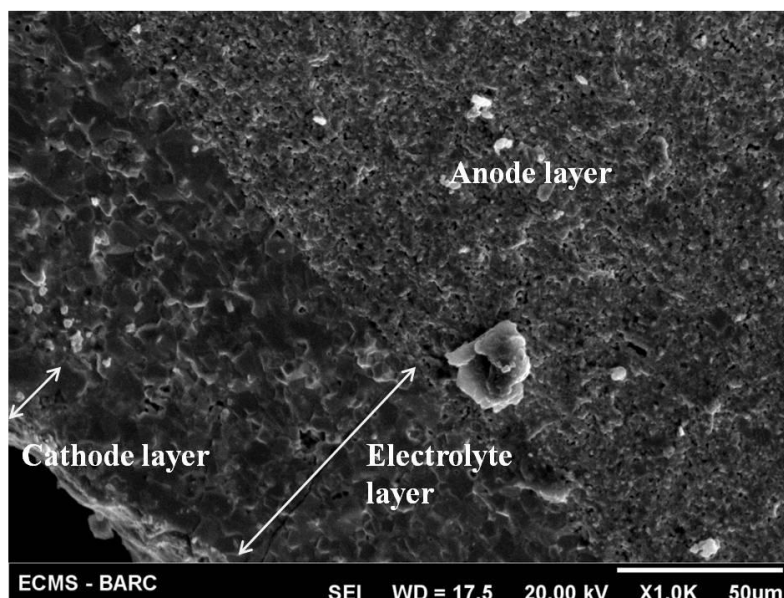
Fig. 8.9: SEM micrograph of single cell fabricated by tape casting (after cell testing)

8.4 Summary

Planar anode supported single cells have been formed by uniaxial die pressing and doctor blade co-casting method. Electrolyte thickness could be maintained in the range of 70 to 90 μm in case of pressing technique. Dense electrolyte layer of uniform thickness around 50 μm has been obtained by tape casting. Good adherence is obtained in the cells formed by both the techniques. The cells fabricated by pressing route and co-casting route delivered power @ 80 mW/cm^2 and 85 mW/cm^2 , respectively. As per calculation, using the data generated on electrolyte resistance and area specific interfacial polarisation resistance, the power density is expected to be much higher than the above values. The low power density in the present study is primarily due to the defficiency in current collection.

CHAPTER 9

Conclusions

Based on the work in the present thesis the following broad conclusions have been drawn.

- Phase pure and nano-crystalline GDC powder can be prepared through a single step gel combustion route using citric acid or glycine as fuel. When urea is used as fuel it forms weak complex with metal ions leading to instability in the gel and consequently formation of inhomogeneous precursor powder through incomplete combustion. In this case a calcination temperature of 700 ^{o}C is required for phase formation.

- Citric acid fuel gives optimum results in terms of preparation of fine nano-crystalline powder in narrow particle size distribution. The powders prepared using citric acid fuel could be sintered to near theoretical density at a temperature as low as 1200 ^{o}C. In view of this, GDC powders with different levels of gadolinia doping have been prepared through citric acid gel combustion route.

- Combustion temperature of GDC increases with gadolinia doping because of increase of heat of combustion. Agglomerated particle size increases with increase in gadolinia content attributed to higher reactivity of primary particle surface.

- In gadolinia-ceria system the sintering initiation temperature decreases with gadolinia content. Higher reactivity of primary particle surface lead to lower insertion temperature of sintering. However the final sintering temperature increases with gadolinia content. Because of the formation of hard agglomerates, shrinkage occurs over wider temperature range. Nevrtheless, GDC powders with different gadolinia content (in the range of 0 to 19%) could be sintered to near theoretical density ($> 96\%$) at 1250 $^{\circ}$C.

- Conductivity of GDC increases with increase in gadolinia substitution and reaches maximum at a level of 10-12 mol% Gd_2O_3. Further substitution leads to decrease in conductivity. The initial increase in conductivity with increase in gadolinia concentration is attributed to increase in oxygen vacancy concentration. However at higher level of gadolinia substitution vacancies get associated with dopant cations and lead to decrease in oxygen ion conductivity. Activation energy is found to be lowest for 10-12 mol% gadolinia doped ceria.

- Fine grained microstructure is developed in GDC electrolyte material when prepared through low temperature sintering of combustion synthesized powder. The grain boundary conductivity increases and bulk conductivity decreases as grain size becomes finer. At low temperature fine grained microstructure have higher conductivity; however conductivity increases with grain size at higher temperature region. Thus from technological point of view fine grained microstructure is preferable for application at lower temperatures.

- Phase pure and nano-crystalline NiO powder has been prepared through gel combustion route and calcining at 700 ^{o}C. NiO-GDC anode prepared by mixing combustion synthesized GDC and NiO powders followed by sintering at 1250 ^{o}C shows porous structure in which both GDC and NiO phases are networked. Ni-GDC cermet obtained by hydrogen reduction of NiO-GDC showed an electrical conductivity above 1200 S.cm^{-1} in the operating temperature regime and is stable over a long period. Hence, nano-structured NiO and GDC can form an anode with good stability over a long period.

- Very low interfacial polarization resistance was obtained for NiO-GDC/GDC symmetric cells with a thin electrolyte layer. ASR value as low as 0.06 ohm.cm^2 was obtained at 800 ^{0}C. With respect to the total cell resistance, the contribution of anode is negligible. Long study on the performance anode layer should be carried out to evaluate the ageing effect.

- Phase pure nanocrystalline gadolinium cobaltate (GdCoO$_3$) powder has been synthesized by solution polymerization method and subsequently calcining the derived precursor at 800 ^{o}C. Fine powders of gadolinium cobaltite can be sintered to near theoretical density by sintering at 1200 ^{o}C. Thermal expansion coefficient of GdCoO$_3$ is higher compared to GDC electrolyte material. However, using a composite of GDC and GdCoO$_3$, thermal expansion coefficient can be tuned to that of the electrolyte material. The area specific resistance of the interface between composite electrode and electrolyte material is reasonably low and the value can be

164

further brought down through optimization of process parameters. The results suggest that $GdCoO_3$ forms a candidate material for application as SOFC cathode material.

- Thermal expansion coefficient decreases with barium doping and matching TEC has been obtained with 10% Ba-doped gadolinium cobaltite. In the low temperature region electrical conductivity of $GdCoO_3$ increases significantly with barium addition. However, conductivity at higher temperature does not change much. Conductivity value more than 400 $S.cm^{-1}$ is obtained for pure and barium doped gadolinium cobaltite samples in the operating temperature region.

- Composite electrode prepared using 10% Ba-doped gadolinium cobaltite and GDC shows reasonably low area specific resistance (0.6 $ohm.cm^2$ at 900^oC). Addition of pore former further improves the electrode performance through micro modification of the pore structure enhancing better transport of reactants to the reaction site.

- Planar anode supported single cells with dense electrolyte layer of uniform thickness around 50 µm has been obtained by doctor blade co-casting method. Cocasting of anode and electrolyte layer followed by co-sintering of both layers was used for fabrication of aode supported cells. Maximum power density of 85 mW/cm^2 was obtained for such type of cells. From the property measuremet of individual components, a high value of power density is expected, however the observed low power density in the present study is primarily due to the defficiency in current collection.

Future Scope

- Evaluation of oxygen ion conductivity of GDC electrolyte in reducing environment

- Long term performance evaluation of Ni-GDC anode and optimization of microstructure through better ceramic processing.

- Long term performance evaluation of $Gd_{0.9}Ba_{0.1}CoO_3$ cathode and optimization of microstructure.

- Performance evaluation of single cell after sealing and current collection.

REFERENCES

1. REN21 (2011) Renewables 2011: Global Status Report, p. 17, 18.

2. W. Vielstich, H. A. Gasteiger, A. Lamm (Editors), Hand book of fuel cells, Fundamentals, Technology and applications, John Wally & sons Chichester, England, 2003, ISBN 0-471-49926-9.

3. B. Debaer, PhD Thesis, University of Twente, The Netherlands.

4. W. R Grove, Phis. Mag. 14 (1839) 127.

5. A. J. Appleby, Fuel Cell Hand Book (1989) New York : Van Nostrand Reinhold

6. M. Juhl, S. Primdahl C. Manon and, M. Mogenson, J. Power Sources 61 (1996) 173.

7. M.Brown, S. Primdahl and M.Mogenson, J. Electrochem. Soc. 147 (2000) 475.

8. G.A.Tompsett, C.Finnerty, K.Kendall, T.Alston, and N.M. Sammes, J. Power Sources 86 (2000) 376.

9. M. Dokiya, Solid State Ionics 152 (2002) 383.

10. S. P. S. Badwal, K. Foger, Ceram. Int. 22 (1996) 257.

11. J.F. Baumard, P. Abelard, Advances in Ceramics: Edited by N. Claussen, M. Rűhle, A. Heuer, American Ceramic Society, Columbus, OH, 12 (1984) 555.

12. C.B. Choudhary, H.S. Maiti, E.C. Subbarao, in Solid Electrolytes and Their Applications, Edited by E.C. Subbarao, Plenum Press, New York, (1980) 1.

13. R. Ran, X. Wu, C. Quan, D. Weng, Solid State Ionics 176 (2005) 965.

14. M. Ellouze, W. Boujelben, A. Cheikhrouhou, H. Fuess, R. Madar, J. Alloys Compd. 352 (2003) 41.

15. F. Ishizaki, T. Yoshida, S. Sakurada, Proc. 1st Int. Symp. On Solid Oxide Fuel Cells, The Electrochemical Society, Pennington, NJ (1989)p. 3.

16. H. L. Tuller, A. S. Nowick, J. Electrochem. Soc. 122 (1975) 255.

17. T. Takahashi, H. Iwahara, J. Appl. Electrochem. 3 (1973) 65.

18. K. Hu, C. Chen, D. Peng, G. Meng, Solid State Ionics 28 (1988) 566.

19. T. Takahashi, H. Iwahara, Y. Nagai, J. Appl. Electrochem. 2 (1972) 97.

20. M. J. Verkerk, K. Keizer , A. J. Burggraaf, J. Appl. Electrochem. 10 (1980) 81.

21. J. Miyayama, T. Nishi, H. Yanagida, J. Mater. Sci. 22 (1987) 2624.

22. T. Takahashi, T. Esaka, H. Iwahara, J. Appl. Electrochem. 7 (1977) 303.

23. L. Brixner, J. Am. Chem. Soc. 80 (1958) 3214.

24. F. K. Patterson, C. W. Moeller, R. Ward, Inorg. Chem. 2 (1963) 196.

25. F. Forrat, G. Dauge, P. Trevoux, G. Danner, M. Christen, C. R. Acad. Sci. Paris 259 (1964) 2813.

26. R. V. Coates, J. Appl. Chem. 14 (1964) 346.

27. T. Takahashi, H. Iwahara, Energy Convers. 11 (1971) 105.

28. J. A. Kilner, P. Barrow, R. J. Brook, M. J. Norgett, J. Power Sources 3 (1978) 67.

29. T. Takahashi, H. Iwahara, in Research in Effective Use of Energy, sp. publ. of the Ministry of Education Science and Culture of Japan 3 (1982) 727.

30. A. F. Sammells, R. L. Cook, W. L. Worrell, Rep. No. GRI-YO/O136, Gas Research Institute, Chicago, IL, (1990).

31. R. L. Cook, R. C. MacDuff, A. F. Sammells, J. Electrochem. Soc. 137 (1990) 3309.

32. B. C. H. Steele, A. Heinzel, Nature 414 (2001) 345.

33. F. P. F. van Berkel, F. H. van Heuveln, J. P. P. Huijsmans, Solid State Ionics 72 (1994) 240.

34. U. Anselmi-Tamburini, G. Chiodelli, M. Arimondi, F. Maglia, G. Spinolo, Z. A. Munir, Solid State Ionics 110 (1998) 35.

35. T. H. Etsell, S. N. Flengas, Chem. Rev. 70 (1970) 339.

36. V. N. Chebotin, M. V. Perfiliev, Electrochemistry of solid electrolytes (1978) Technical Information Center, US Department of Energy, Oak Ridge.

37. B. Dalslet, P. Blennow, P. V. Hendriksen, N. Bonanos, D. Lybye, M. Mogensen, J. Solid State Electrochem. 10 (2006) 547.

38. E. V. Tsipis, V. V. Kharton, J. R. Frade, J. Eur. Ceram. Soc. 25 (2005) 2623.

39. J. B. Goodenough, Y-H Huang, J. Power Sources 173 (2007) 1.

40. S. Tao, J. T. S. Irvine, J. Electrochem. Soc. 151 (2004) A252.

41. J. Liu, B. Madsen, Z. Ji, S. Barnett, Electrochem. Solid State Lett 5 (2002) A122.

42. Y-H Huang, R. I. Dass, J.C. Denyszyn, J. B. Goodenough, J. Electrochem. Soc. 153 (2006) A1266.

43. N. Q. Minh, T. Takahashi (1995) Science and technology of ceramic fuel cells. Elsevier, Amsterdam.

44. S. C. Singhal, Mater. Res. Soc. Bull. 25 (2000) 16.

45. O. Yamamoto, Electrochim. Acta 45 (2000) 2423.

46. B. C. H. Steele, J. Mater. Sci. 36 (2001) 1053.

47. J. P. P. Huijsmans, Curr. Opin. Solid State Mat. Sci. 5 (2001) 317.

48. S. F. Palguev, V. K. Gilderman, V. I. Zemtsov (1990) High-temperature oxide electronic conductors for electrochemical devices. Nauka, Moscow.

49. V. V. Kharton, E. N. Naumovich, A. A. Vecher, J. Solid State Electrochem. 3 (1999) 61.

50. R. J. Gorte, AIChE J. 51 (2005) 2377.

51. F. De Bruijn, Green Chem. 7 (2005) 132.

52. K. Kendall, Int. Mater. Rev. 50 (2005) 257.

53. C. Sun, U. Stimming, J. Power Sources 171 (2007) 247.

54. S. B. Adler, Chem. Rev. 104 (2004) 4791.

55. L. Blum, W. A. Meulenberg, H. Nabielek, R. Steinberger-Wilckens, Int. J. Appl. Ceram. Technol 2 (2005) 482.

56. V. V. Kharton, A. A. Yaremchenko, E. N. Naumovich, J. Solid State electrochem. 3 (1999) 303.

57. Y. S. Gaiduk, V. V. Kharton, E. N. Naumovich, A. V. Nikolaev, V. V. Samokhval, Inorg. Mater. 30 (1994) 1360.

58. Y. Takeda, H. Y. Tu, H. Sakaki, S. Watanabe, N. Imanishi, O. Yamamoto, M. B. Phillipps, N. M. Sammes, J. Electrochem. Soc. 144 (1997) 2810.

59. Y. Takeda, Y. Sakaki, T. Ichikawa, N. Imanishi, O. Yamamoto, M. Mori, T. Abe, Solid State Ionics 72 (1994) 257.

60. S. P. Jiang, J. Solid State Electrochem. 11 (2007) 93.

61. E. Siebert, A. Hammouche, M. Kleitz, Electrochim. Acta 40 (1995) 1741.

62. H. Y. Lee, W. S. Cho, S. M. Oh, H-D Wiemhöfer, W. Göpel, J. Electrochem. Soc. 142 (1995) 2659.

63. K. Yasumoto, N. Mori, J. Mizusaki, H. Tagawa, M. Dokiya, J. Electrochem. Soc. 148 (2001) A105.

64. Y. Sakaki, Y. Takeda, A. Kato, N. Imanishi, O. Yamamoto, M. Hattori, M. Iio, Y. Esaki, Solid State Ionics 118 (1999) 187.

65. T. Ishihara, T. Kudo, H. Matsuda, Y. Takita, J. Electrochem. Soc. 142 (1995) 1519.

66. H-R Rim, S-K Jeung, E. Jung, J-S Lee, Mater. Chem. Phys. 52 (1998) 54.

67. A. J. McEvoy, S. Rambert, S. Widmer (1996), In: Thorstensen, B (eds) Proc 2nd Eur Solid Oxide Fuel Cell Forum (Oslo, May 1996). vol. 1. European SOFC Forum, Oberrohrdorf, Switzerland, pp 599.

68. J. A. M. van Roosmalen, E. H. P. Cordfunke, Solid State Ionics 52 (1992) 303.

69. F. H. van Heuveln, H. J. M. Bouwmeester, J. Electrochem. Soc. 144 (1997) 134.

70. H. Kamata, A. Hosaka, J. Mizusaki, H. Tagawa, Solid State Ionics 106 (1998) 237.

71. V. N. Tikhonovich, V. V. Kharton, V. V. Samokhval , A. V. Kovalevsky, Solid State Ionics 93 (1997) 95.

72. Y. Takeda, R. Kanno, M. Noda, Y. Tomida, O. Yamamoto, J. Electrochem. Soc. 134 (1987) 2656.

73. M. A. Pena, J. L. G. Fierro, Chem. Rev. 101 (2001) 1981.

74. J. Holc, D. Kuščer, M. Hrovat, S. Bernik, D. Kolar, Solid State Ionics 95 (1997) 259.

75. M. B. Phillipps, N. M. Sammes, O. Yamamoto, Solid State Ionics 123 (1999) 131.

76. I. P. Marozau, V. V. Kharton, A. P. Viskup, J. R. Frade, V. V. Samakhval, J. Eur. Ceram. Soc. 26 (2006) 1371.

77. X. D. Zhou, H. U. Anderson, SOFC-IX: solid oxide fuel cells IX, Electrochemical Society proceedings, Quebec PQ, Canada, (2005) pp 1479.

78. V. V. Kharton, A. A. Yaremchenko, A. L. Shaula, A. P. Viskup, F. M. B. Marques, J. R. Frade, E. N. Naumovich, J. R. Casanova, I. P. Marozau, Defect Diffus. Forum 226 (2004) 141.

79. H. L. Lein, K. Wiik, T. Grande, Solid State Ionics 177 (2006) 1795.

80. M. Søgaard, P. V. Hendriksen, M. Mogensen, J. Solid State Chem. 180 (2007) 1489

81. W. Zajac, K. Swierczek, J. Molenda, J. Power Sources 173 (2007) 675.

82. V. V. Kharton, A. A. Yaremchenko, M. V. Patrakeev, E. N. Naumovich, F. M. B. Marques, J. Eur. Ceram. Soc. 23 (2003) 1417.

83. J. M. Ralph, C. Rossignol, R. Kumar, J. Electrochem. Soc. 150 (2003) A1518.

84. S. P. Simner, J. F. Bonnett, N. L. Canfield , K. D. Meinhardt, V. L. Sprenkle , J. W. Stevenson, Electrochem. Solid-state Lett. 5 (2002) A173.

85. G. Coffey, J. Hardy, O. Marina, L. Pederson, P. Rieke, E. Thomsen, Solid State Ionics 175 (2004) 73.

86. H. J.M. Bouwmeester, A. J. Burgraaf (1996) In: A. J. Burggraaf, L. Cot, (eds) Fundamentals of inorganic membrane science and technology. Elsevier, Amsterdam, pp 435.

87. M. Al Daroukh, V. V. Vashook, H. Ullmann, F. Tietz, I. Arual Raj, Solid State Ionics 158 (2003) 141.

88. H. Ullmann, N. Trofimenko, F. Tietz, D. Stöver, A. Ahmad-Khanlou, Solid State Ionics 138 (2000) 79.

89. G. C. Kostogloudis, C. Ftikos, A. Ahmad-Khanlou, A. Naoumidis, D. Stöver, Solid State Ionics 134 (2000) 127.

90. J. W. Stevenson, T. R. Armstrong, R. D. Carneim, L. R. Pederson, W. J. Weber, J. Electrochem. Soc. 143 (1996) 2722.

91. A. N. Petrov, V. A. Cherepanov, A. Yu. Zuev, J. Solid State Electrochem. 10 (2006) 517.

92. K. Huang, H. Y. Lee, J. B. Goodenough, J. Electrochem. Soc. 145 (1998) 3220.

93. Y. Takeda, H. Ueno, N. Imanishi, O. Yamamoto, N. Sammes, M. B. Phillipps, Solid State Ionics 86 (1996) 1187.

94. H. Y. Lee, S. M. Oh, I. Y. Seo, F. Rocholl, H. D. Wiemhöfer (1997) In: U. Stimming, S. C. Singhal, H. Tagawa, W. Lehnert (eds) SOFC V. The Electrochemical Society, Pennington, NJ, pp 520.

95. E. N. Naumovich, V. V. Kharton, V. V. Samokhval, A. V. Kovalevsky, Solid State Ionics 93 (1997) 95.

96. T. Ishihara, M. Honda, T. Shibayama, H. Furutani, Y. Takita, Ionics 4 (1998) 395.

97. F. Chen, C. Xia, M. Liu, Chem. Lett. 30 (2001) 1032.

98. H. Uchida, S. Arisaka, M. Watanabe, J. Electrochem. Soc. 149 (2002) A13.

99. S. Uhlenbruck, F. Tietz Mater. Sci. Eng. B 107 (2004) 277.

100. E. Lust, P. Möller, I. Kivi, G. Nurk, S. Kallip, J. Solid State Electrochem. 9 (2005) 882.

101. V. V. Kharton, E. V. Tsipis, A. A. Yaremchenko, I. P. Marozau, A. P. Viskup, J. R. Frade, E. N. Naumovich, Mater. Sci. Eng. B 134 (2006) 80.

102. F. Morin, G. Trudel, Y. Denos, Solid State Ionics 96 (1997) 129.

103. S. K. Poznyak, V. V. Kharton, J. R. Frade, A. A. Yaremchenko, E. V. Tsipis, S. O. Yakovlev, I. P. Marozau, J. Solid State Electrochem. 12 (2008) 15.

104. E. V. Tsipis, V. V. Kharton, J. R. Frade, P. Nunez, J. Solid State Electrochem. 9 (2005) 547.

105. T. Ishihara, S. Fukui, H. Nishiguchi, Y. Takita, Solid State Ionics 152 (2002) 609.

106. F. S. Baumann, J. Fleig, G. Cristiani, B. Stuhlhofer, H-U Habermeier, J. Maier, J. Electrochem. Soc. 154 (2007) B931.

107. J. Peña-Martinez, D. Marrero-Lopez, D. Perez-Coll, J. C. Ruiz-Morales, P. Nuñez, Electrochim Acta 52 (2007) 2950.

108. K. Huang, H. Y. Lee, J. B. Goodenough, J. Electrochem. Soc. 145 (1998) 3220.

109. K. T. Lee, A. Manthiram, J. Electrochem. Soc. 153 (2006) A794.

110. K. Yasumoto, Y. Inagaki, M. Shiono, M. Dokiya, Solid State Ionics 148 (2002) 545.

111. T. Ishihara, T. Kudo, H. Matsuda, Y. Takita, J. Electrochem. Soc. 142 (1995) 1519.

112. C. J. Zhu, X. M. Liu, D. Xu, D. T. Yan, D. Y. Wang, W. H. Su, Solid State Ionics 179 (2008) 1470.

113. W. X. Chen, T. L. Wen, H. W. Nie, R. Zheng, Mater. Res. Bull. 38 (2003) 1319.

114. G. C. Kostgloudis, G. Tsiniarakis, C. Ftikos, Solid State Ionics 135(2000) 529.

115. V. Dusastre, J. A. Kilner, Solid State Ionics 126 (1999) 163.

116. B. C. H. Steele, Solid State Ionics 86–88 (1996) 1223.

117. L. Kindermann, D. Dos, H. Nickel, K. Hilpert, C. C. Appel, F. W. Poulsan, J. Electrochem. Soc. 144 (1997) 717.

118. B. C. H. Steele Solid State Ionics 129 (2000) 95.

119. X. W. Meng, S. Q. Lv, Y. Ji, W. Tao, Y. L. Zhang, J. Power Sources 183 (2008) 581.

120. Z. P. Shao, S. M. Haile, Nature 431 (2004) 170.

121. A. Y. Yan, M. J. Cheng, Y. L. Dong, W. S. Yang, V. Maragou, S. Q. Song, P. Tsiakaras, Appl. Catal. B 66 (2006) 64.

122. R. Chiba, F. Yoshimura, Y. Sakurai, Solid State Ionics 124 (1999) 281.

123. H. Orui, K. Watanabe, R. Chiba, M. Arakawa, J. Electrochem Soc 151 (2004) A1412.

124. A. Endo, S. Wada, C. J. Wen, H. Komiyama, K. Yamada, J. Electrochem. Soc. 145 (1998) L35

125. C. W. Tanner, K. Z. Fung, A. V. Virkar, J. Electrochem. Soc. 144 (1997) 21

126. Y. Liu, S. W. Jha, M. L. Liu, Adv. Mater. 16 (2004) 256.

127. M. Mamak, G. S. Metraux, S. Petrov, N. Coombs, G. A. Ozin, M. A. Green, J. Am. Chem. Soc. 125 (2003) 5161.

128. Y. J. Leng, S. H. Chan, Q. L. Liu, Int. J. Hydro. Energy 33 (2008) 3808.

129. C. W. Sun, Z. Xie, C. R. Xia, H. Li, L. Q. Chen, Electrochem. Commun. 8 (2006) 833.

130. T. Fukui, K. Murata, S. Ohara, H. Abe, M. Naito, K. Nogi, J. Power Sources 125 (2004) 17.

131. H. Abe, K. Murata, T. Fukui, W. J. Moon, K. Kaneko, M. Naito, Thin Solid Films 496 (2006) 49.

132. M. Antonietti, G. A. Ozin, Chem. Eur. J 10 (2004) 28.

133. T. Z. Sholklapper, H. Kurokawa, C. P. Jacobson, S. J. Visco, L. C. De Jonghe, Nano Lett 7 (2007) 2136.

134. Y. Huang, J. M. Vohs, R. J. Gorte, J. Electrochem. Soc. 153 (2006) A951.

135. A. Barbucci, M. Viviani, M. Panizza, M. Delucchi, G. Cerisola, J. Appl. Electrochem. 35 (2005) 399.

136. Y. J. Leng, S. H. Chan, K. A. Khor, S. P. Jiang, J. Solid State Electrochem. 10 (2006) 339.

137. G. S. Godoi, D. P. F. de Souza, Mater. Sci. Eng. B 140 (2007) 90.

138. K. Chen, Z. Lu, N. Ai, X. Chen, J. Hu, X. Huang, W. Su, J. Power Sources 167 (2007) 84.

139. J-H Kim, R-H Song, J. H. Kim, T-H Lim, Y-K Sun, D-R Shin, J. Solid State Electrochem. 11 (2007) 1385.

140. A. Hagiwara, N. Hobara, K. Takizawa, K. Sato, H. Abe, M. Naito, Solid State Ionics 178 (2007) 1123.

141. C. Laberty, F. Zhao, K. E. Swider-Lyons, A. V. Virkar, Electrochem. Solid State Lett. 10 (2007) B170.

142. E. P. Murray, S. A. Barnett, Solid State Ionics 143 (2001) 265.

143. H. Zhao, L. Huo, S. Gao, J. Power Sources 125 (2004) 149.

144. C. Xia, W. Rauch, F. Chen, M. Liu, Solid State Ionics 149(2002) 11.

145. N. T. Hart, N. P. Brandon, M. J. Day, N. Lapena-Rey, J. Power Sources 106 (2002) 42.

146. K. Imahara, C. P. Jacobson, S. J. Visco, L. C. De Jonghe, Solid State Ionics 176 (2005) 451.

147. S. P. Jiang, Mater. Sci. Eng. A 418 (2006) 199.

148. W. Wang, M. D. Gross, J. M. Vohs, R. J. Gorte, J. Electrochem. Soc. 154 (2007) B439.

149. N. Q. Minh, J. Am. Ceram. Soc. 76 (1993) 563.

150. N.B. Kirk, J.V. Wood, J. Mater. Sci., 30 (1995) 2171.

151. Y. Zhou, M.N. Rahman, Acta. Mater., 45 (1997) 3635.

152. S. Zha, C. Xia, G. Meng, J. Power Source, 115 (2003) 44.

153. S. Torrens, N.M. Sammes, G. A. Tompsett, Solid State Ionics, 111 (1998) 9.

154. M. Hirano, E. Kato, J. Am. Ceram. Soc., 82 (1999) 2861.

155. B. Xia, I.W. Lenggoro, Okuyama, J. Mater. Chem., 11(2001) 2925.

156. R. D. Purohit, B. P. Sharma, K. T. Pillai, A. K. Tyagi, Mater. Res. Bull., 36 (2001) 2711.

157. S.R. Jain, K.C. Adiga, V.R. Pai Venekar, Combustion Flame, 40 (1981) 71.

158. L.A. Chick, L.R. Pederson, G.D. Maupin, J.L. Bates, L.E. Thomas, G.J. Exarhos, Mater. Lett., 10 (1990) 6.

159. H. Inaba and H. Tagawa, Solid State Ionics 83 (1996) 1.

160. S.C. Singhal and K. Kendall, High Temperature Solid Oxide Fuel Cells: Fundamentals, Design and Applications, Elsevier, Oxford, UK, 2003, p.92.

161. M. Aoki, Y.-M. Chiang, I. Kosacki, L. J.-R. Lee, H. Tuller and Y. Liu, J. Am. Ceram. Soc. 79 (1996) 1169.

162. M.J. Verkerk, B.J. Middelhuis and A.J. Burggraaf, Solid State Ionics 6 (1982) 159.

163. X. Guo, Solid State Ionics 81 (1995) 235.

164. X.J. Chen, K.A. Khor, S.H. Chan and L.G. Yu, Mater. Sci. Eng. A 341 (2003) 43.

165. X.J. Chen, K.A. Khor, S.H. Chan, et al., Mater. Sci. Eng. A 374 (2004) 64.

166. S.P.S. Badwal, Solid State Ionics 52 (1992) 23.

167. S.P.S. Badwal, F.T. Ciacchi, S. Rajendran, J. Drennan, Solid State Ionics 109 (1998) 167.

168. P. Mondal, A. Klein, W. Jaegermann, H. Hahn, Solid State Ionics 118 (1999) 331.

169. X.D. Zhou, W. Huebner, I. Kosacki and H. U. Anderson, J. Am. Ceram. Soc. 85 (2002) 1757.

170. G.M. Christie and F.P.F. van Berkel, Solid State Ionics 83 (1996) 17.

171. Y.-M. Chiang, E.B. Lavik and D.A. Blom, Nanostructured Materials 9 (1997) 633.

172. T. Suzuki, I. Kosacki and H.U. Anderson, Solid State Ionics 151 (2001) 111.

173. N. Sata, K, Eberman, K. Eberl and J. Maier, Nature 408 (2000) 946.

174. I. Kosacki, H.U. Anderson, Y. Mizutani and K. Ukai, Solid State Ionics 152 (2002) 431.

175. J. Rupp and L. Gauckler, Solid State Ionics 177 (2006) 2513.

176. M.G. Bellino, D.G. Lamas, and N.E. Walsoi de Reca, Adv. Functional Materials 16 (2006) 107.

177. T. Mahata, G. Das, R. K. Mishra and B.P. Sharma, Journal of Alloys and Compounds 391 (2005) 129.

178. R.K. Lenka, T. Mahata, P.K. Sinha, and B.P. Sharma, J. Am. Ceram. Soc. 89 (2006) 3871.

179. E. Barsoukov and J.R. Macdonald, Impedance Spectoscopy, Theory, Practice and Applications, Wiley Interscience, New Jarsey, 2005.

180. J Luo, E F Hairetdinov, D P Almond and R Stevens, Solid State Ionics 122 (1999) 205.

181. J. A. Kilner, B C H Steele, in O.Toft Sorensen (Ed), Nonstoichiometric Oxides, Academic Press, 1981, p233

182. A S Nowick, D S Park, in G Mahan, W Roth (Eds) Super Ionic Conductors, Plenum Press, 1976, p-395

183. Hugo J Avila-Paredes, Kwanghoon Choi, Chien-Ting Chen and Sangtae Kim, J. Mater. Chem, 19 (2009) 4837.

184. Y. J. Leng, S. H. Chan, S. P. Jiang, K. A. Khor, Solid State Ionics 170(2004) 9.

185. J. W. Kim, A. V. Virkar, K. Z. Fung, K. Mehta, S. C. Singhal, J. Electrochem. Soc. 146(1999)69.

186. Y. J. Leng, S. H. Chan, K. A. Khor, S. P. Jiang, Int. J. Hyd. Energy 29 (2004) 1025.

187. Q. L. Liu, K. A. Khor, S. H. Chan, J. Power Sources 161 (2006) 123.

188. X. S. Xin, Z. Lu, X. Q. Huang, X. Q. Sha, Y. H. Zhang, W. H. Su, J. Power Sources 159 (2006) 1158.

189. X. Y. Xu, C. G. Xia, S.G. Huang, D. K. Peng, Ceram. Int. 31 (2006) 1061.

190. Y. Y. Chen, W .C .J. Wei, Solid State Ionics 177 (2006) 351.

191. X. S. Xin, Z. L˙u, X. Q. Huang, X. Q. Sha, Y. H. Zhang, K. F. Chen, N. Ai, R. B. Zhu, W. H. Su, J. Power Sources 160 (2006) 1221.

192. L. Jia, Z. L¨u, X. Q. Huang, Z. G. Liu, K. F. Chen, X. Q. Sha, G. Q. Li, W. H. Su, J. Alloys Compd. 424 (2006) 299.

193. M. G. Chourashiya, L. D. Jadhav, Int. J. Hyd. Energy 36 (2011) 14984.

194. C. Fu, S. H. Chan, Q. Liu, X. Ge, G. Pasciakjg, Int. J. Hyd. Energy 35 (2010) 301.

195. A. U. Chavan, L. D. Jadhav, A. P. Jamale, S. P. Patil, C. H. Bhosale, S. R. Bharadwaj, P. S. Patil, Ceram. Int. 38 (2012) 3191.

196. V. Gil, J. Tartaj, C. Moure, Ceram. Int. 35 (2009) 839.

197. D. Y. Han, H. Y. Yang, C. B. Shen, X. Zhou, F. H. Wang, Powder Technology 147 (2004) 113.

198. H. Mohebbi, T. Ebadzadeh, F. A. Hesari, J. Power Sources 178 (2008) 64.

199. D. Ai, X. Dai, Q. Li, C. Deng, S. Kang, China Particuology 2 (2004) 157.

200. C. Ding, T. Hashida, Int. J. Hyd. Energy 36 (2011) 5567.

201. H. Inaba and H. Tagawa, Solid State Ionics 83 (1996) 1.

202. S.J. Skinner, Int. J. Inorg. Mater. 3 (2001) 113.

203. K.C. Wincewicz, J.S. Cooper, J. Power Sources 140 (2005) 280.

204. E.V. Tsipis, V.V. Kharton, J. Solid State Electrochem. 12 (2008) 1367.

205. C. Sun, R. Hui, J. Roller, J. Solid State Electrochem. 14 (2010) 1125.

206. H. Ullmann, N. Trofimenko, F. Tiez, D. Stover, A. Ahmad-Khanlou, Solid State Ionics 138 (2000) 79.

207. H. Uchida, S. Arisaka, M. Watanabe, J. Electrochemical Soc. 149 (2002) A13.

208. A. Weber, E. Ivers-Tiffee, J. Power Sources 127 (2004) 273.

209. C. Xia, W. Rauch, F. Chen, M. Liu, Solid State Ionics 149 (2002) 11.

210. K. Imahara, C.P. Jacobson, S.J. Visco, L.C. De Jonghe, 176 (2005) 451.

211. H. Zhao, L. Huo, S. Gao, J. Power Sources 125 (2004) 149.

212. A. Hagiwara, N. Hobara, K. Takizawa, K.Sato, H. Abe, M. Naito, Solid State Ionics 177 (2006) 2967.

213. M. Asamoto, H. Yamaura, H. Yahiro, J. Power Sources 196 (2011) 1136.

214. R N Das, Materials Letter 47 (2001) 344.

215. Y Takeda, H Ueno, N Imanishi, O Yamamoto, N. Sammes, M.B. Phillipps, Solid State Ionics 86-88 (1996) 1187.

216. A.Y. Kropanev, A.N. Petrova, Inorg. Mat. 19 (1983) 1782.

217. M. Mogensen, T. Lindegaard, U.R. Hansen, G. Mogensen J. Electrochem. Soc. 141 (1994) 2122.

218. F. Tietz, I. Arul Raj, M. Zahid, D. Stover, Solid State Ionics 177 (2006) 1753.

219. T. Kenjo, M. Nashiya, Solid State Ionics 57 (1992) 295.

220. S. Li, Z. Lu, X. Huang, W. Su, Solid State Ionics 178 (2008) 1853.

221. SB Alder, Chem. Rev. 104(2004)4791.

222. T. Kawada, N Sakai, H Yokokawa, M Mori and T Iwata, J. Electrochem. Soc. 137(1990)3042.

223. T Kenjo and M Nishiya, Solid State Ionics, 57(1992)295.

224. M J L Ostergard, C Clausen, C. Bagger, and M Mogensen, Electrochim. Acta 40 (1995)1971.

225. V. Dusastre and J A Kilner, Solid State Ionics, 126 (1999) 163.

226. S. V. Moharil, B. S. Nagrare, S. P.S. Shaikh, Int. J. Hyd. Energy, 37(2012)5208.

227. Han Chen, Kui Cheng, Fei Ye, Wenjian Weng, Ceram. Int. 37(2011)1209.

228. C. Endler-Schuck, A. Leonide, A. Weber, S. Uhlenbruck, F. Tietz, E. Ivers-Tiffée, J. Power Sources 196(2011)7257.

229. L Antoni, Material Sci. Forum 461-464(2004)1073.

230. E Ivers-Tiffe, A Weber, H Schichlein (2003), Handbook of fuel cells, vol 2. Wiley, Chichester, p-587.

231. E Siebert, A Hammouche, M Kleitz, Electrochim Acta 40(1995)1741.

232. MJ Jorgensen, M Mogensen, J Electrochem. Soc. 148(2001) A433.

233. J Fleig, Annu Rev. Mat. Res. 33(2003)361.

234. M. Mogensen, B Kindl, B malmgren-Hasen, Program and abstracts of Fuel Cell seminar(1990), phenix, AZ, Courteesy Associates, Washington (DC) (1990) p.195

235. V D Belyaev, T I Politova, O A Marina, V A Sobyanin, Appl. Catal. A Gen. 133(1995) 47.

236. A O Stormer, P Holtappels, H Y Tu, U Stimming in J Huijsmans (ed) Processing of the fifth European Solid Oxide Fuel Cell Foruum, Lucerne, Switzerland, (2002)p.343.

237. P Holtappels, J Bradley, J T S Irvine, A Kaiser, M Mogensen, J. Electrochem. Soc. 148(2001) A923.

238. X. Jacques-Bédard, T.W. Napporn, R. Roberge, M. Meunier, J. Power Sources 153 (2006) 108.

239. Z. Wang, M. Cheng, Y. Dong, M. Zhang, H. Zhang ,J. Power Sources 156 (2006) 306.

240. H. Wang, W. Ji, L. Zhang, Y. Gong, B. Xie, Y. Jiang, Y. Song, Solid State Ionics 192 (2011) 413.

241. H. Moon, S. D. Kim, S. H. Hyun, H. S. Kim, Int. J. Hyd. Energy 33 (2008) 1758.

242. Jung-Hoon Song, Sun-Il Park, Jong-Ho Lee, Ho-Sung Kim, J. Mat. Processing Technology 198 (2008) 414.

243. T. Mahata, S.R. Nair, R.K. Lenka, P.K. Sinha, Int. J. Hyd. Energy 37 (2012) 3874.

244. D Simwonis, H Thülen, F.J Dias, A Naoumidis, D Stöver, J. Mat. Processing Technology, 92–93 (1999) 107.

245. M.E. Navarro, X.G. Capdevila, M. Morales, J.J. Roa, M. Segarra, J. Power Sources 200 (2012) 45.

246. J. Ding, J. Liu, W. Yuan, Y. Zhang, J. Eur. Ceram. Soc. 28 (2008) 3113.

247. Y. Liu, Y. Tang, J. Ding, J. Liu, Int. J. Hyd. Energy 37 (2012) 921.

248. J. Li, Z. Lü, X. Huang, Z. Liu, Z. Zhi, X. Sha, G. Li, W. Su, Ceram. Int. 33 (2007) 631.

249. S. B. Savignat, M. Chiron, C. Barthet, J. Eur. Ceram. Soc. 27 (2007) 673.

250. Z. Shen, X. Zhu, S. Le, W. S., K. Sun, Int. J. Hyd. Energy 37 (2012) 10337.

251. N.O. Shanti, D.M. Bierschenk, S.A. Barnett, K.T. Faber, J. Power Sources 212 (2012) 43.

252. Z. Wang, J. Qian, J. Cao, S. Wang, T. Wen, J. Alloys and Comp. 437 (2007) 264.

253. R E Meistler, E R Twiname, "Tape casting theory and practice", USA, The American Ceramic Society (2000).

Publications in Journals out of the present work

1. **Combustion synthesis, powder characteristics and shrinkage behavior of ceria gadolinia system**, **R K Lenka,**T Mahata, P K Sinha and B P Sharma, *J. Am. Ceram. Soc., 89 (2006)] 3871-3873*

2. **Combustion synthesis of gadolinia doped ceria using glycine and urea fuels, R K Lenka,** T Mahata, A K Tyagi, and P K Sinha *J. of Alloys Comp. 466(2008) 326-329.*

3. **Influence of grain size on the bulk and grain boundary ionic conduction behavior in Gadolinia doped Ceria, R.K. Lenka**, T. Mahata, A.K. Tyagi and P.K. Sinha, *Solid State Ionics, 181(2010) 262-267.*

4. **Synthesis and characterization of GdCoO$_3$ as a potential SOFC cathode material, R K Lenka,** P K Patro, T Mahata, P K Sinha and A K Tyagi, *J. of Alloys and Comp.537 (2012) 100-105.*

5. **Effect of Ba on the performance of GdCoO$_3$ cathode**
   R.K. Lenka, T. Mahata, A.K. Tyagi and P.K. Sinha, Solid State Ionics (communicated).

6. **Characterization of Ni-GDC SOFC anode fabricated using nano-powders**
   R.K. Lenka, T. Mahata, A.K. Tyagi and P.K. Sinha, *J. Am. Ceram. Soc.* (communicated).

Conference Presentations

1. **Effect of firing temperature on the ionic conductivity in 12 mol% gadolinia doped ceria** *presented at PM-08 International Conference and Exhibition held at Chennai on 20 – 21 Feb., 2008.* **R.K. Lenka**, T. Mahata, P.K. Sinha, and B.P. Sharma

2. **Synthesis and characterization of GdCoO$_3$ cathode material for SOFC application,** *presented at international symposium on material chemistry (ISMC08), during 2-6 Dec 2008, at TSH, BARC, Mumbai,* **R K Lenka**, P K patro, P K SInha and A K Tyagi

3. **Synthesis and characterization of GdCoO$_3$ as a cathode material for solid oxide fuel cell,** *presented at International Conference on Electroceramics (ICE-2009)* held at New Delhi, during Dec. 13-17, 2009, **R.K. Lenka**, P.K. Patro, T. Mahata, D. Prakash, A.K. Tyagi and P.K. Sinha.

4. **Nano-electro ceramics for IT-SOFC**, *presented at RSM-2010*, held at Parle College, during 19-20 feb 2010, **R K Lenka** and A K Tyagi

5. **Characterization of Electrode-electrolyte interface in SOFC,** *presented at national conference on "Recent Advances in Analytical Sciences and Applications"* held at Summer Hill University, Shimla, during 12-14 April 2010, **R K Lenka**, T Mahata, A K Tyagi and P K Sinha.

6. **Integration of NiO-GDC Composite with GDC electrolyte by Co-sintering and Electrochemical Characterisation for SOFC Anode Application,** *Presented at ISMC-10, TSH, BARC, Mumbai, during Dec 3-8, 2010,* **R K Lenka**, T Mahata and P K Sinha

7. **Synthesis and characterization of a novel Gd$_{0.9}$Ba$_{0.1}$CoO$_{3-\delta}$ SOFC cathode material,** *presented at ISMC-12 held at BARC, Mumbai, during Dec. 11-15, 2012*, **R.K. Lenka**, T. Mahata, P.K. Sinha and A.K. Tyagi.

8. **Fabrication of GDC electrolyte based SOFC cells by tape co-casting method,** *presented at ISMC-12 held at BARC, Mumbai, during Dec. 11-15, 2012*, **R.K. Lenka**, P. K Patro, T. Mahata, P.K. Sinha and A.K. Tyagi.